

(2)

THERMODYNAMICS AND KINETICS OF AUSTENITE DECOMPOSITION
IN THE
IRON-RICH IRON-MANGANESE SYSTEM



By

KAMALESH KUMAR SRIVASTAVA

A Thesis

Submitted to the School of Graduate Studies
in Partial Fulfilment of the Requirements

for the Degree

Doctor of Philosophy

McMaster University

November 1980

Dedicated to my parents

DOCTOR OF PHILOSOPHY (1980)
(Metallurgy)

McMASTER UNIVERSITY
Hamilton, Ontario

TITLE: Thermodynamics and Kinetics of Austenite Decomposition in the
Iron-rich Iron-Manganese System

AUTHOR: Kamalesh Kumar Srivastava, B.Sc. D.A.V. Degree College,
Kanpur (Agra University),
India
B.Tech. Indian Institute of
Technology, Kanpur, India
M.Tech. Indian Institute of
Technology, Kanpur, India

SUPERVISOR: Professor J.S. Kirkaldy

NUMBER OF PAGES: xiv, 128

ABSTRACT

A thermodynamically self consistent phase diagram together with T_0 line for iron-rich Fe-Mn system has been evaluated using the experimental tie-line information from this study and other sources and thermodynamic data from the literature.

The competing morphologies resulting from the decomposition of Fe-Mn austenite due to variation in composition and cooling rate are equiaxed, ragged ferrite and lath morphology. The former two may result via a massive mode, whereas the last one may be due to a martensitic reaction. The massive mode of decomposition has been observed in the two phase field of this system.

The solute drag theory for massive transformation due to Hillert and Sundman has been further developed for the low velocity branch. Our theory predicts a C-shaped TTT curve and an optimum in the rate of entropy production with respect to a structure parameter related to defect density.

Isothermal transformation tests have yielded a C-shaped TTT curve for Fe-3.1%Mn alloy. The transformation behaviour has been explained as controlled by trace interstitial impurities (C and N) diffusion above the nose and by the massive mode at lower temperatures.

ACKNOWLEDGEMENTS

I wish to express my sincere thanks to Professor J.S. Kirkaldy for suggesting the problems treated here and his continued guidance throughout the course of this work. It was a great pleasure to learn from him. The extensive assistance offered by Professors G.R. Purdy, J.D. Embury and J.L. Duncan who served on my supervisory committee, are gratefully acknowledged. I wish to thank the staff and graduate students of the Department of Metallurgy and Materials Science for their advice and assistance.

Gratitude is expressed to Stelco Research Centre, in particular, to Mr. D. McCutcheon for chemical analyses of the alloys used in this study. Most sincere thanks to Mrs. K. Noon for her great patience in typing this thesis.

Thanks alone cannot express the contribution by my wife, Sheela, to this research. Her understanding, patience, and sacrifices have contributed immeasurably to the completion of this work.

TABLE OF CONTENTS

| | | |
|-------------|---|----|
| CHAPTER I | INTRODUCTION | 1 |
| | Part I-Thermodynamics | |
| CHAPTER II | THE Fe-Mn PHASE DIAGRAM | 4 |
| CHAPTER III | THEORETICAL BACKGROUND | 6 |
| III.1 | Thermodynamics of the Fe-Mn Phase Diagram of the T_0 Line | 6 |
| III.1.1.A | The Ferrite-Austenite Equilibrium and the Solution Model | 6 |
| III.1.1.B | Thermodynamic Evaluation of the T_0 Line | 9 |
| III.1.2 | Thermodynamic Data | 10 |
| III.1.2.A | Activity Data | 10 |
| III.1.2.B | Data on Free Energy of Transformation of Pure Iron | 11 |
| III.1.3 | Method of Evaluation of the Phase Diagram and the T_0 Line | 12 |
| III.2 | Analysis of Isothermal Diffusion Couples | 13 |
| III.2.1 | One Phase Diffusion Couple | 13 |
| III.2.2. | Planar Binary Two Phase Infinite Diffusion Couple | 14 |
| III.2.3. | Parabolic Precipitation of α from a Super-saturated Ternary γ Alloy | 16 |
| CHAPTER IV | EXPERIMENTAL | 22 |
| IV.1 | Preparation of the Fe-Mn Alloys | 23 |
| IV.2 | Tie-line Experiments | 24 |
| IV.3 | Heat Treatment | 25 |
| IV.4 | Metallographic and Electron-Microprobe Analysis | 26 |

| | | |
|--------------|---|----|
| CHAPTER V | RESULTS OF EQUILIBRATION EXPERIMENTS | 28 |
| V.1 | Planar, One-Dimensional Austenite-Ferrite Diffusional Couple | 28 |
| V.2 | The $\gamma/\alpha+\gamma$ Diffusion Couple | 32 |
| V.3 | The Single Phase γ Diffusion Couple | 36 |
| V.4 | Equilibration of a Surface Depleted Fe-Mn Alloy | 37 |
| V.5 | Summary of the Experimental and Theoretical Phase Diagram Results | 39 |
| CHAPTER VI | DISCUSSION | 40 |
| | PART II-KINETICS | 42 |
| CHAPTER VII | INTRODUCTION | 42 |
| CHAPTER VIII | DISCUSSION OF PREVIOUS WORK | 44 |
| VIII.1 | Massive Transformations | 46 |
| VIII.2 | Martensitic Transformations | 55 |
| CHAPTER IX | EXPERIMENTAL | 57 |
| IX.1 | Continuous Cooling Tests | 57 |
| IX.2 | Isothermal Transformation Tests for Grain Boundary Ferrite Formation | 59 |
| CHAPTER X | RESULTS AND DISCUSSION | 60 |
| X.1 | Continuous Cooling Tests | 60 |
| X.2 | Isothermal Transformation Tests for Grain Boundary Ferrite Formation | 65 |
| CHAPTER XI | CONCLUSIONS | 74 |
| | REFERENCES | 76 |
| | TABLES | 80 |
| | FIGURES | 84 |

LIST OF TABLES*

1. Free Energy of Transformation of Pure Iron from Ferrite to Austenite in Cal./Mole.
2. Analyses of the Ferrovac-E Iron and Electrolytic Manganese Flakes Used for the Preparation of Fe-Mn Alloys.
3. Summary of the Experimental Results Obtained from the Equilibration of the Various Diffusion Couples.

*All the tables have been placed at the end of thesis.

LIST OF FIGURES*

1. Phase diagram for the iron-rich Fe-Mn system (after Hillert et. al.⁽²⁾). (O) Troiano et. al.⁽¹⁾, (□) Hillert et. al.⁽²⁾.
2. Free Energy of transformation of pure iron from ferrite to austenite in cal./mole.
3. a. Schematic phase diagram showing α/γ equilibrium and the location of the composition limits of the one phase diffusion couple (x),
b. Composition profiles at $t=0$ and $t>0$.
4. a. Schematic phase diagram showing α/γ equilibrium and the composition limits of the diffusion couple (X), b. Schematic composition profiles in the γ and α phases.
5. a. Schematic phase diagram showing α/γ equilibrium and the original composition of the alloy (X), b. the composition profiles in α and γ phases, following the precipitation of α .
6. a,b Schematic penetration curves in $\lambda(=x/\sqrt{t})$ space for ferrite growth in Fe-C-Mn austenites. The mass balances are represented by equal shaded areas on either side of the interface (after Purdy, Weichert and Kirkaldy⁽²⁵⁾).
7. Schematic phase diagram showing true equilibrium and para-equilibrium phase boundaries with paraequilibrium tie-lines parallel to C axis.
8. a. Schematic phase diagram showing α/γ equilibrium and the location of the composition limits of the diffusion couple, b. Schematic composition profile for the diffusion couple having a negligibly small fraction of α at $t=0$, and c. at $t>0$.

9. a. Schematic phase diagram showing α/γ equilibrium and the composition limits of the diffusion couple (x), b. composition profile at $t=0$ and c. at $t>0$.
10. Diffusion profile generated in Fe-6.2%Mn alloy on heating in vacuum sealed capsule at 1100°C for 24 hours.
11. Schematic diagram showing arrangement of Ferrovac-E, Fe and Fe-Mn alloys, as held in a molybdenum clamp (approximately full size).
12. Typical calibration curve for electron microprobe analysis.
13. a. Optical micrographs of Fe-6.2%Mn/Fe diffusion couple equilibrated at 762°C for 6 weeks (x125) and b. Fe-3.1%Mn/Fe diffusion couple equilibrated at 822°C for 6 weeks (x125). 00 and TT are the positions of γ/α interface at $t=0$ and $t=t$, respectively.
14. a. Complete composition profile in Fe-6.2%Mn couple equilibrated at 762°C for 6 weeks, taken across γ/α interface. There are a few MnO precipitates on the right.
b. Complete composition profile across γ/α interface in the Fe-3.1% Mn/Fe diffusion couple equilibrated at 822°C for 6 weeks. Note the precipitates of MnO which have been detected with Ferrovac side.
c. Expanded partial composition profile in the Fe-3.1%Mn/Fe diffusion couple equilibrated at 822°C for 6 weeks. Note the loss of resolution at the interface due to the approximately 2 μm diameter x-ray source.
15. a. Optical micrograph of Fe-2.4%Mn diffusion couple equilibrated at 762°C for 6 weeks, x125, and b. that at higher magnification of the far right region of the same sample as in (a), x250.

16. a. Composition profile in the single phase ferrite region of Fe/Fe-2.4%Mn couple equilibrated at 762°C for 6 weeks.
b. Typical composition profiles across α/γ interfaces in Fe/Fe-2.4%Mn couple equilibrated at 762°C for 6 weeks.
17. a. Optical micrograph of Fe/Fe-4%Mn, x250 and b. that of Fe-6.2%Mn/Fe-4%Mn couples equilibrated at 762°C for 6 weeks, x250.
18. Typical composition profile in Fe-6.2%Mn/Fe-4%Mn couple equilibrated at 762°C for 6 weeks.
19. a. Optical micrograph of Fe/Fe-2%Mn, x125, and b. that of Fe-2.47%Mn/Fe-3.1%Mn diffusion couple equilibrated at 822°C, x125.
20. a. Typical composition profile in Fe/Fe-2%Mn diffusion couple equilibrated at 822°C for 6 weeks. b. Typical microprobe trace across $\alpha/\gamma/\alpha$ regions of Fe/Fe-2%Mn diffusion couple equilibrated at 822°C for 6 weeks.
21. Composition profile in single phase austenite; Fe-3.1%Mn/Fe-2.47%Mn equilibrated at 822°C for 6 weeks.
22. a. Scanning electron micrographs of Fe-6.2%Mn sample austenitized at 1100°C for 120 hr and followed by annealing at 762°C for 6 weeks, x1800 and b. at higher magnification, x4500.
23. Typical composition profile of the Fe-6.2%Mn alloy austenitized at 1100°C for 120 hrs, and followed by annealing at 762°C for 6 weeks.
24. $\Delta G_{Mn}^{\alpha \rightarrow \gamma}$ as a function of temperature.
25. Phase diagram of the iron-rich Fe-Mn system.
26. Influence of cooling rate on the temperature at which the $\gamma \rightarrow \alpha$ transformation begins in Fe-Mn alloys; a-1.2; b-4.1; c-7.5;

d-9.8%Mn: I-IV stages of transformation (after Shteynberg et. al.⁽⁴⁷⁾).

27. I. Schematic phase diagrams for various types of alloys that may undergo massive transformations, (critical compositions are indicated by dashed vertical lines), II. Schematic free energy diagrams for β and α phases (after Massalski⁽⁵⁴⁾).
28. The driving force versus velocity curves for various compositions; a. pure metal, b and c correspond to the increasing concentration of impurity. The unstable part of the curve (c) is broken. The two stable branches (c.f. curve (c)) conform to the low and high velocity approximations (after Cahn⁽⁶⁴⁾).
29. Schematic steady state composition profiles in ferrite, phase boundary, and austenite for boundary velocities v_1 and v_2 .
30. a-i Various ferrite morphologies in Fe-Mn alloys as a function of composition and cooling rate, x120, number on each micrograph gives microhardness, DPH, for 500 gm load.
31. a. Optical micrograph of air cooled Fe-4%Mn alloy, x250, and b. that of prepolished sample of Fe-6.2%Mn alloy austenitized at 900°C for 10 min. and then unbroken capsule thrown in water, x125. Note the surface rumpling following the transformation, c. Scanning electron micrograph of water quenched Fe-4%Mn alloy, x1000, and d. that of Fe-1.5%Mn-0.25% Mo alloy, x500.
32. Transmission electron micrographs of a. furnace cooled Fe-2%Mn alloy, x14000, b. water quenched Fe-4%Mn alloy, x12000 and c. water quenched Fe-1.5%Mn-0.25% Mo, x64000.

33. a. Variation of ferrite morphology with composition in Fe-6.2%Mn alloy austenitized at 1100°C in vacuum sealed quartz capsule for 24 hours followed by furnace cooling. GBF: Grain boundary ferrite, RF: Ragged Ferrite, LM: Lath morphology. b. Scanning electron micrograph of the same region as shown in Figure (33a) at higher magnification.
34. Optical micrographs at higher magnification (x240) for the estimation of fraction of grain boundary ferrite formed in a. Fe-2.8%Mn alloy at 675°C for 10 min. and b. Fe-3.1%Mn at 620°C for 27 min.
35. Microstructures of Fe-3.1%Mn samples austenitized at 1040°C for 30 min. and followed by different heat treatments, x60.
36. TTT start (5%) curves for grain boundary ferrite formation in Fe-Mn alloys. (— • —) theoretical TTT start curves for pure massive control.
37. Schematic manganese spike in austenite, ahead of the advancing interface.
38. a. An approximate Fe-Mn-C isotherm: (—) true equilibrium, (— • —) envelope of zero partition, (---) para equilibrium, (O) composition of alloy, at 660°C and b. at 600°C. The areas in circle are shown on expanded scale.
39. Schematic representation of the variation of driving force for carbon diffusion ahead of austenite (controlling the rate of transformation) with variation in temperature estimated in terms of location of the bulk composition of alloy relative to the ferrite/austenite boundaries: A_1B_1/D_1E_1 , A_2B_2/D_2E_2 , and

A_3B_3/D_3E_3 are the ferrite/austenite solvus, respectively, for temperatures $T_1 > T_2 > T_3$; (— - —) envelope of zero partition.

* All the figures have been placed at the end of thesis.

CHAPTER 1

INTRODUCTION

In view of the existing energy crisis, the development of new structural steels with ever increasing demands on the strength to weight ratio, together with a high value of toughness, has become a matter of prime importance. One of the results of recent efforts is the family of HSLA (High Strength-Low Alloy) steels. Typically, these steels are alloys of iron, 1-2% Mn, 0.2-0.5% Mo, 0.05 to 0.1% C and 0.05 to 0.10% V, Nb or Ti. They derive their strength from a microstructure consisting of a fine dispersion of carbonitrides in a matrix of fine acicular ferrite. Characteristically, to promote high toughness, these steels have less than 0.1% carbon content. Furthermore, the carbonitride forming micro alloying elements V, Nb, and Ti tend to scavenge carbon from the matrix assuring an essentially Fe-Mn austenite.

It was our hypothesis at the beginning of this study that the decomposition products of this austenite can be understood in terms of an Fe-Mn base rather than a conventional Fe-C base alloy. Thus, to extend our understanding of the thermodynamics, kinetics and morphology in such steels austenite decomposition in iron-rich, Fe-Mn based alloys has been investigated.

To begin with it is useful to refer to the iron-rich side of the Fe-Mn phase diagram (Fig. 1). Iron, on heating, transforms at 911°C from the body-centred cubic (B.C.C.) structure called ferrite or α -iron to the face-centred cubic (F.C.C.) structure called austenite or γ -iron.

This transformation reverses at 1400°C, a temperature much higher than that of concern in this study.

Manganese, being an austenite stabilizing element, on alloying with iron lowers the $\gamma \leftrightarrow (\alpha + \gamma)$ transformation temperature. The ferrite solvus line shows a maximum at 3.2 at % manganese at approximately 550°C, whereas the solubility of Mn in austenite increases monotonically with decrease in temperature, reaching ~26 at.% at 400°C.

In the high temperature region above 600°C, experimental information on the $\gamma / (\alpha + \gamma)$ phase boundary is missing. This is the region where the $\gamma / (\alpha + \gamma)$ transformation for most of the commercially interesting Fe-Mn based steels (<2% Mn) takes place.

On cooling below the $\gamma / (\alpha + \gamma)$ phase boundary, the Fe-Mn austenite decomposes into equiaxed or ragged boundary ferrite, or a lath morphology, or a mixture thereof, depending upon the Mn content of the alloy and the rate of cooling. The critical cooling rates for obtaining equiaxed ferrite, ragged ferrite and lath morphology are in increasing order, respectively. Of interest here is a knowledge of the critical cooling rates for these phases as a function of Mn content and their relationship to the phase diagram.

The objectives of this study are to establish a thermodynamically consistent Fe-Mn phase diagram together with experimental confirmation in the high temperature region and to examine in general the effects of the alloy composition and the cooling rate on the mode of decomposition of iron-rich Fe-Mn austenite into massive and equiaxed ferrite. Accordingly, this thesis is divided into two parts. The first part

deals with a study of the Fe-Mn phase diagram and the second part deals with the kinetics of Fe-Mn austenite decomposition.

Part I-Thermodynamics

CHAPTER II

THE Fe-Mn PHASE DIAGRAM

Troiano and McGuire⁽¹⁾ experimentally determined the Fe-Mn phase diagram using crystal structure and lattice parameter determinations and by examination of the microstructures of equilibrated Fe-Mn alloys. They determined the $\alpha/(\alpha+\gamma)$ boundary between 400° and 800°C. However, they could not locate the $(\alpha+\gamma)/\gamma$ boundary with the same level of accuracy, as they extrapolated it from the data at 600°C and below on the basis of qualitative observations of the character of the microstructures and the diffraction patterns.

Hillert et. al.⁽²⁾ experimentally determined one point on the $\alpha/(\alpha+\gamma)$ boundary at 820°C, which is in agreement with the experimental trend of Troiano and McGuire⁽¹⁾ (Fig. 1). They used two methods for preparing the samples with α and γ in equilibrium. One was a diffusion couple method in which pieces of iron alloys of two different alloy contents were spot welded together and then heat treated at the desired temperature for a long enough time to make the concentration gradients at the α/γ boundary sufficiently flat to allow chemical analysis by an electron microprobe. In the other method, they chose the alloy composition in the two phase, $(\alpha+\gamma)$, phase field region and then heat treated the specimens at the desired temperature for long enough time to equilibrate. They determined the $\alpha/(\alpha+\gamma)$ point at 820°C but did not succeed in measuring the corresponding $(\alpha+\gamma)/\gamma$ point due to the steep manganese gradient in the austenite adjacent to the interface.

Hillert et. al.⁽²⁾ proceeded to fit theoretical $\alpha/(\alpha+\gamma)$ and $(\alpha+\gamma)/\gamma$ phase boundaries between 911° and 500°C using existing thermodynamic data and a regular solution model. The calculated $\alpha/(\alpha+\gamma)$ boundary passing through their single experimental point lies very close to that of the Troiano and McGuire⁽¹⁾ diagram, while for the $(\alpha+\gamma)/\gamma$ boundary their calculated curve lies substantially lower than the estimate of Troiano and McGuire⁽¹⁾ (911° > T > 600°C).

Gilmour et. al.⁽³⁾ reevaluated the Fe-Mn phase diagram between 911° and 700°C, using the $\alpha/(\alpha+\gamma)$ boundary of Troiano and McGuire⁽¹⁾ and the Wagner thermodynamic formalism⁽⁴⁾. Their $(\alpha+\gamma)/\gamma$ boundary lies very close to, though a little higher, than that of Hillert et. al.⁽²⁾ Kirchner et. al.⁽⁵⁾ used rigorous regular solution thermodynamics to evaluate the Fe-Mn phase diagram between 911° and 400°C. Their calculated diagram is essentially in agreement with that of Hillert et. al.⁽²⁾.

In view of the strong indication that the $(\alpha+\gamma)/\gamma$ boundary is lower than that estimated by Troiano and McGuire⁽¹⁾ and the missing experimental tie-line information in the region of high temperatures (> 600°C), an experimental evaluation of two tie-lines has been carried out. Experiments using several diffusion techniques have been performed. The theoretical methods and the experimental techniques are described in the following sections.

CHAPTER III
THEORETICAL BACKGROUND

In the first part of this section the thermodynamics of the phase equilibria, the solution model and the available thermodynamic data used to calculate the Fe-Mn phase diagram are discussed. In the second part the theoretical analysis of the equilibrated diffusion couples yielding the experimental determination of the tie-lines end compositions is presented.

III.1 Thermodynamics of the Fe-Mn Phase Diagram and of the T_0 line

III.1.1.A The Ferrite-Austenite Equilibrium and the Solution Model

The partial molar free energies, \bar{G}_i , or the chemical potentials, μ_i , for each component i are equal for two or more phases in equilibrium. Thus, for the Fe-Mn ferrite-austenite equilibrium

$$\bar{G}_{Fe}^{\alpha} = \bar{G}_{Fe}^{\gamma} \quad (1a)$$

$$\bar{G}_{Mn}^{\alpha} = \bar{G}_{Mn}^{\gamma} \quad (1b)$$

where

$$\bar{G}_{Fe} = {}^0G_{Fe} + RT \ln a_{Fe} \quad (2a)$$

$$\bar{G}_{Mn} = {}^0G_{Mn} + RT \ln a_{Mn} \quad (2b)$$

where ${}^0G_{Fe}$ and ${}^0G_{Mn}$ are the standard free energies and a_{Fe} and a_{Mn} are the activities of Fe and Mn, respectively. On combining equation (1a) with (2a)

$${}^0G_{Fe}^{\alpha} + RT \ln a_{Fe}^{\alpha} = {}^0G_{Fe}^{\gamma} + RT \ln a_{Fe}^{\gamma} \quad (3)$$

or

$$\Delta {}^0G_{Fe}^{\alpha \rightarrow \gamma} = \ln(a_{Fe}^{\alpha}/a_{Fe}^{\gamma}) \quad (4a)$$

Similarly from equations (1b) and (2b)

$$\Delta {}^0G_{Mn}^{\alpha \rightarrow \gamma} = \ln(a_{Mn}^{\alpha}/a_{Mn}^{\gamma}) \quad (4b)$$

Since the activity of a component in a given phase can be expressed as the product of an activity coefficient, γ_i , and its mole fraction, X_i , equations (4a) and (4b) can be expressed as

$$\frac{\Delta {}^0G_{Fe}^{\alpha \rightarrow \gamma}}{RT} = \ln(X_{Fe}^{\alpha}/X_{Fe}^{\gamma}) + \ln(\gamma_{Fe}^{\alpha}/\gamma_{Fe}^{\gamma}) \quad (5a)$$

$$\frac{\Delta {}^0G_{Mn}^{\alpha \rightarrow \gamma}}{RT} = \ln(X_{Mn}^{\alpha}/X_{Mn}^{\gamma}) + \ln(\gamma_{Mn}^{\alpha}/\gamma_{Mn}^{\gamma}) \quad (5b)$$

(Note that the subscripts α and γ stand for the ferrite and austenite, respectively: $X_{Fe} + X_{Mn} = 1$, and $\Delta {}^0G_i^{\alpha \rightarrow \gamma} = {}^0G_i^{\gamma} - {}^0G_i^{\alpha}$).

As this study is mainly concerned with the high temperature region involving relatively dilute solutions, Wagner's Taylor series formalism can be used to describe the concentration dependence of the activity coefficients. ⁽⁴⁾ Thus on expanding the logarithm of the activity coefficients about the state of infinite dilution and dropping the second and higher order derivatives, one obtains

$$\ln \gamma_{Mn} = \ln \gamma_{Mn}^0 + \frac{\delta \ln \gamma_{Mn}}{\delta X_{Mn}} X_{Mn} + \dots$$

$$\ln \gamma_{Mn} = \ln \gamma_{Mn}^0 + \epsilon_{Mn Mn} X_{Mn}$$

where $\epsilon_{Mn Mn}$ is the Wagner self-interaction parameter for Mn in a given phase. Furthermore, choosing infinite dilution as the standard state, γ_{Mn}^0 is taken as unity, i.e.,

$$\ln \gamma_{Mn} = \epsilon_{Mn Mn} X_{Mn} \quad (6)$$

A related expression for the solvent may be obtained by using the Gibbs-Duhem relationship, as follows:

$$X_{Fe} d \ln \gamma_{Fe} + X_{Mn} d \ln \gamma_{Mn} = 0 \quad (7)$$

$$\begin{aligned} d \ln \gamma_{Fe} &= - \frac{X_{Mn}}{X_{Fe}} d \ln \gamma_{Mn} \\ &\approx - X_{Mn} d \ln \gamma_{Mn} \quad (\because X_{Fe} \approx 1) \\ &\approx - X_{Mn} d(\epsilon_{Mn Mn} X_{Mn}) \end{aligned}$$

and

$$\ln \gamma_{Fe} \approx - \frac{\epsilon_{Mn Mn}}{2} X_{Mn}^2 \quad (8)$$

On combining equation (5a) with (8) and (5b) with (6) one obtains the following, respectively:

$$\frac{\Delta^0 G_{Fe}^{\alpha \rightarrow \gamma}}{RT} = \ln(X_{Fe}^{\alpha} / X_{Fe}^{\gamma}) + (\epsilon_{Mn Mn}^{\gamma} X_{Mn}^{\gamma 2} - \epsilon_{Mn Mn}^{\alpha} X_{Mn}^{\alpha 2}) / 2 \quad (9)$$

and

$$\frac{\Delta^0 G_{Mn}^{\alpha \rightarrow \gamma}}{RT} = \ln(X_{Mn}^{\alpha} / X_{Mn}^{\gamma}) + (\epsilon_{Mn Mn}^{\alpha} X_{Mn}^{\alpha} - \epsilon_{Mn Mn}^{\gamma} X_{Mn}^{\gamma}) \quad (10)$$

Provided the standard free energies of transformation from the ferrite to austenite phase for each component and the Wagner self-interaction parameter for Mn in each are known, the tie-lines for the two phase

region can be calculated by solving equations (9) and (10) simultaneously.

III.1.1.B Thermodynamic Evaluation of the T_0 Line

By definition, T_0 is the temperature at which $G^\alpha = G^\gamma$, i.e., the molal free energy of the ferrite phase is equal to that of the austenite, for a given composition, $X(T_0)$. The significance of T_0 may be better understood in terms of the kinetics of composition invariant decomposition of austenite, i.e., the free energy change accompanying the decomposition of austenite of composition $X(T_0)$ into ferrite of composition $X(T_0)$ is zero at temperature T_0 . Following this definition one obtains the two conditions,

$$G^\alpha(T_0) = G^\gamma(T_0) \quad (11)$$

and

$$X^\alpha(T_0) = X^\gamma(T_0) = X(T_0) \quad (12)$$

For a binary system equation (11) can be expanded as follows:

$$(1 - X(T_0))\bar{G}_{Fe}^\alpha + X(T_0)\bar{G}_{Mn}^\alpha = (1 - X(T_0))\bar{G}_{Fe}^\gamma + X(T_0)\bar{G}_{Mn}^\gamma \quad (13)$$

or

$$X(T_0) = \left[1 - \frac{(\bar{G}_{Mn}^\gamma - \bar{G}_{Mn}^\alpha)}{(\bar{G}_{Fe}^\gamma - \bar{G}_{Fe}^\alpha)} \right]^{-1}$$

On further manipulation using equations (2a), (2b), (6) and (8), one obtains

$$X(T_0) = \left[1 - \frac{\Delta^0 G_{Mn}^{\alpha+\gamma} + (\epsilon_{MnMn}^\gamma - \epsilon_{MnMn}^\alpha)X(T_0)}{\Delta^0 G_{Fe}^{\alpha+\gamma} - \frac{RT}{2} (\epsilon_{MnMn}^\gamma - \epsilon_{MnMn}^\alpha)X^2(T_0)} \right]^{-1} \quad (14)$$

Equation (14) can be solved for $X(T_0)$ using numerical iterative techniques.

III.1.2 Thermodynamic Data

III.1.2.A Activity Data

In austenite, several activity measurements have been reported in various temperature ranges, giving conflicting results in terms of the deviation from ideality⁽⁵⁻¹⁰⁾. Hillert et. al.⁽²⁾ chose a constant value for the regular solution model interaction parameter, $A^Y = -1200$ Cal/mole, to fit the austenite boundary in the low temperature range ($\leq 600^\circ\text{C}$) to the experimental points of Troiano and McGuire⁽¹⁾. Kirchner et. al.⁽⁵⁾ extracted a temperature dependent regular solution model interaction parameter, $A^Y = -5210 + 4.56T$ (Cal./mole), using Roy and Hultgren's⁽⁸⁾ activity measurements and the data extracted from the low temperature phase diagram.

Gilmour et. al.⁽³⁾ reviewed the activity data of Roy and Hultgren⁽⁸⁾ at 1450°K and obtained $\epsilon_{\text{MnMn}}^Y = -0.65$. Then, they extrapolated this value to their temperature of interest using a (theoretical) $1/T$ dependence⁽¹¹⁾ and then used a constant value $\epsilon_{\text{MnMn}}^Y = -1$ in the range $700^\circ \leq T \leq 911^\circ\text{C}$. In this study, in view of the conflicting results of the activity measurements and our doubts that equilibrium was attained in the low temperature phase diagram data, the approach of Gilmour et. al.⁽³⁾ is followed setting $\epsilon_{\text{MnMn}}^Y = -942.5/T$.

For the ferrite phase no experimental measurement of the activity is available. Kirchner et. al.⁽⁵⁾ extracted their regular solution model interaction parameter, A^α , from the phase diagram⁽¹⁾ and then back calculated to generate the phase diagram. In this study $\epsilon_{\text{MnMn}}^\alpha$ is set equal

to $\epsilon_{\text{MnMn}}^{\gamma}$. We argue firstly from the fact that the interaction parameter has been shown to be directly proportional to the coordination number and a difference of pair interaction energies⁽¹¹⁾. Furthermore, the ferrite interatomic distances are larger than in austenite. It may thus be noted that the first factor tends to make $\epsilon_{\text{MnMn}}^{\alpha}$ lower than $\epsilon_{\text{MnMn}}^{\gamma}$ whereas the second tends to make it higher. In the absence of any further information it is thus assumed that these two opposing factors cancel each other, leaving $\epsilon_{\text{MnMn}}^{\alpha} = \epsilon_{\text{MnMn}}^{\gamma}$. This hypothesis is empirically supported by the fact that $\epsilon_{\text{MnMn}}^{\gamma}$ (-0.65 at 1450°K) is not very different from $\epsilon_{\text{MnMn}}^{\text{Liquid Fe}}$ (-0.6 at steel making temperature⁽¹²⁾). In any case, as the phase boundaries in the Fe-Mn system are not very sensitive to this parameter ($580^{\circ} \leq T \leq 911^{\circ}\text{C}$), our choice of setting $\epsilon_{\text{MnMn}}^{\alpha} = \epsilon_{\text{MnMn}}^{\gamma}$ should lead to insignificant error.

III.1.2.B Data on Free Energy of Transformation of Pure Iron

The free energy of transformation of pure iron from the ferrite to austenite phase has been evaluated by several workers⁽¹³⁻¹⁹⁾, as summarised in Figure (2). Kirchner et. al.⁽⁵⁾ have used (${}^0G_{\text{Fe}}^{\gamma} - {}^0G_{\text{Fe}}^{\alpha}$) values from Orr and Chipman⁽¹³⁾, Hillert et. al.⁽²⁾ preferred to use the values given by Kohlhaas and Braum⁽¹⁹⁾ as they produced better agreement with the experimental values of X_{Mn}^{γ} at low temperatures. Gilmour, Purdy and Kirkaldy⁽³⁾ used slightly adjusted values of $\Delta {}^0G_{\text{Fe}}^{\alpha \rightarrow \gamma}$ presented by Kaufman, Clougherty and Weiss⁽¹⁵⁾. Recently, Sharma⁽²⁰⁾ has used $\Delta {}^0G_{\text{Fe}}^{\alpha \rightarrow \gamma}$ values given by Orr and Chipman⁽¹³⁾ for the calculation of the Fe-Cr-C phase diagram. In this study the data of Orr and Chipman⁽¹³⁾ retabulated by Harvig⁽²¹⁾, giving the interpolated values of $\Delta {}^0G_{\text{Fe}}^{\alpha \rightarrow \gamma}$

for intermediate temperatures, will be used in all subsequent calculations (Table I).

III.1.3 Method of Evaluation of the Phase Diagram and the T_0 Line

The most probable phase diagram and T_0 line was evaluated using the following computational procedures:

- (I) Given the thermodynamic data, viz., $\Delta^0 G_{Fe}^{\alpha \rightarrow \gamma}$, ϵ_{MnMn}^{γ} and ϵ_{MnMn}^{α} , limited experimental tie line information from the present study and from the previous sources^(1,2) and the equilibrium relationship (10), $\Delta^0 G_{Mn}^{\alpha \rightarrow \gamma}$ was calculated at different temperatures. A least squares straight line was fitted to obtain $\Delta^0 G_{Mn}^{\alpha \rightarrow \gamma}$ as a function of temperature ($580^\circ < T < 911^\circ C$). A linear temperature dependence was chosen since this has been observed in the case of other solutions of austenite stabilizing elements, e.g., C⁽²²⁾ and Ni⁽²³⁾.
- (II) Equations (9) and (10) were solved simultaneously for X^α and X^γ between 600° and $911^\circ C$ using a numerical iterative technique. $X^\alpha(T)$ and $X^\gamma(T)$ are the ferrite and austenite solvus lines of the phase diagram, respectively.
- (III) $X(T_0)$ was obtained by solving equation (14). The results are described in a later section.

III.2 Analysis of Isothermal Diffusion Couples

In this section the diffusion process will be analysed for a number of one and two phase situations. These will be treated as one dimensional problems, both sections of the diffusion couples being infinite in the x direction and of constant cross-section, the original position of the interface being at $x = 0$. The diffusion coefficients are assumed to be concentration independent.

III.2.1 One Phase Diffusion Couple

Analysis of this situation provides a good approximation to the composition profile in a $\gamma/(\alpha+\gamma)$ couple, where the second phase, α , is a negligibly small fraction. This is the simplest situation to analyse. If D^γ is the composition independent diffusion coefficient in the γ phase, the diffusion profile can be described by Fick's second equation, together with initial and boundary conditions as following:

$$\frac{\partial C}{\partial t} = D^\gamma \frac{\partial^2 C}{\partial x^2} \quad (15)$$

$$C = C^{II} \text{ for } x < 0 \text{ at } t = 0 \quad (16a)$$

$$C = C^I \text{ for } x > 0 \text{ at } t = 0 \quad (16b)$$

$$C = C^{II} \text{ for } x = -\infty \text{ at } t \geq 0 \quad (16c)$$

$$C = C^I \text{ for } x = +\infty \text{ at } t \geq 0 \quad (16d)$$

where C is the composition at any instant, t , at position x . The composition limits of the diffusion couple relative to the phase diagram and the composition profiles at $t = 0$ and $t > 0$ are shown in

the Figures (3a) and (3b). The appropriate solution is

$$C = C^I + \frac{C^{II} - C^I}{2} \left[1 - \operatorname{erf} \frac{x}{2\sqrt{D^\gamma t}} \right] \quad (17)$$

III.2.2 Planar Binary Two Phase Infinite Diffusion Couple

An analytic treatment has been given by Wagner⁽²⁴⁾. The composition profiles of the two components relative to the phase diagram and their initial composition profiles are shown in Figures (4a) and (4b), respectively. It is assumed that local equilibrium is achieved as soon as the two components of the couple are brought together.

Following Wagner⁽²⁴⁾, the differential equations, initial conditions, and the boundary conditions describing the diffusion in the two phases are written as follows:

For the γ phase

$$\frac{\partial C}{\partial t} = D^\gamma \frac{\partial^2 C}{\partial x^2} \text{ for } x < 0 \quad (18)$$

$$C = C^{II} \text{ for } x < 0, t = 0 \quad (19)$$

Similarly for the α phase,

$$\frac{\partial C}{\partial t} = D^\alpha \frac{\partial^2 C}{\partial x^2} \text{ for } x > 0 \quad (20)$$

$$C = C^I \text{ for } x > 0, t = 0 \quad (21)$$

In terms of the assumed parabolic kinetics for the position of the moving interface given by

$$\xi = \eta \cdot 2 \sqrt{D \cdot t} \quad (22)$$

where η is a constant, the particular solution of equation (18) which satisfies the initial and boundary conditions, for the γ phase is

$$C = C^{II} - \frac{C^{II} - C^{\gamma/\alpha}}{1 + \operatorname{erf}(\eta^{\gamma})} \left\{ 1 + \operatorname{erf} \frac{x}{2\sqrt{D^{\gamma}t}} \right\} \text{ for } -x < \xi \quad (23)$$

Similarly for the α phase

$$C = C^I + \frac{C^{\alpha\gamma} - C^I}{(1 - \operatorname{erf}(\eta^{\alpha}))} \left\{ 1 - \operatorname{erf} \frac{x}{2\sqrt{D^{\alpha}t}} \right\} \text{ for } -x > \xi \quad (24)$$

where $\eta^{\alpha} = \eta^{\gamma} \sqrt{\phi}$ and $\phi = D^{\gamma}/D^{\alpha}$. The velocity of the interface, v , can be expressed in terms of the parameters for either phase, viz.,

$$v = \frac{d\xi}{dt} = \eta^{\gamma} \sqrt{D^{\gamma}/t} \quad (25)$$

The amount of material necessary for a small displacement of the interface, $d\xi$, can be equated to the material delivered by the γ phase minus the material drained into the α phase in an infinitesimal interval of time, dt , i.e.

$$(C^{\gamma\alpha} - C^{\alpha\gamma}) \frac{d\xi}{dt} = -D^{\gamma} \frac{\partial C}{\partial x} \Big|_{x=\xi^-} + D^{\alpha} \frac{\partial C}{\partial x} \Big|_{x=\xi^+} \quad (26)$$

Now from equation (22), (23) and (24)

$$C^{\gamma\alpha} - C^{\alpha\gamma} = \frac{1}{\eta^{\alpha} \sqrt{\pi/\phi}} \frac{C^{II} - C^{\gamma\alpha}}{(1 + \operatorname{erf}(\eta^{\alpha}/\sqrt{\phi}))} \exp -\left(\frac{\eta^{\alpha}}{\phi}\right)^2 + \frac{1}{\eta^{\alpha} \sqrt{\pi}} \frac{C^{\alpha\gamma} - C^I}{(1 - \operatorname{erf}(\eta^{\alpha}))} \exp -(\eta^{\alpha})^2 \quad (27)$$

It should be noted that a special case of equation (27) can be applied to the parabolic precipitation of α from a supersaturated γ phase of concentration C^{II} as indicated in Fig. (5). In this case the precipitate can be assumed to evolve at constant composition so that the second term on the right hand side vanishes and (27) becomes

$$\eta^\gamma = \frac{1}{\sqrt{\pi}} \frac{C^{II} - C^{\gamma\alpha}}{C^{\gamma\alpha} - C^{\alpha\gamma}} \frac{\exp - (\eta^\gamma)^2}{(1 + \operatorname{erf} \eta^\gamma)} \quad (28)$$

This is the binary limit of a ternary formula which we will be presenting in the following section.

III.2.3 Parabolic Precipitation of α from a Supersaturated Ternary γ Alloy

We are concerned here with precipitation in the Fe-Mn-C (or N) system which has a constitution as indicated in Figs. (6a-6b) and we seek the generalizations of equation (28). The local equilibrium treatment of this problem was due originally to Purdy et. al.⁽²⁵⁾ and has been used by Gilmour et. al.⁽³⁾ in their study of the role of manganese in the formation of proeutectoid ferrite. An approximate and numerically equivalent method has been given by Hillert⁽²⁶⁾. In this problem we need to obtain both Mn and C profiles which satisfy the two interfacial mass balances

$$(C'_{i1} - C_{i1})v = -J_i(\xi), \quad i = 1, 2 \quad (29)$$

($i = 1$ and 2 represent carbon and manganese, respectively) where C_{i1} is concentration of component i and $J_i(\xi)$ is the flux of the component

i , at the interface. Primed quantities refer to ferrite and unprimed to austenite. The velocity of the precipitate growth and the flux of component i are given as follows:

$$v = \frac{\eta'}{2\sqrt{t}} \quad (30)$$

and

$$J_i = -\sum_{k=1}^2 D_{ik} \frac{\partial C_k}{\partial x} \quad (31)$$

where D_{ik} describes the diffusion of component i on the concentration gradient of component k . The growth rate constant η' must be determined by simultaneous solution of the two flux balances

$$(C'_{i1} - C_{i1}) \frac{\eta'}{2\sqrt{t}} = \sum_{k=1}^2 D_{ik} \frac{\partial C_k}{\partial x} \quad (i = 1, 2) \quad (32)$$

These equations involve only two independent variables, i.e., η' and one of the concentration terms, say, C_{11} as the other three concentration terms (C'_{11} , C_{21} , C'_{21}) are fixed by the particular equilibrium tie line in the two phase region corresponding to the interfacial concentrations. The solutions of equation (32) predict two types of transformations, as discussed qualitatively in the following paragraphs.

As shown in Figure (6a), a sample with composition A rapidly cooled to the isotherm temperature would be highly super-saturated. For this alloy a "zero partition" tie line is represented by B'-B. As $D_{11} \gg D_{22}$ and carbon diffuses much faster than manganese ahead of the interface stable "no-partition" profiles such as shown in Fig. (6a) exist as solutions of the diffusion equations. The very small depletion of Mn in ferrite (not experimentally detectable) would be balanced by the narrow Mn "spike" at the interface. The steep Mn

gradient will satisfy the equations for the rapid transformation rate, although the transformation is carbon diffusion controlled. Ignoring the ternary interactions, this argument holds for any alloy within the dashed triangle in Fig. (6a). The ternary interaction leads to further reductions in the driving force due to the negative interaction between Mn and C.

In this region of high supersaturation $C'_{11} \approx 0$ and $C_{20} \approx C'_{21}$ (C_{i0} represents the bulk composition of the component i). Furthermore, $D_{11} \gg D_{22}$ and D_{21} the diffusion of Mn on a carbon gradient is negligible because due to high mobility, carbon can relax to the manganese gradient long before manganese can readjust to carbon gradient⁽²⁷⁾. With these simplifications, an approximate growth parameter β_1 (related to n' by $\beta_1 \approx n' \sqrt{D_{11}}/2$) is given as follows:

$$\beta_1 = \frac{\Delta_1}{\sqrt{\pi} C_{11}} \left(1 + \frac{D_{12}}{D_{11}} \frac{\Delta_2}{\Delta_1} \right) \frac{e^{-\beta_1^2}}{\operatorname{erfc} \beta_1} \quad (33)$$

where Δ_1 and Δ_2 are the concentration differences, as shown in Fig. (6a). The ratio D_{12}/D_{11} is to be related to the thermodynamic parameter through the quasi-steady carbon diffusion approximation⁽²⁸⁾. Since $D_{12}/D_{11} \approx \epsilon_{12} X_1$, equation (33) contains only carbon diffusion coefficients, it is only necessary to know that the manganese coefficients are small. The effective carbon concentration for the transformation is given as

$$\bar{C}_{11} = C_{11} + \frac{D_{12}}{D_{11}} (C_{21} - C_{20}) \quad (34)$$

It should thus be noted that the driving force for the carbon diffusion controlled transformation is reduced by a constitutional effect and a

ternary thermodynamic effect of Mn.

For a low supersaturation alloy of composition D lying outside the dashed "triangle" in Fig. (6b), all solutions of the mass balance require some manganese partition resulting in a very low growth rate. The approximate tie-line for this alloy is E'-E where the carbon depletion in ferrite is balanced by a very small increase in the austenite spread over a large distance, with a small local increase at the interface due to the ternary thermodynamic interaction. In this case of low supersaturation $C_{11} \approx C_{10}$ and $C'_{11} = 0$ and the equivalent growth parameter β_2 (related to n' by $\beta_2 = n'\sqrt{D_{22}}/2$) is given as follows:

$$\beta_2 = \frac{1}{\sqrt{\pi}} \frac{\Delta_2}{(C_{21} - C'_{21})} \frac{e^{-\beta_2^2}}{\operatorname{erfc} \beta_2} \quad (35)$$

This represents a manganese-controlled reaction.

There is a second approach to this problem based on the concept of paraequilibrium due originally to Hultgren⁽²⁹⁾ and clarified by Hillert⁽³⁰⁾ and by Gilmour et. al.⁽³⁾. This concept of a metastable interface insists that the fast diffusing carbon have equal activities at and through the interface and that the alloy concentration, e.g.,

X_{Mn} satisfy

$$\frac{X_{\text{Mn}}^{\alpha}}{X_{\text{Fe}}^{\alpha}} = \text{constant} \quad (36)$$

on going through the interface. This leads to a pseudo phase diagram as in Fig. (7) in which the tie-lines are essentially parallel to the X_{C} axis. Note that because of $X_{\text{Mn}}^{\alpha} = X_{\text{Mn}}^{\gamma}$ the zero carbon terminus of the diagram must coincide with the T_0 line. The transformation of alloy X

shown in Fig. (7) can then be discussed by a binary formula of type (28) with an adjustment of the interface carbon values according to the identified paraequilibrium tie line. It is not yet clear that such a ternary reaction exists in nature.

III.2.3 PLANAR ONE PHASE/TWO PHASE BINARY DIFFUSION COUPLE

Due to the complex nature of this three-dimensional diffusion situation, it will be discussed only in terms of the limiting conditions. The first condition concerns an $\gamma/(\alpha+\gamma)$ couple when α in the right hand section is a negligibly small fraction. This situation is similar to that in the one phase diffusion couple discussed in III.2.1., except that the overall kinetics of the moving front will be somewhat faster than normal parabolic as part of the material is delivered to α particles so as to transform them to γ , Figs. (8a-8c). The composition profile may be approximated as follows:

$$C = C^{\gamma/\alpha} + \frac{C^{II} - C^{\gamma\alpha}}{2} \left(1 - \operatorname{erf} \frac{x}{2\sqrt{D^{\gamma}t}} \right) \quad (37)$$

The second limiting condition concerns the transformation of a $\gamma/(\alpha+\gamma)$ couple where the γ in the right hand section is a negligibly small fraction. This may be represented by a diffusion situation which is similar to that discussed III.2.2. There will, however, be a perturbation in the diffusion profile in the α phase near each γ particle as shown in Figs. (9a-9c). In this case with the bulk diffusion proceeding only in the γ phase, the diffusion equation, initial and boundary conditions can be written as follows⁽²⁴⁾:

$$\frac{\partial C}{\partial t} = D^{\gamma} \frac{\partial^2 C}{\partial x^2} \text{ for } x < \xi \quad (38)$$

where ξ is the position of interface at any instant $t > 0$.

$$C = C^{II} \text{ for } x < 0, \text{ at } t = 0 \quad (39)$$

$$C = C^{\gamma\alpha} \text{ for } x = \xi^- \text{ at } t > 0 \quad (40)$$

Assuming as usual parabolic kinetics for the moving interface, i.e.,

$$\xi = \eta \sqrt{2D^{\gamma}t} \quad (41)$$

where η is a constant, the particular solution of equation (38) satisfying the initial and boundary conditions is

$$C = C^{II} - \frac{C^{II} - C^{\gamma\alpha}}{1 + \operatorname{erf}(\eta)} \left(1 + \operatorname{erf} \frac{x}{2\sqrt{D^{\gamma}t}}\right) \quad (42)$$

Now applying the mass balance, the material delivered by the austenite on the left of the moving interface is equated to that necessary for raising the concentration level on the right from the average C^I to $C^{\gamma\alpha}$, i.e.,

$$(C^{\gamma\alpha} - C^I) \frac{d\xi}{dt} = -D^{\gamma} \frac{\partial C}{\partial x} \quad (43)$$

From equations (41), (42), and (43) we thus obtain

$$\eta = \frac{1}{\sqrt{\pi}} \frac{C^{\gamma\alpha} - C^I}{C^{II} - C^{\gamma\alpha}} \frac{\exp(-\eta^2)}{(1 + \operatorname{erf} \eta)} \quad (44)$$

Note the similarity between this approximate growth rate equation and equation (28).

CHAPTER IV

EXPERIMENTAL

The experimental determination of the tie lines in the Fe-Mn system reveals the inherent problem of slow diffusion of the substitutional alloying element, particularly in the austenite phase. The annealing periods required to reach complete thermodynamic equilibrium for previously homogenised alloy samples are very long. It may be recalled that Hillert et. al.⁽²⁾ could not evaluate X^{γ} in their experiment due to this limitation. Gilmour, Purdy and Kirkaldy⁽³⁾ made use of two experimental facts to overcome this difficulty in the equilibration of Fe-Mn-C alloys: firstly that the diffusion of substitutional elements in upquenched austenite is greatly enhanced⁽³⁾ due to the presence of an extensive defect structure and secondly that the diffusion coefficient for chromium (another substitutional alloying element) in ferrite is known to be approximately two orders of magnitude higher than that in austenite⁽³²⁾. They successfully equilibrated a structure consisting of austenite dispersed in ferrite matrix, relying on rapid diffusion of manganese through the ferrite for equilibration abetted by enhanced manganese diffusion in the austenite by the reverse martensitic transformation. Sharma⁽²⁰⁾ has followed the same lines for equilibration of Fe-Cr-C alloys.

In this study two distinct methods have been used to equilibrate ferrite with austenite, yielding tie line compositions.

IV.1 Preparation of the Fe-Mn Alloys

Iron-rich binary alloys containing up to 6.2 weight percent manganese were prepared using Ferrovac-E iron and electrolytic manganese of spectrographic grade (99.99%). The composition of these starting materials is given in Table II. The Ferrovac-E iron was treated with moist H₂ for one week at 890°C to further reduce carbon level. These approximately 40 gram samples were prepared in a non-consumable tungsten electrode arc furnace under an argon atmosphere. Larger batches of nearly 400 grams were prepared using untreated Ferrovac-E iron and electrolytic manganese by melting in an alumina crucible in an induction furnace under a purified helium atmosphere. All of these alloys were deformed by rolling at least 30%, homogenised at 1300°C for one week, and finally machined to remove 2 to 3 mm of skin to avoid the effects of macro-segregation and preferential evaporation of manganese from the surface. The homogeneity of these alloys was confirmed by chemical analysis using atomic absorption spectrography and the electron microprobe.

Samples of continuously varying manganese concentration were prepared by austenitizing the desired Fe-Mn alloys at 1100°C for various lengths of time in a vacuum-sealed quartz capsule taking advantage of the preferential evaporation of manganese from the surface. Typical composition profiles developed in these samples is shown in Figure (10).

IV.2 Tie-line Experiments

Two methods were adopted for the preparation of specimens in which ferrite and austenite phases could equilibrate with each other. The first was a diffusion couple method in which alloys of different manganese concentrations were joined together or with a piece of Ferrovac-E and heat treated for a long enough time so as to yield experimentally accessible interface of precipitated ferrite-austenite equilibria. In the second method, the samples of continuously varying manganese concentration were heat treated for long periods at a given temperature to yield distinct regions of ferrite and austenite. (Note that the austenite on subsequent quenching decomposes into various supercooled forms). Chemical microanalysis then allows the determination of the end compositions of the tie lines.

The samples of chosen alloys of approximately 4 mm x 10 mm x 10 mm were encapsulated in quartz under a vacuum of 5×10^{-5} torr, austenitized at 980°C for 30 minutes and then quenched in water to obtain a starting super-cooled structure. The samples to form the diffusion couple were then polished to one micron level and tight fitted into a clamp made of pure (99.9%) molybdenum as shown in Fig. (11). The criterion for the choice of the material of the clamp was that it should have a thermal expansion coefficient lower than that of iron (The linear thermal expansion coefficient of Mo and Fe at room temperature are $3.0 \times 10^{-6}/^{\circ}\text{F}$ and $6.7 \times 10^{-6}/^{\circ}\text{F}$, respectively⁽³³⁾), so that during the annealing period the diffusion couple expands more than the clamp assuring good welding contact between the couple sections and uniform diffusion across the interface.

IV.3 Heat Treatment

In this study, two temperatures in the high temperature range were chosen for austenite-ferrite equilibrium, viz., 762° and 822°C. For equilibration at 762°C, an Fe-6.2% Mn alloy was chosen for equilibration of the surface depleted sample and a stack consisting of Fe/Fe-2.47%Mn/Fe/Fe-4%Mn/Fe-6.2%Mn/Fe was chosen for local equilibration within diffusion couples. All compositions are in weight percent unless otherwise stated. Since each element in this cascade is 3 to 4 mm thick, the Mn diffusion field of one couple (a maximum of 200 μm long) does not overlap with that of the neighbouring couple. Similarly, for equilibration at 822°C, a stack consisting of Fe/Fe-2.0%Mn/Fe/Fe-2.47%Mn/Fe-3.1%Mn/Fe was chosen.

These samples, with starting structures for the Fe-Mn alloys in the lath form were encapsulated in a quartz tube at a vacuum of 5×10^{-5} Torr. In turn, the capsule was suspended in a kanthal wound vertical furnace having a uniform temperature zone of approximately 40 mm length. During the equilibration period, a constant flow of a purified mixture of helium plus ten percent hydrogen was maintained through the furnace tube to ensure good welding.

The temperature was measured using a Pt/Pt-13% Rh thermocouple located adjacent to the sample outside the capsule and a self compensating (for ice junction) digital temperature indicator. The proportional controller used for the input power control to the furnace allowed a maximum fluctuation of $\pm 1^\circ\text{C}$. The thermocouple was calibrated at 419.5° and 960.5°C using melting/freezing point of high purity (99.99%) zinc and silver, respectively.

IV.4 Metallographic and Electron-Microprobe Analysis

The equilibrated diffusion couples were cut perpendicular to the interface between the couple, using a low speed diamond wheel cutter. This slice of approximately 3 mm thickness was mounted on a bakelite backing and polished to the 1 μ m level for metallographic and electron-microprobe examination. 2% nital and 2% picral solutions were used as etchants to delineate the microconstituents, the former being used for ferrite boundaries and the latter for lath structure details. A number of photomicrographs were taken of various areas of the specimens and the volume fractions of the phases were determined using the linear intercept method⁽³⁴⁾.

The equilibrated, polished and etched samples were analysed for Mn concentration using the Cameca electron-microprobe detecting the K_{α} line, at an accelerating voltage of 20 kV and a specimen current of 100 nanoamperes. It may be noted that the light etching of the sample has been shown to have no effect on the microprobe analyses⁽³⁵⁾. A typical calibration curve using Fe-Mn alloys of concentrations 1.2%, 2.0%, 4.0% and 6.2% Mn as standards is shown in Fig. (12). The background counts were measured on a piece of Ferrovac-E iron. The bars in this figure represent the 95% confidence limit of the counts for a given alloy composition. It may be recalled that the 95% confidence limit is given by $\pm 2\sigma$, where σ is the standard deviation. Since the emission of x-rays follows Poisson statistics quite accurately (due to the random nature of the emission of electrons from the gun), and the dead times losses of the counters were negligible, the standard deviation may be evaluated as the square root of the total number of

counts⁽³⁶⁾. Hence, for these low concentration measurements, the statistical R.M.S. error is given by⁽³⁷⁾

$$\sigma(\%) = \frac{100\sqrt{N_p + N_B}}{N_p - N_B} \quad (45)$$

where N_p is the total number of counts of the characteristic radiation and N_B is the number of background counts.

For the present measurements, at the 2% Mn level, σ is 1.6% which would correspond to a standard deviation of about 0.03 at.% in the tie line end composition determinations. At the 95% confidence level, the expected error in a single tie line and composition measurement is ± 0.06 at.%. It may be noted that this does not recognize other possible systematic errors.

Various composition profiles were measured via point counts with an automatic step scan procedure, i.e., the sample is moved intermittently by a motor controlled by an electronic timer such that the timer, and hence the motor, starts at the same time as the scalar print out. The motor then runs for a preset time which must be less than the print-out cycle as the x-rays are not being counted during this period. Step sizes ranging from 5 μm near the tail of the error function shaped composition profile to 0.5 μm near the interphase-interface were used.

CHAPTER V

RESULTS OF EQUILIBRATION EXPERIMENTS

In this section the optical and electron micrographs of the equilibrated diffusion couples together with their microprobe traces are presented and analysed in relation to the theory discussed in section III.2 to yield the end compositions of the tie lines for the Fe-Mn system. These results together with other data will be used to construct the phase diagram ($600^{\circ} \leq T \leq 911^{\circ}\text{C}$).

V.I Planar, One-Dimensional Austenite-Ferrite Diffusional Couple

Figures (13a) and (13b) are optical micrographs of Fe-6.2%Mn/Fe equilibrated at 762°C and Fe-3.1%Mn/Fe equilibrated at 822°C , respectively. These microstructures consist of ferrite (on the right) α and the decomposed form of austenite (on the left) α' . One may note broken straight lines behind the advancing (to the left) wavy γ/α interfaces as remnants of imperfections in the welding of the diffusion couple. These lines may be used as indicators of the original position (at $t=0$) of the γ/α interfaces⁽³⁸⁾. The occasional crossing of the original γ/α interface position by the α grain boundaries and the continuity of the etching shade (besides the continuity of the composition profile, which will be discussed later) are microstructural evidence of good weld across the γ/α interface.

The metastable decomposed form of austenite, α' , could be either equiaxed or ragged ferrite, or a lath morphology, or a mixture thereof, depending upon the composition and hence the hardenability of the

equilibrated austenite. For example, the austenite in figure (13a), well away from the α/γ interface, having bulk composition of 6.2% Mn decomposes mainly into a lath morphology, whereas that shown in figure (13b) well away from γ/α with bulk composition 3.1% Mn decomposes primarily into ragged ferrite. This aspect will be discussed in detail in the second part of this thesis.

Figure (14a) shows the composition profile across the γ/α interface in the Fe-6.2%Mn/Fe diffusion couple equilibrated at 762°C. This profile is drawn by eye as a smooth curve through the data points determined by the electron microprobe analysis. Note that its general form is as predicted by equations (23) and (24). As discussed in section III.2.2., the discontinuity values in the composition profile in austenite at Y' and that in ferrite at Y represent the composition of austenite and that of ferrite, respectively, in equilibrium with each other. I.e., the tie line end compositions as marked by arrows are $X_{762^\circ\text{C}}^\alpha = 1.95\% \text{Mn} = 1.98 \text{ at. \%Mn}$ and $X_{762^\circ\text{C}}^\gamma = 4.55 \text{ w\%Mn} = 4.62 \text{ at. \%Mn}$. It is to be noted that these discontinuity points must be determined as intersection of the extrapolated diffusional compositional profiles in each phase to the γ/α interface.

The Matano interface in Figure (14a) has been determined, graphically. It amounts to the placing of line BE at such a position that the area ABCYY'A (corresponding to the amount of Mn delivered by austenite) is equal to the area ECDE (corresponding to the amount of Mn received by ferrite). The perpendicular distance between BE and YY', ξ , is the distance through which the γ/α interface has moved during the equilibration period. In this analysis, the areas were measured

using a planimeter and ξ was found to be 6.5 μm . The value on the microstructure shown in figure (13a) varies from 8 to 12 μm . The discrepancy is probably due to a Kirkendall effect⁽³⁸⁾ in α and/or γ .

Figure (14b) is the complete composition profile across the γ/α interface in the Fe-3.1 %Mn/Fe diffusion couple equilibrated at 822°C. Again using the same criterion, the end compositions of the tie line, marked by arrows, are determined as $X_{822^\circ\text{C}}^\alpha = 1.32 \text{ w\%Mn} = 1.35 \text{ at.\%Mn}$ and $X^\gamma = 2.40 \text{ w\%Mn} = 2.44 \text{ at.\%Mn}$. The displacement of the γ/α interface during equilibration determined on the basis of the mass balance gives $\xi = 25 \mu\text{m}$ whereas that on the microstructure shown in Figure (13b) varies from 50 to 60 μm .

Figure (14c) shows an expanded partial composition profile in the neighbourhood of the γ/α interface in the equilibrated Fe-3.1% Mn/Fe diffusion couple in a different region. The profile in austenite is relatively flatter near the interface, probably due to an incomplete weld. Due to the high Mn vapour pressure the interface is nonetheless equilibrated as a comparison of the intercepts indicate.

It may be recalled that at $t = 0$ the Fe-6.2%Mn and Fe-3.1%Mn alloys are in the "as-quenched", or "martensitic" form. As the equilibration treatment begins the martensite is up-quenched transforming to austenite, the latter inheriting the extensive defect structure of the former. Krauss⁽³⁹⁾ has observed high densities of tangled dislocations in up-quenched Fe-Ni martensite which substantiates this proposition. Thus the diffusivity of Mn in up-quenched martensite may be much higher than that in the equilibrated austenite. This high diffusivity of Mn

in the up-quenched state may be a very slowly decreasing function of time as Kurdumov⁽³¹⁾ has indicated defects do not anneal out easily at temperatures below 1000°C. It has been noticed also (Fig. 14b) that the ferrite side of all the couples has substantial precipitation of MnO₂ due to the expected high oxygen content of the ferrovac-E.

In view of the complex nature of the effective diffusion coefficient of Mn in the austenite phase, the multiple sink situation on the ferrite side, and our main objective being the determination of the end compositions of the tie lines in the Fe-Mn system, it was decided not to perform a quantitative diffusional analysis of these composition profiles. Nonetheless, it is worth noting semiquantitatively from Figure (14a) that $D^\alpha/D^\gamma \sim 15$, a lower than normal value (~ 100) since D^γ has been artificially enhanced by up-quenching.

V.2 The $\gamma/\alpha\gamma$ Diffusion Couple

Figure (15a) is a micrograph of a Fe/Fe-2.47% Mn diffusion couple equilibrated at 762°C. This micrograph consists of the three distinct regions: equiaxed ferrite on the far left, a fine distribution of ferrite and decomposed austenite in the middle, and a representative equilibrium distribution of ferrite and austenite (in decomposed form) corresponding to the bulk composition, Fe-2.47% Mn, on the far right. The first and the third regions on the two ends will be discussed in detail, whereas the fine structure in the middle (probably due to the higher nucleation rate in this region) will not be discussed any further. Figure (15b) is the microstructure corresponding to the far right in figure (15a) at higher magnification (x250), several photomicrographs were taken at high magnification in this region and the austenite fraction was determined by the linear intercept method to be equal to $18.94 \pm 0.72\%$.

Figure (16a) is the composition profile of the Fe/Fe-2.47%Mn diffusion couple equilibrated at 762°C, in the equilibrated ferrite (far left in figure (15a) region). Since this diffusion couple represents equilibration between a single phase alloy and a two phase alloy and since only a small fraction of the second phase on the other (right end in figure (15a)) end, it can be approximated as a case of diffusion between the two components in the same phase but differing in composition, as discussed in section III.2.3. The validity of this approximation is confirmed by the complete error function shape of the composition profile in the ferrite phase. The asymptotic composition on the far right end of the diffusional composition profile represents the composition

of ferrite (in equilibrium with austenite), $X_{762^\circ\text{C}}^\alpha = 1.95 \text{ w\%Mn} = 1.98 \text{ at.\%Mn}$, confirming the result of the previous section.

As an aside, we note that Kirkaldy, Smith and Sharma have⁽⁴⁰⁾ demonstrated a negligible composition dependence of D_{Mn} up to Fe-4% Mn in δ -ferrite in the temperature range of 1446°C to 1494°C. Assuming the same simple nature of diffusion in the lower temperature range, (since the structure remains the same), the composition independent diffusion coefficient, D , may be evaluated as

$$D = \frac{Z^2}{\pi t} \quad (46)$$

where Z is the intercept at the abscissa by the tangent to the composition profile at the original position of the interface. This, in turn, may be determined on the basis of the mass balance and graphically by equating the areas AYBA and CY'BC. This construction in figure (16a) yields $Z^\alpha = 55 \text{ }\mu\text{m}$ or $D_{762^\circ\text{C}}^{\text{Mn},\alpha\text{Fe}} = 2.7 \times 10^{-12} \text{ cm}^2/\text{sec}$. This value of diffusion coefficient is in excellent agreement with the value ($3.5 \times 10^{-12} \text{ cm}^2/\text{sec}$) obtained by interpolation of the high temperature data of Kirkaldy et. al.⁽⁴⁰⁾ and low temperature data of Nohara et. al.⁽⁴¹⁾.

Figure (16b) shows the composition profile obtained by scanning across several $\alpha/\gamma/\alpha$ regions in the far right region of the micrograph shown in the figure (15a). The composition of ferrite is uniformly constant, i.e., $X_{762^\circ\text{C}}^\alpha = 1.95 \text{ w\%Mn} = 1.98 \text{ at.\%Mn}$, confirming the results of previous sections. The uniformity of the composition in the ferrite phase may be attributed to the relatively large ferrite grain size which eliminates the smearing effect from underneath and to the relatively larger diffusion coefficient of Mn in ferrite than that in

austenite. Due to the absence of these features the composition profile in austenite shows either strong gradients or uniformly lower composition than $X_{762^\circ\text{C}}^Y$ as determined in section V.1. This uniform dilution effect may be caused by ferrite lying under the austenite grain being analysed. Due to these limitations we place little weight on $X_{762^\circ\text{C}}^Y$ deduced from these composition profiles, Figure (16b).

Figures (17a) and (17b) are typical micrographs of Fe/Fe-4.0% Mn and Fe-6.2%Mn/Fe-4%Mn diffusion couples, respectively, equilibrated at 762°C. The former consists of equilibrated ferrite on the left of the vertical wavy $\alpha/(\alpha+\gamma)$ interface and a mixture of ferrite and the metastable decomposed form of austenite on the right, whereas the latter consists of primarily a lath morphology on the left and a mixture of ferrite and a metastable decomposed form of austenite on the right.

Figure (18) is a composition profile as scanned across the equilibrated Fe-6.2%Mn/Fe-4.0%Mn diffusion couple-interface. The Mn delivered from the left section of the diffusion couple transforms ferrite to austenite and raises the concentration of Mn in austenite on the right. Thus the composition profile on the left falls continuously, in the form of an error function, to a nearly constant value. It is seen that near a ferrite particle the composition rises corresponding to the austenite in equilibrium. However, due to the dilution caused by the ferrite particles the microprobe detects less than the composition of austenite in equilibrium with ferrite. Furthermore on meeting a large ferrite particle the composition profile falls close to $X_{762^\circ\text{C}}^\alpha$.

Figures (19a) and (19b) are micrographs of the Fe/Fe-2%Mn and Fe-2.47%Mn/Fe3.1 %Mn diffusion couples, respectively, equilibrated at 822°C for 6 weeks. The former is of the $\alpha/(\alpha+\gamma)$ kind and the latter of the γ/γ kind. Due to the lack of contrast between α and γ (in decomposed form) in figure (19a) it was not possible to evaluate the phase fraction of austenite in equilibrium with ferrite, from this sample.

Figure (20a) shows a composition profile across the Fe/Fe-2%Mn diffusion couple equilibrated at 822°C. $X_{822^\circ\text{C}}^\alpha$ and $X_{822^\circ\text{C}}^\gamma$, as marked by the arrows, clearly confirm the results of the previous sections. It may be noted that the composition of the austenite is constant within the statistical (95% confidence level) limits, confirming the attainment of complete equilibrium in relatively large austenite regions (so free from the smearing effect). Figure (20b) is the microprobe trace of several $\alpha/\gamma/\alpha$ regions of this sample, which again confirms the $X_{822^\circ\text{C}}^\alpha$, $X_{822^\circ\text{C}}^\gamma$ and the attainment of equilibrium.

V.3 The Single Phase γ Diffusion Couple

Figure (21) shows a composition profile across the Fe-3.12%Mn/Fe-2.47%Mn diffusion couple equilibrated at 822°C. Analysis of this diffusion profile does not provide any direct information about the end compositions of the tie line. However, this smooth error function shaped composition profile yields two useful pieces of information. Firstly, it certifies that at 822°C, the 2.47%Mn alloy lies in single phase austenite region. This provides supporting evidence for $X_{822^\circ\text{C}}^{\gamma} = 2.4 \text{ w\%Mn} = 2.44 \text{ at \%Mn}$. Secondly, it yields a composition independent average diffusion coefficient of Mn in austenite (in the up-quenched state), i.e. $D_{822^\circ\text{C}}^{\text{Mn},\gamma} = 2.64 \times 10^{-14} \text{ cm}^2/\text{sec}$. This is in good agreement with the value of $5.6 \times 10^{-14} \text{ cm}^2/\text{sec}$ obtained from extrapolation of the high temperature measurements of Nohara and Hirano⁽⁴¹⁾.

V.4 Equilibration of a Surface Depleted Fe-Mn Alloy

An Fe-6.2%Mn alloy austenitized at 1100°C for 120 hr. in a vacuum sealed quartz tube develops a continuous composition profile (e.g. Figure (10)): the bulk concentration being 6.2%Mn in the middle and the surface concentration ~1% on either end, depending upon the size of the quartz tube and the temperature of austenitization. This surface concentration is the result of the equilibrium with manganese vapours in the quartz tube. Thus a semi-infinite diffusion couple is formed between the alloy with this surface concentration and that with the bulk concentration.

Figures (22a) and (22b) show the scanning electron micrographs of this sample, indicating equilibrated ferrite on the left end and austenite (in decomposed form) on the right. It may be noted that the metastable decomposed form of austenite changes with changing Mn content of the austenite.

Figure (23) is a composition profile of the Fe-6.2%Mn alloy austenitized at 1100°C for 120 hr, and followed by equilibration at 762°C. As the equilibration annealing proceeds the concentration of ferrite increases, transforming ferrite to austenite and thus pushing the α/γ interface to the right. The austenite in the immediate neighbourhood of the α/γ interface receives Mn from the right and, in turn, delivers to the ferrite on the left. In this process, the Fe-6.2%Mn alloy in the bulk appears to attain equilibrium with the austenite (with composition $X_{762^\circ\text{C}}^{\gamma}$), which is in equilibrium with ferrite. Thus the composition profile in austenite phase near the α/γ is relatively flatter, clearly marking $X_{762^\circ\text{C}}^{\gamma} = 4.55\text{w\%Mn} = 4.62$

at.%Mn; similarly on the ferrite side, as marked by arrows, $X_{762^{\circ}\text{C}}^{\alpha} = 1.95 \text{ w\%Mn} = 1.98 \text{ at.\%Mn}$. This confirms the end compositions of the tie line determined in the previous sections.

V.5 Summary of the Experimental and Theoretical Phase Diagram Results

Table (III) summarizes the experimental results obtained from the equilibration of the various diffusion couples. The number of check marks show the estimated relative degree of reliability in evaluation of the tie line end composition. In a given case the composition profile may be flatter allowing a more reliable evaluation of an interfacial composition than in other case and a phase fraction determined from lever rule application to the tie line determined from microprobe analysis may be more reliable than that determined from statistical analysis of a series of microstructures.

Using these tie line end compositions and the computational procedure described in the section III.1.3., $\Delta G_{Mn}^{O\alpha\rightarrow\gamma}$ as a function of temperature, i.e.,

$$\Delta G_{Mn}^{O\alpha\rightarrow\gamma} = -7359 + 5.519T \quad (47)$$

and the phase diagram together with the T_0 line have been calculated as shown in Figs. (24) and (25), respectively.

CHAPTER VI

DISCUSSION

The Fe-Mn phase diagram shown in Fig. (25) is thermodynamically self-consistent and in excellent agreement with the experimentally determined tie lines.

Admittedly, some error in the judgement of the interfacial austenite compositions may be involved due to the relatively steep concentration gradient (Figs. (14a), (14b)). However, this has not affected the statistical results of this study, as these compositions were confirmed by relatively more flat profiles, e.g., Figs. (20a) and (23).

The most likely systematic error in this study lies with the fact that the Ferrovac-E iron used in the preparation of Fe-Mn alloys for tie line experiments initially had 40 ppm carbon, 5 ppm nitrogen and relatively high oxygen (~100 ppm). It is supposed that the moist hydrogen treatment (at 890°C for 1 week, see p. 23) will have reduced the carbon substantially. Furthermore, during the equilibration period hydrogen (continuously flowing through the furnace tube outside the quartz capsule) easily diffuses into the quartz capsule due to the high diffusivity of hydrogen in quartz glass (10^{-6} cm²/sec⁽⁴³⁾ at 800°C). This assists the tie line experiments in two ways; firstly, the reducing atmosphere promotes good welding and scavenging of nitrogen and secondly the hydrogen on combining with oxygen in Ferrovac-E and Fe-Mn alloys could provide an oxidizing potential which scavenge carbon, particularly near the diffusion couple interface area. This is the region where the end

compositions of tie lines are measured at α/γ interfaces.

The chemical analyses of a section through the equilibrated diffusion couples for overall carbon and nitrogen content indicated $C \sim 0.003\%$ and $N \sim 0.001\%$. It should be realized that as these values lie close to the detection limit of the Stelco Method* ($\pm .002\%$) one can give little absolute weight to these C and N analyses. We estimate that at the worst the systematic error in the measured concentration X_{Mn}^{γ} due to interstitials is 0.04 w% and approximately equal to the statistical error of the measurement, which is to say negligible on the scale of Figure (25). This is not to say that such amounts may not be significant in kinetic measurements (see Part II).

It should finally be noted that our $X_{822^{\circ}C}^{\alpha}$ is in good agreement with that of Hillert et. al.⁽²⁾ Furthermore the results are consistent with the Vant Hoff relationship, which should be very accurate at this level of dilution. I.e., $\Delta^{\circ}G^{\alpha\rightarrow\gamma}/RT = X^{\gamma} - X^{\alpha} = 0.0108$ and 0.0260 at 822° and $762^{\circ}C$, respectively, from Table I as compared with our experimental values of 0.0109 and 0.0264 .

*A combustion method with an electrical conductivity measurement cell as the detection system for nitrogen analysis and an infrared absorption as the detection system for carbon analysis.

PART II - KINETICS

CHAPTER VII

INTRODUCTION

The study of manganese as an alloy addition in steel has long been of great technological interest. All commercial steels contain 0.3 to 0.8% Mn to counteract the deleterious effects caused by iron sulphide and to improve the hardenability of steels. Iron sulphide forms brittle, low melting point films around the steel crystals and causes the metal to crack during hot working, whereas in the presence of manganese, the sulphur prefers to combine as the less deleterious manganese sulphide. Hardenability is defined as a measure of the depth of hardness in a quenched steel. It may be noted that it refers to the relative ease of hardening and not to the value of hardness. A high value of hardenability means that higher temperature transformations are suppressed and hence a relatively lower rate of cooling can produce low temperature morphologies in the steel.

During the last two decades, intensive interest in high strength structural steels has focussed attention on the study of the microstructures and the associated mechanical properties of low-carbon-manganese steels. There has been a commercial tendency to increase the manganese content and decrease the carbon content in order to get a steel with higher toughness at a given strength level. The microalloying elements (Nb, V, Ti) added for precipitate strengthening also scavenge some carbon from the austenite.

In this part of the thesis, following a review of previous experimental and theoretical work, the various modes of decomposition of carbon free ($<0.01\%$) iron-rich Fe-Mn austenite will be examined with the objective of promoting an understanding of the ferrite morphology of structural steels. In particular, the experimental results on the kinetics of grain boundary ferrite formation will be discussed in terms of various theoretical models.

CHAPTER VIII

DISCUSSION OF PREVIOUS WORK

Iron-rich Fe-Mn austenite, on continuously cooling below the $\gamma/(\alpha+\gamma)$ phase boundary, decomposes to a low temperature product. The mode of decomposition of this austenite, resulting in a specific morphology, depends upon the manganese content of the alloy and the cooling rate used. The grain size of the parent austenite may also be included as a factor deciding the morphology of the product phase. However, the grain size of the austenite is not an independent factor, as it depends upon the composition of the alloy and the austenitizing process (the temperature and the duration of austenitization) following the mechanical treatment, if any.

Some basic information about the mode of decomposition of austenite has been obtained from the study of cooling curves in rapid quenching. Iron-manganese alloys containing up to 10% Mn have been studied over cooling rates ranging from a few degrees per second to 3×10^5 °C/sec⁽⁴⁴⁻⁴⁷⁾. Characteristically, the $\gamma \rightarrow \alpha$ start temperature, measured as an arrest point in the cooling curve, is depressed initially as the cooling rate is increased. This is an indication of isothermal kinetics of austenitic decomposition in this temperature range. On further increasing the cooling rate, Jzumiya et. al.⁽⁴⁵⁾ and Bolton and Petty⁽⁴⁶⁾ found a plateau region up to cooling rates of 5000°C/sec, whereas Shteynberg et. al.⁽⁴⁷⁾ found a series of four plateaus in the range of 100 to 300,000°C/sec (Fig. 26).

The $\gamma \rightarrow \alpha$ start temperatures corresponding to the only plateau obtained by Jzumiya et. al.⁽⁴⁵⁾ and Bolton and Petty⁽⁴⁶⁾ compare well with those corresponding to the second plateau of Shteynberg et. al.⁽⁴⁷⁾. This comparison is confirmed by the resulting microstructure being the same, i.e., apparently martensitic in both cases. The latter believe that the earlier workers missed the first plateau due to a relatively larger austenite grain size. The third and the fourth plateaus were not recorded, obviously due to the insufficiently high cooling rates employed. Shteynberg et. al.⁽⁴⁷⁾ also noted that on increasing the Mn concentration that some of these plateaus overlap, e.g., for 3.7% Mn alloy the third and fourth and for the 9.5% Mn alloy the second, third and fourth overlap Fig. (26). Shteynberg and his coworkers also observed similar behaviour in the case of pure Fe⁽⁴⁸⁾, Fe-Ni⁽⁴⁹⁾, Fe-Mo⁽⁴⁹⁾ and Fe-Cr⁽⁴⁹⁾ systems.

The microstructures in the alloys having up to 4.1% Mn resulting from the cooling rates corresponding to the first plateau, consist of nearly equiaxed grains bounded by irregularly shaped grain boundaries, apparently as a result of massive transformation. In all other cases (up to 10% Mn and cooling rates of 300,000°C/sec) a lath structure identified as martensite formed.⁽⁴⁷⁾ The increasing cooling rates led to the finer structures and to a greater relief effect. While Shteynberg et. al.⁽⁴⁷⁾ claim a distinction between the microstructures and the hardness values associated with their four plateaus, others have claimed that the operating modes of decomposition of austenite are only two. It may be recalled that only two plateaus were observed in pure iron by Bibby and Parr⁽⁴²⁾ and in Fe-Ni alloys by Swanson and Parr⁽⁵⁰⁾.

up to 55,000°C/sec; the first corresponding to the massive transformation and the second to the martensitic transformation. It is clear that as in pure iron⁽⁴²⁾ and Fe-Ni alloys,^(49,50) iron-rich Fe-Mn austenite decomposes either by the massive or martensitic route. The characteristics of massive and martensitic transformations will now be reviewed, briefly.

VIII.1 Massive Transformations

Massive transformations have been studied exhaustively by Massalski and his coworkers in numerous systems including Fe-Ni⁽⁵¹⁾ and Fe-Cr⁽⁵²⁾. Excellent reviews are available in the literature on this subject by Massalski^(53,54). The basic features of this mode of transformation are discussed below.

The microstructure of the product phase (in this case, massive ferrite) typically consists of 'massive' patchy grains surrounded by irregular boundaries of both planar and curved (wavy) kinds. It is this feature of the microstructure which provided the original name for the transformation^(55,56).

The crystal structure of the parent phase changes to that of the product phase while the composition is inherited unchanged. This transformation is of the nucleation and predominantly interface controlled growth type. The growth is thermally activated, occurring through short range (over a few atomic distances) diffusional jumps across the interphase boundary.

The lack of a crystallographic orientational relationship between the product and the parent phase has been considered as a characteristic of this transformation. This feature is supported by the experimental

evidence, in several systems studied by Massalski and his coworkers. However, Ayers and Joy⁽⁵⁷⁾ in their study of β (B.C.C.) to α_m (F.C.C.) massive transformation in Ag-Zn alloy have observed specific orientational relationships. Recently, Plitcha and Aaronson^(58,59) in their study of Ti-Ag, Ti-Au and Ag-Al alloys have also shown the existence of specific orientational relationships.

The relationship of this transformation to the phase diagram is best illustrated by the schematic phase diagrams of Fig. (27.I). It may be noted that the high temperature phase on cooling to the single phase region transforms to a different crystal structure while the composition remains invariant. This condition is met automatically in the case of allotropic transformations in pure elements. In the case of an alloy this condition is met at the T_0 line. However, since the growth in this transformation is thermally activated, it needs substantial undercooling (below T_0) to initiate observable amounts of transformation. Often this means the necessity of cooling the alloy down to the limit of the lower single phase region (the lower solidus). The massive transformation has, however, been observed in the two phase field of number of systems, viz., Fe-Ni⁽⁵¹⁾, Cu-Zn^(60,61), Cu-Al⁽⁶⁰⁾ and Ag-Cd⁽⁶¹⁾. The thermodynamics and the kinetics of this characteristic still remain a matter of debate.

Figure (27.II) shows the free energy change associated with the decomposition of a high temperature phase β at various temperatures within two and one phase (at low temperature, α) fields. The top portion of this diagram shows α and β solvus lines together with the T_0 line, and the bottom portion shows three pairs of free energy curves for

β and α phases at temperatures T_1 , T_2 and T_3 . An alloy of composition C in the β phase on cooling to T_1 (note that T_1 corresponds to $T_0(C)$, i.e., $G^\alpha = G^\beta$) can decompose into α and β of compositions α_1 and β_1 , respectively. At T_1 it cannot transform to α of composition C as for this reaction the free energy change is zero. As this alloy is cooled further to $T_2 < T_0(C)$ a choice of mode of decomposition opens up, i.e., it can decompose either to α_2 and β_2 (involving diffusion of solute) with a free energy change ΔG_e^2 or to α of composition C via massive transformation with a free energy change ΔG_m^2 . It may be noted that though $\Delta G_e^2 > \Delta G_m^2$, the actual mode of decomposition may be decided by kinetic factors. On cooling to T_3 (in the single phase α field) this alloy (of composition C in the β phase) transforms to α without any change in composition via the massive route. Hillert⁽⁶²⁾ has pointed out that in this situation the free energy change for one of the components may be of wrong sign, i.e., $G_A^\beta - G_A^\alpha > 0$ but $G_B^\beta - G_B^\alpha < 0$, Fig. (27 II), until some diffusion is allowed in the β matrix ahead of migrating interface allowing in turn a free energy construction so that the composition of β is displaced locally such that the tangents to G^α and G^β curves do not intersect.

Some understanding of the massive transformation has been achieved via its thermodynamic and kinetic treatment using the analogy between the massive transformation and solute drag on a moving grain boundary.

Following the pioneering work of Lucke and Detert⁽⁶³⁾, Cahn⁽⁶⁴⁾ and Lucke and Stuwe⁽⁶⁵⁾ further developed the theory for solute drag effect on a moving grain boundary. They considered the variation in interaction energy, E , between the solute and the boundary with the

variation in distance y of an atom from the middle of the boundary. They^(64,65) preferred to apply the model to a boundary with a wedge shaped energy well because such a shape simplifies the calculations. Considering only the energy aspects, it seems that the solute atoms in the boundary are not at rest; rather each is attracted towards the centre by a force given by $-dE/dy$.

The net force and the total drag is calculated by integrating over all the atoms. Thus, for a stationary boundary, because of the symmetric nature of solute distribution about the boundary, the net force is zero. On the other hand for a moving boundary the concentration profile is asymmetric exerting a net force on the boundary.

Cahn⁽⁶⁴⁾ obtained a relationship between the driving force (which is a function of composition, C and Temperature, T) and the velocity V resulting from the impurity drag effect. He assumed that there exists an intrinsic drag P_0 (due to factors other than impurities) for a pure specimen, and while considering an impure (alloy) specimen the variation in P_0 is negligible as compared to that in P_i (the extrinsic part of drag due solely to the impurities) relating velocity to composition, temperature and the driving force

$$P(V,C) = P_0(V) + P_i(V,C) \quad (48)$$

Cahn⁽⁶⁴⁾ concluded the following: (i) The solute drag does not depend upon the nature of solute/boundary interaction, i.e., attraction or repulsion. (ii) There exist two distinct branches of driving force versus velocity curve (Fig. (28)), i.e., for a given driving force the reaction can follow either a slow branch or a fast

one. It should be noted that for the pure specimen the velocity varies linearly with the driving force whereas there exists a transition from linear (slow branch) to a non-linear (fast branch) relationship with increasing concentration of impurity.

Hillert⁽²⁶⁾ in his theory preferred to operate upon the free energy of the solute, in contrast to internal energy used by Cahn⁽⁶⁴⁾. Here it is self-evident that the net force on the solute atoms is zero when they are in equilibrium. He argued that the work put into the movement of a boundary in order to overcome the solute drag must dissipate by the diffusion of solute taking place as a result of the boundary movement.

It should be noted that in these models of the impurity drag effect on the moving boundary an implicit assumption is that the diffusion rate along the boundary is infinite resulting in a planar grain boundary with uniform concentration in the plane of boundary.

Roy and Bauer⁽⁶⁶⁾ have considered the deviation from the planar nature of the boundary, which, due to diffusive and convective fluxes, causes a non-uniform distribution of impurities in the boundary. The convective flux arises when the net boundary motion is not perpendicular to the boundary plane and the diffusive flux is due to a non-uniform concentration gradient. Furthermore a non-uniform distribution of impurities gives rise to a non-uniform drag on the boundary causing a non-planar grain boundary configuration. These two factors are coupled and can lead to stable or unstable boundary shapes, depending upon the details of the process.

Hillert and Sundman⁽⁶⁷⁾ have developed a theoretical kinetic treatment of the massive transformation in a binary alloy. They obtained the following expression for the rate of free energy dissipation (given as the product of the flux and the driving force) per mole of the solution due to the diffusion of solutes.

$$\frac{\Delta G_{S.D.}}{\Delta t} = \frac{RTAv^2}{V_m} \int_{-\infty}^{\infty} \frac{(X_B - X_B^0)^2}{DX_A X_B} dy \quad (49a)$$

where v is the velocity of the moving phase boundary of cross-section A which passes through 1 mole of solution during time Δt such that $Av\Delta t = V_m$, V_m is the molar volume, X_B^0 is the bulk composition of the alloy, X_B is the composition of the alloy at location y from the centre of the phase boundary ($X_A = 1 - X_B$) and D is the diffusion coefficient of the solute in the boundary. One can express equation (49a) in terms of an integral involving dimensionless parameters, i.e.,

$$\frac{\Delta G_{SD}}{\Delta t} = \frac{RTAv}{V_m} \left(\frac{v\delta}{D_0}\right) f \quad (49b)$$

where

$$f = \int_{-\infty}^{\infty} \frac{(X_B - X_B^0)^2 d(y/\delta)}{(D/D_0) X_A X_B} \quad (49c)$$

δ is the width of the phase boundary and D_0 is the bulk diffusion coefficient of the solute. D/D_0 may vary with the parameter y/δ depending upon the model chosen for the phase boundary diffusion. Using an ideal solution model and an appropriate standard state such that the Henry's law coefficient is unity, the chemical potential or partial molal

free energy for each component may be written as follows:

$$\mu_B = {}^0G_B + RT \ln X_B \quad (50a)$$

and

$$\mu_A = {}^0G_A + RT \ln X_A \quad (50b)$$

For the case of low velocity, which is of concern in this study, using the thermodynamic and diffusion model of Hillert et. al.⁽⁶⁷⁾ the ideal approximation for the driving force is given as

$$\frac{d(\mu_B - \mu_A)}{dy} = \frac{d({}^0G_B - {}^0G_A)}{dy} + \frac{RT}{X_A X_B} \frac{dX_B}{dy} = - \frac{RTv}{D} \frac{(X_B - X_B^0)}{X_A X_B} \quad (51a)$$

which in the limit of zero force or velocity becomes

$$\frac{dX_B}{dy} = - \frac{X_A X_B}{RT} \frac{d({}^0G_B - {}^0G_A)}{dy} \quad (51b)$$

Hillert⁽⁶⁷⁾ considered the boundary as a thin film of a special phase having its own free energy curve such that at equilibrium a characteristic amount of segregation is established. Thus by assuming equilibrium segregation coefficients (for the solute) for growing ferrite to boundary and boundary to parent austenite $d({}^0G_B - {}^0G_A)/dy$ is defined. Furthermore, steady state composition profiles as shown in Figure (29) can be evaluated using equation (51a). One can evaluate the solute drag by simultaneously using equations (51a) and (49b). In the low velocity ($v\delta/2D < 0.1$) approximation which we will be subsequently using, the term in equation (51a) with v only enters weakly into the integral of (49a) in comparison to the v^2 coefficient. Accordingly we are justified in using equation (51b) in the evaluation

of f (equation (49c)). We have verified that the thermodynamics, the kinetics and the evaluation of the dissipation of free energy in solute drag by Hillert and Sundman⁽⁶⁷⁾ are self consistent.

The latter authors⁽⁶⁷⁾ in agreement with Cahn⁽⁶⁴⁾ have found that (i) the total solute drag is independent of whether the solute is attracted or repelled by the boundary, and (ii) an optimum (maximum) in total solute drag exists with respect to the velocity of the boundary.

The dissipation expression (49b) can be related to the driving free energy attending a massive transformation per unit volume, ΔF , as follows. Firstly, it is necessary for theoretical consistency with the steady state free energy balance to propose that a part of the total free energy available ΔF_0 , (Measured in terms of the undercooling below T_0) is stored in the product phase as a characteristic defect concentration, such that

$$\Delta F = \Delta F_0 \left(1 - \frac{S_0^2}{S^2}\right) \quad (52)$$

where $1/S^2$ is the defect density (number of defects per cm^2) and $1/S_0^2$ is a limiting density at given T .^{*} Now considering the free energy balance for the steady state one may write

$$\Delta G_{S,D.}/\Delta t = V_m \Delta F/\Delta t$$

or

$$\Delta G_{S,D.}/\Delta t = Av\Delta F \quad (53)$$

Using equation (49b), (52) and (53) one obtains

$$v = V_m \left(\frac{\Delta F_0}{RT}\right) \left(\frac{D_0}{\delta}\right) \frac{1}{f} \left(1 - \frac{S_0^2}{S^2}\right) \quad (54)$$

* It is implied that at high phase boundary velocity when the solute spike cannot be sustained, most free energy for the transformation is stored in the product phase in the form of defects.

It has been shown by computation via (51b) and (49c) for $v \rightarrow 0$ that f decreases for an increasing value of D/D_0 in the boundary. We now postulate that D is monotone with $1/S^2$ on the physical basis that a more defective (or higher D) boundary should correspond to a higher inheritance of defects in the product phase. Thus, in turn, f is monotone with S . It is well-known that this form of v relationship (54) results in a typical C shape for the TTT curve⁽⁶⁸⁾. In this case the asymptote as $t \rightarrow \infty$ would be T_0 .

For the steady state the rate of entropy production per unit volume, σ , at a given temperature, T , can be expressed as:

$$T \cdot \sigma = \frac{Av}{V_m} \Delta F \quad (55)$$

or

$$\sigma = \left(\frac{A}{RT^2} \right) \left(\frac{D_0}{\delta} \right) \frac{\Delta F_0^2}{f(S)} \left(1 - \frac{S_0^2}{S^2} \right)^2 \quad (56)$$

If with Kirkaldy and Sharma⁽⁶⁸⁾ we identify the stable state with a maximum in the entropy production then the stable defect density can be obtained via $f(S)$ evaluated from the Hillert and Sundman⁽⁶⁷⁾ theory ($v \rightarrow 0$) and a model relating D in the boundary to the defect density in the product phase. For large v , the optimization becomes much more complicated since v through equation (51a) then appears explicitly under the integral sign in equation (49c).

VIII.2 Martensitic Transformations

Although numerous reviews on this subject are available in the literature⁽⁶⁹⁻⁷²⁾, it is very difficult to single out a characteristic of this transformation which can be used to identify it. Some of the basic features of this mode of transformation are presented below.

The shape revealed by the rumpling of a polished surface, caused by the shear of the transformed region, has long been used as a criterion to identify the martensitic reaction. This has been contested by the existence of a non-martensitic Widmanstätten ferrite formation which shows surface rumpling⁽⁷³⁾.

In this transformation the crystal structure changes while the composition is inherited unchanged, a feature in common with the massive transformation. The transformation takes place by nucleation and homogeneous shear of the transformed region produced by the movement of a coherent or nearly coherent interface resulting in a definite crystallographic orientational relationship between the parent and the product phase. It may be noted that no thermally activated diffusion is involved in this mode of transformation.

Following this transformation two types of morphologies result, viz., lath martensite and plate martensite. In lath martensite the transforming unit takes the shape of a lath. Each lath is a result of a homogeneous shear and successive shears produce a packet of parallel laths containing a high density of tangled dislocations. It is this morphology that forms in dilute alloys of iron. The plate martensite differs in the shape taken by a transformation unit and its transformation sequence is characterized by nonparallel plate formation.

(Note that the microstructural features are completely different from those characteristic of the massive transformation).

The relationship of this transformation to the phase diagram is similar to that of the massive transformation, except that it generally takes a higher undercooling to generate this mode of decomposition.

CHAPTER IX

EXPERIMENTAL

Alloys of up to Fe-6.2% Mn and Fe-1.5% Mn-0.25% Mo (using Mo of 99.9% purity) were melted and homogenized as described in Part I. The experiments to study the kinetics of the decomposition of austenite were divided in two parts: continuous cooling and isothermal transformation tests.

IX.1 Continuous Cooling Tests

With the objective of obtaining a general semiquantitative survey of the microstructures resulting from the decomposition of Fe-Mn and Fe-Mn-Mo austenite, samples of 10 mm x 5 mm x 1 mm size were autenitized in a vacuum (5×10^{-5} torr) sealed in quartz tubes at various temperatures for 30 min and then transformed at different cooling rates ranging from $\sim 2^\circ\text{C}/\text{min}$ to $\sim 10^5^\circ\text{C}/\text{min}$.

The slowest cooling rate ($2^\circ\text{C}/\text{min}$) was obtained by allowing the sample to cool in the furnace (with the power turned off). To obtain higher cooling rates a vertical furnace was used. A weight was attached to the outer top end of the capsule such that on dropping the latter, the weight would break the capsule instantly. Using this technique, a cooling rate of $\sim 10^3^\circ\text{C}/\text{min}$ was obtained by dropping the capsule into ambient air and $10^5^\circ\text{C}/\text{min}$ was obtained by dropping it in a bucket containing an iced brine solution. The air cooling rate was determined in a separate experiment, in which a Pt/Pt-13% Rh thermo-

couple was spot welded to the sample.

These samples, heat treated according to different schedules, were examined for microstructure using optical, scanning and transmission electron microscopy. The crystal structures of such transformed samples were examined using X-ray diffractometry. Furthermore, to further characterize the microstructures, microhardness values were recorded using the Tukon microhardness tester.

In the beginning of this study, an attempt was made to examine the massive transformation in Fe-Mn alloys using the crossing of thermally etched prior austenite boundaries by the subsequently formed ferrite boundaries, an experimental technique frequently used by Massalski and his coworkers^(51,52). This technique did not succeed in the case of the Fe-Mn system, since during thermal etching, the surface concentration of Mn in these samples always decreased due to the preferential evaporation of Mn. The microstructure of such Mn-depleted samples (Fig. (10)) was studied to some effect by gradually removing the surface layers by mechanical polishing. Also a microstructural and microprobe examination of the cross-section provided a means of the study of the response to continuously varying composition to a given cooling rate, using only one sample. This is complimentary to a Jominy End Quench experiment wherein one studies the response to continuously varying cooling rates in one sample of a given composition.

IX.2 Isothermal Transformation Tests for Grain Boundary Ferrite Formation

For the quantitative study of the isothermal transformation kinetics, a salt bath having 85% BaCl_2 and 15% NaCl was used for austenitizing at 1040°C for 30 minutes and one having 55% BaCl_2 , 25% NaCl and 20% KCl was used for isothermal treatments. The temperature of these samples was measured with a chromel-alumel thermocouple spot welded to the sample and was found to be stable within $\pm 3^\circ\text{C}$ over a period of one hour. The fraction of grain boundary ferrite formed in this study was determined using linear intercepts on optical micrographs. Approximately, $5 \pm 2\%$ ferrite formation was used as the criterion for the TTT start curve.

CHAPTER X

RESULTS AND DISCUSSION

X.1 Continuous Cooling Tests

Figures (30a-i) is a compendium of microstructures obtained in 1 mm thick Fe-Mn alloys as a result of variations in the composition, viz., 2% to 6.2% Mn, and the cooling rate ranging from 2° to $\sim 10^5^\circ\text{C}/\text{min}$. for a given austenitizing treatment, i.e. holding at 950°C for 30 min. The competing morphologies are as follows:

- (i) equiaxed ferrite with mostly planar grain boundaries forming in the alloys of low Mn concentration at a relatively low cooling rate, viz., in 2% Mn alloy cooled at $2^\circ\text{C}/\text{min}$.
- (ii) ragged ferrite forming in leaner alloys at higher cooling rates, viz., in 2% Mn alloy at $10^5^\circ\text{C}/\text{min}$ or in richer alloys at lower cooling rate, viz., in 4% Mn alloy at $2^\circ\text{C}/\text{min}$.
- (iii) lath morphology forming in lean alloys at very high cooling rates or in richer alloys at low cooling rate, viz., in 6.2% Mn alloy at $1000^\circ\text{C}/\text{min}$.

For certain combinations of the alloy composition and cooling rate a mixture of equiaxed and ragged ferrite morphologies is observed (Figures (30b and c)) and for richer alloys ragged ferrite and lath morphology compete (Figures (30d-i)), the latter increasing at the expense of the former with increase in either of the alloy content and cooling rate.

Figure (31a), an optical micrograph at higher magnification (x250) corresponding to (30e), shows a mixture of ragged ferrite and lath morphology. Figure (31c) is a scanning electron micrograph of a portion of (30f) showing the lath morphology and Figure (31d) is for an alloy of composition Fe-1.5%Mn-0.25%Mo whose 0.1 mm thick sample was austenitized and then quenched in water. Figures (32a-c) are transmission electron micrographs corresponding to (30a), (30e) and (31d), respectively. The transmission electron micrographs, indicate the increasing order of defect densities in equiaxed, ragged ferrite and lath morphologies. Similar structures have been observed in the Fe-Mn system by Bolton and Petty⁽⁴⁶⁾ and Roberts.⁽⁷⁴⁾ The microstructural similarity between the lath morphology in the Fe-Mn system and that in low C, Fe-C martensite⁽⁷³⁾ should be noted.

These observations draw attention to two facts: firstly, that for a given alloy composition, say 2% Mn, the critical cooling rate for ragged ferrite formation is higher than that for equiaxed ferrite, and similarly for the 4% Mn alloy, the critical cooling rate for lath morphology is higher than that for ragged ferrite; secondly, that with increase in Mn concentration the critical cooling rates for ragged ferrite and lath morphology decrease, a simple hardenability effect.

The number on the lower left corner in each of the micrographs in Figures (30a-i) represents the microhardness associated with a given microstructure. It should be noted that the microhardness values associated with equiaxed, ragged ferrite and lath morphology are in increasing order due perhaps to the increasing fineness of the

structure and the defect density. The microhardness strongly depends upon the kind of morphology. These microhardness values compare well with those measured by others in Fe-Mn⁽⁴⁷⁾ and Fe-Ni⁽⁷⁵⁾ systems.

It is to be noted that in our continuous cooling tests the cooling rates correspond to the first plateau of Shteynberg et. al.⁽⁴⁷⁾ (Fig. (26)).

The lath morphologies shown in Figures (30 f-i), (31 a,c,d) and (32c) resemble those resulting from the martensitic transformation in low C, Fe-C alloys⁽⁷³⁾. Furthermore, the microhardness of the lath morphology, viz., DPH 287 for (30i) agrees well with that for Fe-C martensite extrapolated to zero carbon level (\sim DPH 300)⁽⁷⁶⁾. Figure (31b) shows the surface rumpling produced on an Fe-6.2%Mn prepolished alloy sample vacuum sealed in a quartz tube, austenitized at 900°C for 10 minutes and followed by the unbroken capsule thrown in water. This surface rumpling suggests a shear mode of transformation.

Although the alloy composition and the cooling rates used in this study place them on the first plateau of Shteynberg et. al.⁽⁴⁷⁾ which corresponds to massive transformation, it is nonetheless possible that due to the differences in prior austenite grain size the regimes of massive and martensitic transformations (in terms of cooling rates) are shifted to lower cooling rates leading to lath morphology as a result of martensitic transformation.

The composition of these alloys affect the microhardness in two ways, firstly as a result of solution hardening and secondly as a result of the finer austenite decomposition product with greater defect density due to the lowering of γ to α transformation temperature. It is to be realized that it is very difficult to isolate the effect

of variation in composition from that in morphology. A ternary alloy of composition Fe-1.5%Mn-0.25%Mo was water quenched to yield lath morphology (Figs. (31d) and (32c)), similar to that reported as acicular ferrite in HSLA steels^(77,78).

These alloys of the Fe-Mn system, having different ferrite morphologies, were analyzed for crystal structure, using X-ray diffractometry. It was found that irrespective of the morphology, the crystal structure is body-centred cubic. A texture effect was prominent in quenched alloys resulting in a decrease in the intensities of (110) and (220) reflections. There was no evidence for tetragonal distortion or retained austenite, due to the very low carbon content of these alloys.

Figure (33a) is a composite figure of a scanning electron micrograph and corresponding electron microprobe trace of a surface depleted (during austenitization at 1100°C for 24 hr.) and furnace cooled (2°C/min) sample of Fe-6.2%Mn alloy. This experiment shows the effect of variation in composition of the alloy on the resulting morphology, for a given cooling rate. Figure (33b) is a scanning electron micrograph at a higher magnification of the same region as shown in Fig. (33a). In Figure (33a) A-A is the maximum solubility limit of Mn in ferrite, i.e., on the left of A-A lies the single phase, α , region and on the right the two phase, $\alpha+\gamma$, region. It is seen that the equiaxed ferrite with mostly planar grain boundaries extends up to the ferrite solvus line (A-A) beyond which ragged ferrite and lath morphologies extend up to the bulk composition. Here two points deserve attention: first that there exists a sharp boundary between equiaxed and ragged ferrite, approximately at the ferrite solvus limit, and second that ragged

ferrite formation starts within the two phase, $\alpha+\gamma$, region and extends well into it.

Considering an irregular shape of ferrite grains with ragged boundaries and composition invariance as criteria for massive mode of decomposition Figure (33a) establishes that the massive mode of decomposition takes place in the two phase field of the Fe-Mn system. This situation correspond to the slow branch of impurity drag treatment of Cahn⁽⁶⁴⁾. It may be recalled that the massive mode of transformation in the two phase field has been reported in Fe-Ni⁽⁵¹⁾, Cu-Zn^(60,61), Cu-Al⁽⁶⁰⁾, and Ag-Cd⁽⁶¹⁾ systems.

X.2 Isothermal Transformation Tests for Grain Boundary Ferrite Formation

Alloys of Fe-2%Mn and Fe-2.8%Mn were subjected to isothermal transformation tests near their respective ferrite solvus temperatures for exploratory purposes. It was found that the nose-time for the C-curve for grain boundary ferrite formation for the Fe-2%Mn alloy was less than 1 min. and for the Fe-2.8%Mn alloy was less than 5 min. Thus in order to have more accurately measurable transformation periods the alloy Fe-3.1%Mn (close to the maximum solubility limit of Mn in ferrite) was chosen for TTT examination. For this alloy the nose time is observed to be 15 minutes at 640°C.

Figures (34a-b) show the micrographs of Fe-2.8%Mn and Fe-3.1%Mn alloys isothermally treated at 675°C for 10 min. and 620°C for 27 min., respectively, at relatively high magnification for estimation of the fraction of grain boundary ferrite formed. Figures (35a-h) show micrographs of Fe-3.1%Mn alloy isothermally treated at different temperatures for different lengths of time. Figure (36) shows the partial TTT start curves for Fe-2%Mn and Fe-2.8%Mn alloys and a complete TTT start curve for the Fe-3.1%Mn alloy for 5±2% grain boundary ferrite formation.

The TTT start curve for the Fe-3.1%Mn alloy shown in Figure (36) draws our attention to three points.

(i) The transformation on cooling starts only after reaching close to ferrite solvus (indicated by T^{α} on this figure). This feature was

observed also by Karlyn et. al.⁽⁷⁹⁾ in the Cu-Zn system. Furthermore, it may be recalled that the equiaxed ferrite formation extended up to the maximum ferrite solvus limit, as shown in Figure (33a). This suggests that this grain boundary ferrite is the analog of the equiaxed ferrite in a uniform solution.

It should be noted that our continuous cooling tests (except for furnace cooling) correspond to cooling curves lying close to the temperature axis (Figure (36)). Thus, for the Fe-2%Mn alloy (for which the nose time is less than 1 minute) equiaxed ferrite formation is seen in furnace cooled and air cooled samples, whereas in a water quenched sample it seems to be suppressed as the cooling curve for this sample misses the nose of the TTT curve. The other alloys Fe-4%Mn and Fe-6.2%Mn may have their TTT nose shifted to far right in Figure (36) resulting in complete suppression of equiaxed ferrite in these alloys.

(ii) The TTT start curve bends backward in a C shape. Karlyn et. al.⁽⁷⁹⁾ using a pulsed heating and metallographic technique observed that the rate of transformation increased monotonically with undercooling together with a C shaped delay time in the Cu-Zn system. They identified this delay time with the time taken for interface control to take over the initially diffusion controlled growth process and not with the actual nucleation of the α particles. Ayers and Massalski⁽⁸⁰⁾ using pulsed heating and continuous resistivity measurements did not

observe any delay time for this system. Bolton and Petty⁽⁴⁶⁾ observed isothermal transformation kinetics in an Fe-3.78%Mn-.012%C alloy and they identified this as a bainitic transformation.

(iii) The low growth rate ($\sim .01 \mu\text{m}/\text{sec}$) of grain boundary ferrite observed in this study of Fe-Mn alloys is suggestive of a diffusion controlled reaction.

We first explore the possibility of volume diffusion of Mn as the rate controlling step. this situation is described by equation (28) of section III.2.2. For a positive value of n^γ equation (28) is modified to

$$n^\gamma = \frac{1}{\sqrt{\pi}} \frac{C^{\gamma\alpha} - C^{\text{II}}}{C^{\gamma\alpha} - C^{\alpha\gamma}} \frac{e^{-(n^\gamma)^2}}{1 - \text{erf}(n^\gamma)} \quad (57)$$

and noting that for high supersaturation $n^\gamma \gg 1$ then we can approximate

$$1 - \text{erf}(n^\gamma) = \frac{e^{-(n^\gamma)^2}}{n^\gamma \sqrt{\pi}} \left[1 - \frac{1}{2(n^\gamma)^2} \right] \quad (58)$$

Now from equations (57), (58) and (22) the ferrite thickness is

$$\xi = \sqrt{2D^\gamma t \left[\frac{C^{\gamma\alpha} - C^{\text{II}}}{C^{\text{II}} - C^{\alpha\gamma}} \right]} = \sqrt{2D^\gamma t R} \quad (59)$$

On substituting into equation (59) values for the observed grain boundary ferrite formation, i.e., $\xi = 16 \mu\text{m}$ at 650°C for 20 minutes, $D_{650^\circ\text{C}}^{\text{Mn},\gamma} = 2.6 \times 10^{-15} \text{ cm}^2/\text{sec}$ (extrapolated from the higher temperature data of Nohara and Hirano⁽⁴¹⁾) and assuming that the

nucleation is instantaneous (i.e. the kinetics is growth controlled), the minimum concentration ratio, R , needed (cf. equation (59)) is

$$R = \frac{C^{\gamma\alpha} - C^{II}}{C^{II} - C^{\alpha\gamma}} = 10^6 \quad (60)$$

This means that the height of the spike in austenite should be 10^6 times larger than the deficit in ferrite, as shown in figure (37). Since $C^{\gamma\alpha} - C^{II} = 0.1$ in our case then $C^{II} - C^{\alpha\gamma} = 10^{-7}$. Using the mass balance, the hatched area on the ferrite side should be equal to the cross-hatched area on the austenite side. Consequently the width of the spike in austenite, $x = 10^{-7} \times 16 \times 10^{-4} / .05 = 3 \times 10^{-9}$ cm, is an order of magnitude smaller than the boundary width. This suggests that the diffusion of Mn should take place mostly in the boundary region.

Nonetheless if we consider that in the neighbourhood of the boundary the bulk diffusion coefficient may be 10 to 100 times larger than that far away from the boundary, the width of the spike in the austenite phase could be larger than the boundary width, resulting in bulk diffusion of Mn as a rate controlling step. In this situation the TTT start curve with asymptote at the $\gamma/(\alpha+\gamma)$ solvus could describe the actual growth rate at large undercooling. However, it should be noted that no Mn partitioning was detected by the microprobe step scan analysis both along and across the grain boundary ferrite precipitates. Furthermore, the observed TTT curve does not have its asymptote at $\gamma/(\alpha+\gamma)$ solvus.

We now explore the possibility that there are sufficient interstitial atoms to force the reaction into the ternary diagram (Fe-Mn-(C,N)) and thus provide a temperature region of control by these interstitials (C and N). The kinetics of interstitial diffusion controlled reaction can be evaluated by referring to criterion (33). However, noting that at 650°C the diffusion coefficient of carbon $D_{650^\circ\text{C}}^{\text{C},\gamma} = 1.96 \times 10^{-8} \text{ cm}^2/\text{sec}^{(81)}$, the diffusion length for carbon in austenite for 20 minutes is

$$x = \sqrt{2 \times 1.96 \times 10^{-8} \times 20 \times 60} = 68 \text{ } \mu\text{m} \quad (61)$$


as compared to the observed grain boundary ferrite thickness of 16 μm . Although x should be discounted by a supersaturation factor it is nonetheless several orders of magnitude higher than the interface boundary width, indicating that the trace interstitial impurities like C and N may be rate controlling in this process. Furthermore the conjecture of interstitial diffusion control can be supported by the fact that the observed TTT start curves (c.f. Fig. (36)) point to asymptote at or near the respective $(\alpha+\gamma)/\alpha$ solvus temperatures for the binary Fe-Mn system (c.f. Fig. (25)).

To discuss this phase transformation behaviour in relation to the phase diagram, we shall consider a ternary Fe-Mn-C system (for sake of simplicity of the discussion) and not the quaternary Fe-Mn-C-N. It is assumed that the trace concentration of oxygen will be in the combined form of manganese oxide. Figures (38a,b) show the approximate Fe-Mn-C isothermal sections of the phase diagram at 660° and 600°C, respectively. The terminal binary limits for the Fe-Mn and the Fe-C

systems are taken from the present study and that of Harvig,⁽²¹⁾ respectively. These terminal points are connected by straight lines as approximate phase boundaries for the α/γ equilibrium. True equilibrium, para-equilibrium phase boundaries and the envelope of zero partition are shown in Figures (38a, b) following the construction of Figures (6a,b) and (7). The region of low C content of present concern is shown separately on an expanded scale, Figures (38a,b).

The Fe-3.1%Mn alloy austenitized at 1040°C for 30 min. and isothermally treated at 640°C for 30 min. was analysed for carbon and nitrogen and each was found to be .004% with an accuracy of $\pm 0.002\%$. Conjecturing that the effect of nitrogen on the constitution of Fe-Mn system is the same as that of carbon, we shall assume that there is a linear additive effect of C and N. Thus the effective alloy composition is Fe-3.15 at %Mn-0.04 at %C as shown by the open circle in Figures (38a,b). Note that points P lie outside the paraequilibrium range and within the no-partition local equilibrium range.

Figure (39) shows a set of schematic ferrite/austenite boundaries for the Fe-Mn-C isotherms for the temperature $T_1 > T_2 > T_3$ and the bulk alloy composition (O) marked as P. Following the construction described in the section III.2.3. (Fig. (6a)) the envelope of zero partition and the self consistent tie-lines (C_1M_1 and C_2M_2 at T_1 and T_2 , respectively) are located on Fig. (39). At temperature T_1 , the alloy composition P lies very close to A_1E_1 , the envelope of zero partition of T_1 , implying a low supersaturation (corresponding to C_3P) for carbon diffusion (controlling austenite to grain boundary ferrite



transformation) ahead of austenite. This condition corresponds to low transformation rates or long times required for a given % transformation at this temperature. As the temperature is lowered to T_2 the alloy composition lies close to the ferrite solvus, A_2B_2 , resulting in high supersaturation (corresponding to C_4P) for carbon diffusion. This condition leads to a high transformation rate or short times for a given % transformation at this temperature, T_2 . On further cooling to T_3 , the alloy composition P falls within the single phase region and could thus transform via the massive mode without any necessity of partitioning of Mn or C.

It is to be noted that should carbon diffusion alone be controlling the rate of transformation for the complete TTT of Fe-3.1%Mn in Fig. (36), the 'nose' of this TTT curve could not be so sharp. This leads to the proposition that there exists a competitive massive mode of decomposition which defines the cut-back of the TTT curve. However, due to the relative faster transformation rate for the massive mode in the high temperature range, it is the carbon diffusion ahead of the interface in austenite which controls the transformation rate above the nose.

Transformation curves for the massive mode have been constructed as follows. According to the most common version of the model of interface control, the migration rate of the interface,

$$v \propto M \Delta G_m^B \quad (62)$$

where M is the mobility of the interface and ΔG_m^B is the free energy per unit mole of solution dissipated in the interface. (Our own theory

would give a similar result, c.f. eq. (54)). Thus the time to form a given fraction of grain boundary ferrite

$$t \propto \frac{1}{M \Delta G_M^B} \quad (63)$$

Since the mobility has an activation term and ΔG_M^B may be estimated as being proportional to $(T_0 - T)$ equation (63) can be rewritten as

$$t = k e^{Q/RT} / (T_0 - T) \quad (64)$$

where k is slowly varying with temperature. We have used this coefficient to force the transformation curve (for massive mode) through the nose of the TTT curve. Q is the activation energy per unit mole of the solution for the thermally activated atomic process in the interface. It was set equal to 30,000 cal./mole, typical of the grain boundary diffusion coefficient of a substitutional element.

Now the complete transformation behaviour of Fe-Mn austenite to grain boundary ferrite may be visualized as follows. The transformation curve for the massive mode, shown as the broken line in the Figure (36), starts with an asymptote at T_0 . As the undercooling increases the massive reaction can speed up, but the trace impurity diffusion controlled part of the transformation being much slower determines the actual rate of transformation. This behaviour may continue till the nose of experimental TTT curve is reached. On cooling below the nose temperature the driving force for C diffusion is now much larger (shown schematically as C_4P in Fig. (39)) transferring the rate control to the massive transformation (dot-dash line)

curve corresponding to the 'slow branch' of the impurity drag effect in grain boundary migration.

CHAPTER XI
CONCLUSIONS

1. The end compositions of the tie-lines for α/γ equilibrium at 762° and 822°C in the iron-rich Fe-Mn system have been measured using a diffusion couple, technique. The end-point values are $X_{762^\circ\text{C}}^\alpha = 1.98$ at. %Mn, $X_{762^\circ\text{C}}^\gamma = 4.62$ at. %Mn, $X_{822^\circ\text{C}}^\alpha = 1.35$ at. %Mn and $X_{822^\circ\text{C}}^\gamma = 2.44$ at. %Mn.
2. The analyses of the composition profiles for the equilibrated diffusion couples yielded $D_{762^\circ\text{C}}^{\text{Mn},\alpha} = 2.7 \times 10^{-12}$ cm²/sec and $D_{822^\circ\text{C}}^{\text{Mn},\gamma} = 2.64 \times 10^{-14}$ cm²/sec.
3. Using the experimental tie-line information from this study and other sources, and the thermodynamic data from the literature a thermodynamically self-consistent phase diagram together with T_0 line has been calculated for the iron-rich Fe-Mn system (see Fig. (25)).
4. The competing morphologies resulting from the decomposition of iron-rich Fe-Mn austenite are equiaxed, ragged ferrite and lath morphology. The former two may result from the massive mode of transformation, whereas the last one may be a result of martensitic decomposition.
5. The massive mode of decomposition has been observed in the Fe-6.2%Mn sample which lies in the two phase field of the Fe-Mn phase diagram.

6. The solute drag treatment of Hillert and Sundman⁽⁶⁸⁾ has been further developed for the low velocity branch. Our treatment predicts a C-shaped TTT (time-temperature transformation) curve following the massive mode of transformation. Furthermore, invoking irreversible thermodynamics it has been noted that the rate of entropy production has an optimum with respect to a structure parameter, S . I.e., for a given free energy of transformation there exists a unique optimum defect density and velocity associated with a massive transformation. To make such a theory quantitative it will be necessary to develop a detailed model of the relationship between the boundary and the product phase defects.

7. A TTT diagram has been experimentally evaluated for a grain boundary ferrite (analog of equiaxed ferrite) formation in the Fe-3.1%Mn alloy, with nose time 15 minutes at 640°C.

8. The grain boundary ferrite formation starts only upon reaching close to the (lower) single phase solidus.

9. The TTT observations are generally consistent with the proposition that the austenitic decomposition to grain boundary ferrite is controlled and drastically limited by trace carbon diffusion above the nose temperature and by the massive mode at lower temperatures.

REFERENCES

1. A.R. Troiano and F.T. McGuire: Trans. ASM, 1943, vol. 31, p. 340.
2. M. Hillert, T. Wada and H. Wada: JISI, 1967, vol. 205, p. 539.
3. J.B. Gilmour, G.R. Purdy and J.S. Kirkaldy: Met. Trans., 1972, vol. 3, p. 1455.
4. C. Wagner: Thermodynamics of Alloys, Addison-Wesley, Reading, Mass., 1952, p. 51.
5. G. Kirchner, T. Nishizawa and B. Urhenius: Met. Trans., 1973, vol. 4, p. 167.
6. J.F. Butler, C.L. McCabe and H.W. Paxton: Trans. TMS-AIME, 1961, vol. 221, p. 479.
7. J.H. Smith, H.W. Paxton and C.L. McCabe: Trans. TMS-AIME, 1961, vol. 221, p. 895.
8. P. Roy and R. Hultgren: Trans. TMS-AIME, 1965, vol. 233, p. 1811.
9. R. Smith and R. Shuttleworth: Acta Met., 1965, vol. 13, p. 623.
10. V.N. Eremenko, G.M. Lukashenko and V.R. Sidorko: Izv. Akad. Nauk, USSR, Metal., 1969, No. 2, p. 170.
11. J.S. Kirkaldy and G.R. Purdy: Can. J. Phys., 1962, vol. 40, p. 202.
12. R. Hultgren, R.L. Orr, P.D. Anderson and K.K. Kelly: Selected Values of Thermodynamic properties of Metals and Alloys, Berkley, 1963, 726.
13. R.L. Orr and J. Chipman: Trans. TMS-AIME, 1967, vol. 239, p. 690.
14. H. Johansson: Arch. Eisenh., 1937, vol. 11, 241.
15. L. Kaufman, E.V. Clougherty and R.J. Weiss: Acta Met., 1963, vol. 11, 323.
16. L.S. Darken and R.P. Smith: Ind. Eng. Chem., 1951, vol. 43, 1815.
17. J.C. Fisher: Trans. AIME, 1949, vol. 185, 688.
18. C. Zener: Trans. AIME, 1946, vol. 167, 513.
19. R. Kohlhaas and M. Braun: Arch. Eisenh., 1963, vol. 34, 391.

20. R.C. Sharma, Ph.D. Thesis, McMaster University (1976).
21. H. Harvig: *Jernkont. Ann.*, 1971 vol. 155, 157.
22. *Metals Handbooke*, ASM, Metals Park, Ohio, 1973, vol. 8, Eight ed.
23. R.C. Sharma and J.S. Kirkaldy: *Can. Met. Quart.*, 1973, vol. 12, No. 4, p. 391.
24. C. Wagner: unpublished research quoted in *Diffusion in Solids, Liquids and Gases*, Acad. Press Inc., New York, 1962, 69.
25. G.R. Purdy, D.H. Weichert and J.S. Kirkaldy: *Trans. TMS-AIME*, 1964, vol. 230, p. 1025.
26. M. Hillert: in *Mechanism of Phase Transformations in Crystalline Solids*, Inst. of Metals, London, 1969, 231.
27. J.S. Kirkaldy and G.R. Purdy: *Can. J. Phys.*, 1962, vol. 40, p. 208.
28. L.C. Brown and J.S. Kirkaldy: *Trans. AIME*, 1964, vol. 230, p. 233.
29. A. Hultgren: *Jernkont. Ann.*, 1951, vol. 135, p. 403.
30. M. Hillert: *Jernkont. Ann.*, 1952, vol. 136, p. 25.
31. G.V. Kurdjumov in *Proceedings of the International Conference on the Peaceful Uses of Atomic Energy*, 1955, p. 15.
32. M.A. Kristhal: *Diffusion Processes in Iron Alloys*, Metallurgizdat, Moskova, 1963.
33. *CRC Handbook of Tables for Applied Engineering Science*, (eds.) R.E. Bolz and G.L. Tuve, 1975, p. 117.
34. J.E. Hilliard and J.W. Cahn: *Trans. TMS-AIME*, 1961, vol. 221, p. 344.
35. H.I. Aaranson and H.A. Domain: *Trans. AIME*, 1966, vol. 236, p. 781.
36. D.K. Bowen and C.R. Hall: *Microscopy of Materials*, Wiley, New York, 1975, p. 88.
37. *The Electron Probe Microanalyser*, McMaster University, Hamilton, Ont., Canada.
38. L.C.C. da Silva and R.F. Mehl: *Trans. AIME, J. Metals*, 1951, vol. 191, p. 155.
39. G. Krauss, Jr.: *Acta Met.*, 1963, vol. 11, p. 499.

40. J.S. Kirkaldy, P.N. Smith and R.C. Sharma: *Met. Trans.*, 1973, vol. 4, p. 624.
41. K. Nohara and K. Hirano: *Suppl. Trans. Iron Steel Inst. Japan*, 1971, vol. 11, 1267.
42. M.J. Bibby and J.G. Parr: *J.I.S.I.* Feb. 1964, 100.
43. J.E. Shelby: *J. App. Phys.*, 1977, vol. 48, 3387.
44. D.W. Gomersall and J.G. Parr: *J.I.S.I.*, Mar. 1965, 275.
45. M. Jzumiyama, M. Tsuchiya and Y. Jmai: *J. Japan Inst. Metals*, 1970, vol. 34, 291.
46. J.D. Bolton and E.R. Petty: *Met. Sc. J.*, 1971, vol. 5, 166.
47. M.M. Shteynberg, D.A. Mirzayev and T.N. Ponomareva: *Fiz. metal. metalloved.*, 1977, vol. 43, No. 1, 166.
48. O.P. Morozov, D.A. Mirzayev and M.M. Shteynberg: *Fiz. metal. metalloved.*, 1972, vol. 34, No. 4, 795.
49. D.A. Mirzayev, O.P. Morozov and M.M. Shteynberg: *Fiz. metal. metalloved.*, vol. 36, No. 3, 560.
50. W.D. Swanson and J.G. Parr: *J.I.S.I.*, Feb. 1964, 104.
51. T.B. Massalski, J.H. Perepezko and J. Jacklovsky: *Mater. Sci. Eng.*, 1975, vol. 18, 193.
52. T.B. Massalski, S.K. Bhattacharyya and J.G. Perepezko: *Met. Trans. A*, 1978, vol. 9A, 53.
53. T.B. Massalski, in *Phase Transformations*, ASM, Metals Park, Ohio, 1970, 433.
54. T.B. Massalski: *Mater. Sci. Eng.*, 1976, vol. 25, 119.
55. A.B. Greninger: *Trans. Met. Soc. AIME*, 1939, vol. 133, 204.
56. T.B. Massalski: *Acta Met.*, 1958, vol. 6, 243.
57. J.D. Ayers and D.C. Joy: *Acta Met.*, 1972, vol. 20, 1371.
58. M.R. Plichta, J.H. Perepezko, H.I. Aaronson and W.F. Lang III: *Acta Met.*, 1980, vol. 28, 1031.
59. M.R. Plichta and H.I. Aaronson: *Acta Met.*, 1980, vol. 28, 1041.

60. T.B. Massalski, A.J. Perkins and J. Jaklovsky: *Met. Trans.*, 1972, vol. 3, 687.
61. J.D. Ayers and T.B. Massalski: *Met. Trans.*, 1971, vol. 3, 261.
62. M. Hillert: in *Lectures on Phase Transformations*, AIME, New York, 1975, 1.
63. K. Lücke and K. Detert: *Acta Met.*, 1957, vol. 5, 628.
64. J.W. Cahn: *Acta Met.*, 1962, vol. 10, 789.
65. K. Lücke and H. Stüwe: *Acta Met.*, 1971, vol. 19, 1087.
66. A. Roy and C.L. Bauer: *Acta Met.*, 1975, vol. 23, 957.
67. M. Hillert and B. Sundman: *Acta Met.*, 1976, vol. 24, 731.
68. J.S. Kirkaldy and R.C. Sharma: *Acta Met.*, 1980, vol. 28, 1009.
69. C.L. Magee: in *Phase Transformations*, ASM, Metals Park, Ohio, 1968, 115.
70. W.S. Owen, F.J. Schoen and G.R. Srinivasan: in *Phase Transformations*, ASM, Metals Park, Ohio, 1968, 157.
71. G. Krauss: in *Hardenability concepts with Applications to Steel*, Met. Soc. AIME, 1978, 229.
72. G. Krauss and A.R. Marder: *Met. Trans.*, 1971, vol. 2, 2343.
73. J.W. Christian: in *Decomposition of Austenite by Diffusional Processes*, Interscience Publishers, New York, 1962, 371.
74. M.J. Roberts: *Met. Trans.*, 1970, vol. 1, 3287.
75. M.J. Roberts and W.S. Owen: *Trans. Quart. ASM*, 1967, vol. 60, 687.
76. *Metals Handbook*, ASM, Metals Park Ohio, 1961, vol. 1, 245.
77. J.D. Boyd: *Met. Trans.*, 1976, vol. 7A, 1577.
78. J.D. Boyd: *Met. Trans.*, 1976, vol. 7A, 1604.
79. D.A. Karlyn, J.W. Cahn and M. Cohen: *Trans. TMS-AIME*, 1969, vol. 245, 197.
80. J.D. Ayers and T.B. Massalski: *Met. Trans.*, 1972, vol. 3, 3185.
81. L. Kaufman, S.V. Radcliffe and M. Cohen: in *Decomposition of Austenite by Diffusional Processes*, Interscience Publishers, New York, 1962, 313.

TABLE I
 Free Energy of Transformation of Pure Iron from Ferrite to Austenite
 in cal./mole.

| Temp. (°K) | $\Delta^0 G^{\alpha \rightarrow \gamma}$ | Temp. (°K) | $\Delta^0 G^{\alpha \rightarrow \gamma}$ |
|------------|--|------------|--|
| 1184 | 0 | 1020 | 64.16 |
| 1180 | 0.74 | 1010 | 72.18 |
| 1170 | 2.52 | 1000 | 80.80 |
| 1160 | 4.48 | 980 | 89.8 |
| 1150 | 6.66 | 970 | 99.3 |
| 1140 | 9.10 | 960 | 109.3 |
| 1130 | 11.84 | 950 | 119.9 |
| 1120 | 14.92 | 940 | 131.0 |
| 1110 | 18.37 | 930 | 142.4 |
| 1100 | 22.22 | 920 | 154.1 |
| 1090 | 26.07 | 910 | 166.0 |
| 1080 | 29.92 | 900 | 178.3 |
| 1070 | 34.21 | 890 | 191.1 |
| 1060 | 39.11 | 880 | 204.1 |
| 1050 | 44.31 | 870 | 217.3 |
| 1040 | 50.15 | 860 | 230.8 |
| 1030 | 56.75 | 850 | 244.7 |

Table II
Analyses of the Ferrovac-E Iron and Electrolytic Manganese Flakes Used
for the Preparation of Fe-Mn Alloys

| Ferrovac-E Iron | | Electrolytic Manganese | |
|-----------------|---------|------------------------|---------|
| C | 40 ppm | Mg | 40 ppm |
| Mn | 10 ppm | Fe | 5 ppm |
| S | 60 ppm | Si | 2 ppm |
| P | 20 ppm | Cu | <2 ppm |
| Si | 60 ppm | Mn | Balance |
| N | 4 ppm | | |
| Fe | Balance | | |

TABLE III

Summary of the Experimental Results Obtained from the Equilibration of the Various Diffusion Couples

(A) For Equilibration at 762°C

| Diffusion Couple | Results Obtained | | Others |
|----------------------------|----------------------------------|--------------------------|--|
| | End Compositions of the Tie-Line | | |
| | $X^\alpha = 1.98$ at.%Mn | $X^\gamma = 4.62$ at.%Mn | |
| Fe-6.2%Mn/Fe | //// | //// | (1) $D^{\alpha, Mn} = 2.7 \times 10^{-12}$ cm ² /sec (2) Volume fraction of austenite in equilibrium with ferrite, $V_f = 18.9\%$, with standard deviation, $\sigma = 0.72\%$ |
| Fe-6.2%Mn/Fe-4.0%Mn | //// | /// | |
| Fe/Fe-2.47%Mn | | ✓ | |
| Surface depleted Fe-6.2%Mn | //// | //// | |

TABLE III (Cont'd.)

(B) For Equilibration at 822°C

| Diffusion Couple | End Compositions of the Tie-Line | | Results Obtained | Others |
|------------------|--|-------------------------------------|-------------------|--------|
| | $X^\alpha = 1.35 \text{ at. \% Mn}$ | $X^\gamma = 2.44 \text{ at. \% Mn}$ | | |
| | Fe-3.1 %Mn/Fe Fe/Fe-2%Mn Fe-3.1 %Mn/Fe-2.47%Mn | //// //// | //// //// / | |

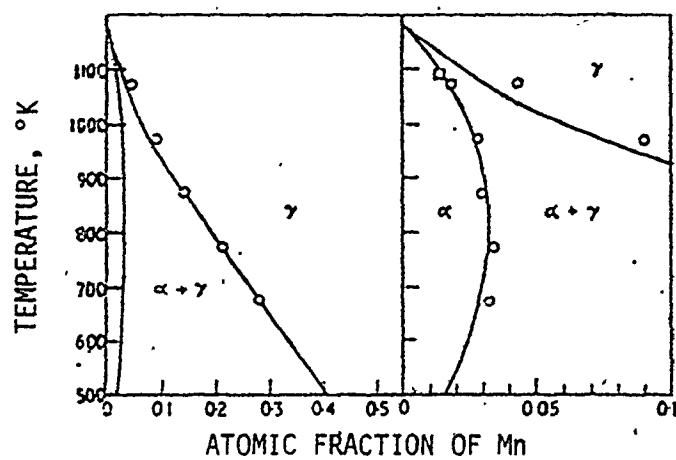


Figure (1) Phase diagram for the iron-rich Fe-Mn system (after Hillert et. al.(2)), (O) Troiano et. al.(1), (□) Hillert et. al.(2).

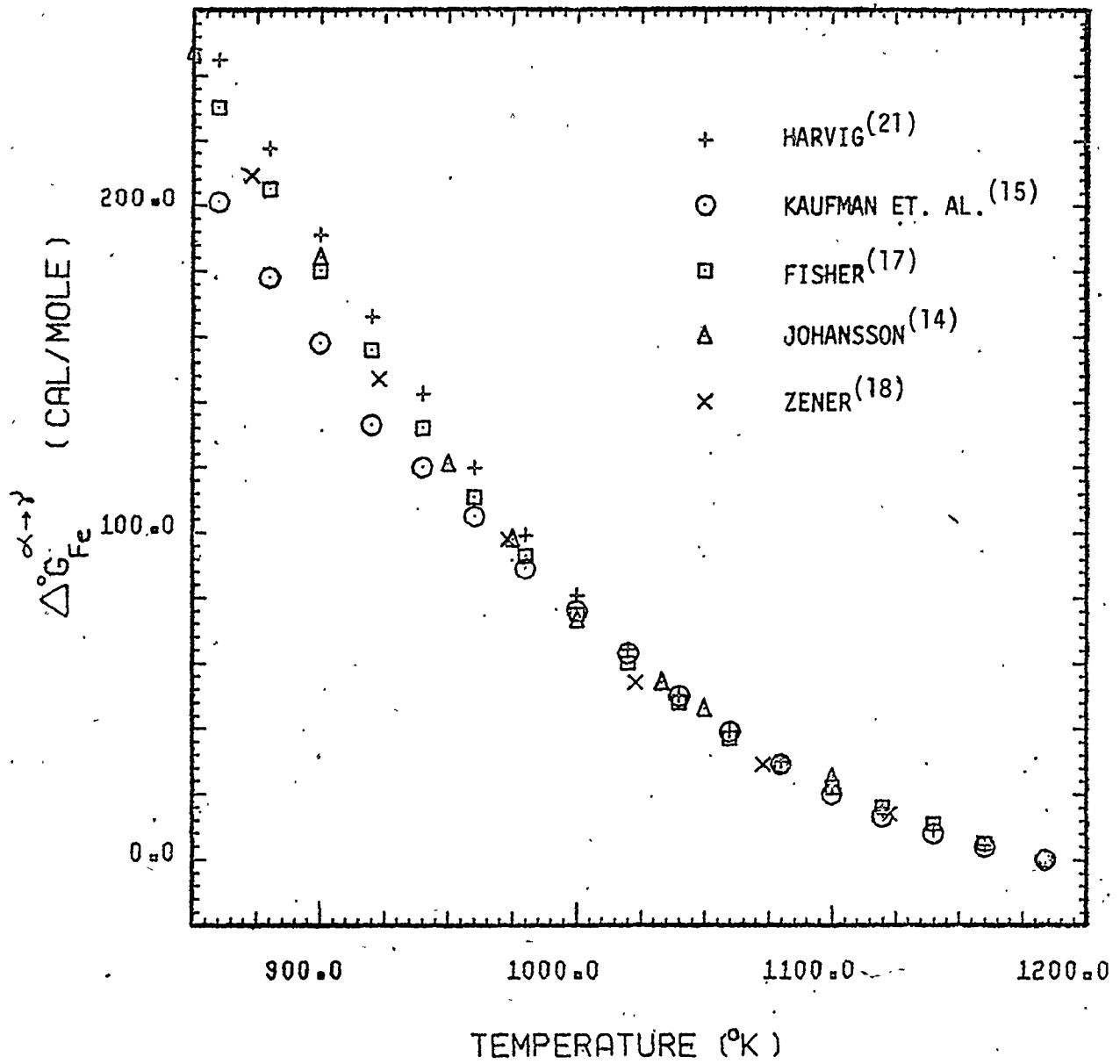
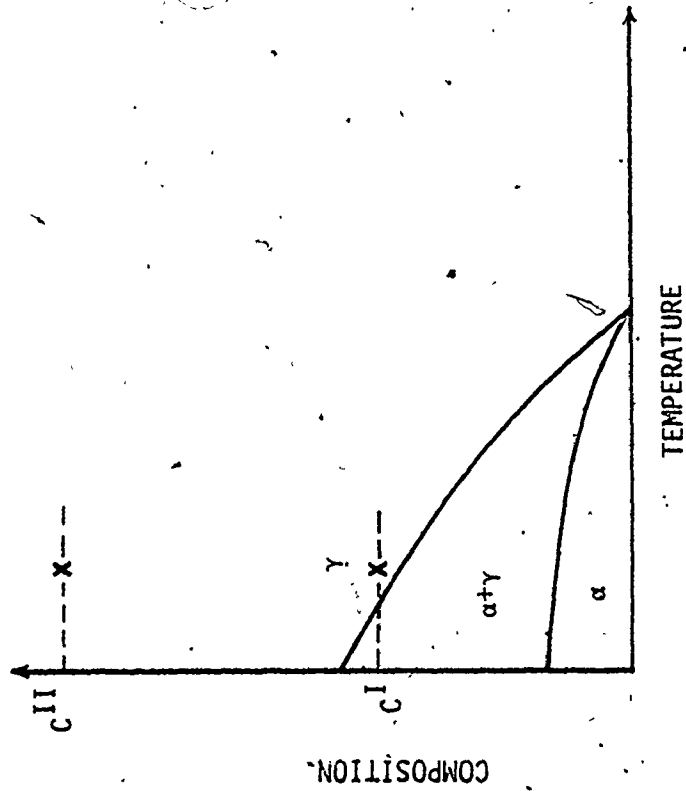
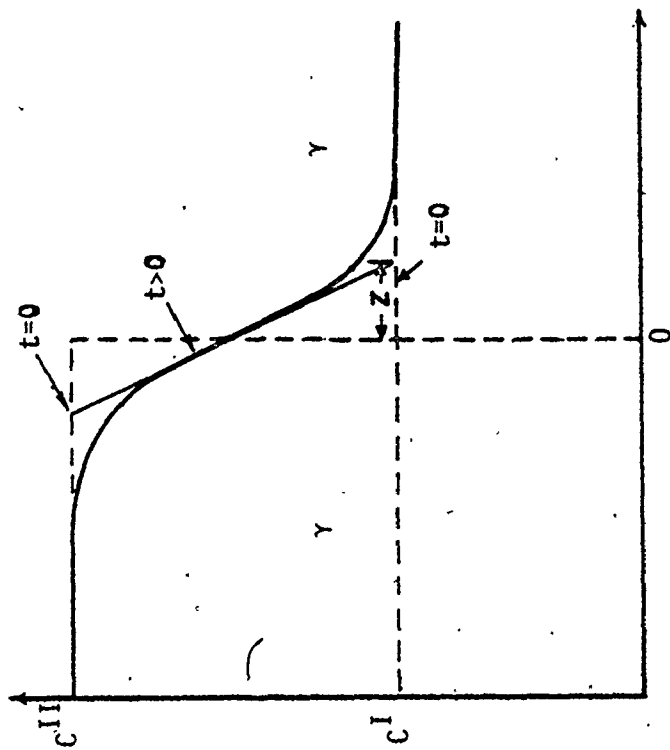


Figure (2) Free energy of transformation of pure iron from ferrite to austenite in cal./mole.



(a)



(b)

Figure (3) a. Schematic phase diagram showing α/γ equilibrium and the location of the composition limits of the one phase diffusion couple (x). b. Composition profiles at $t=0$ and $t>0$.

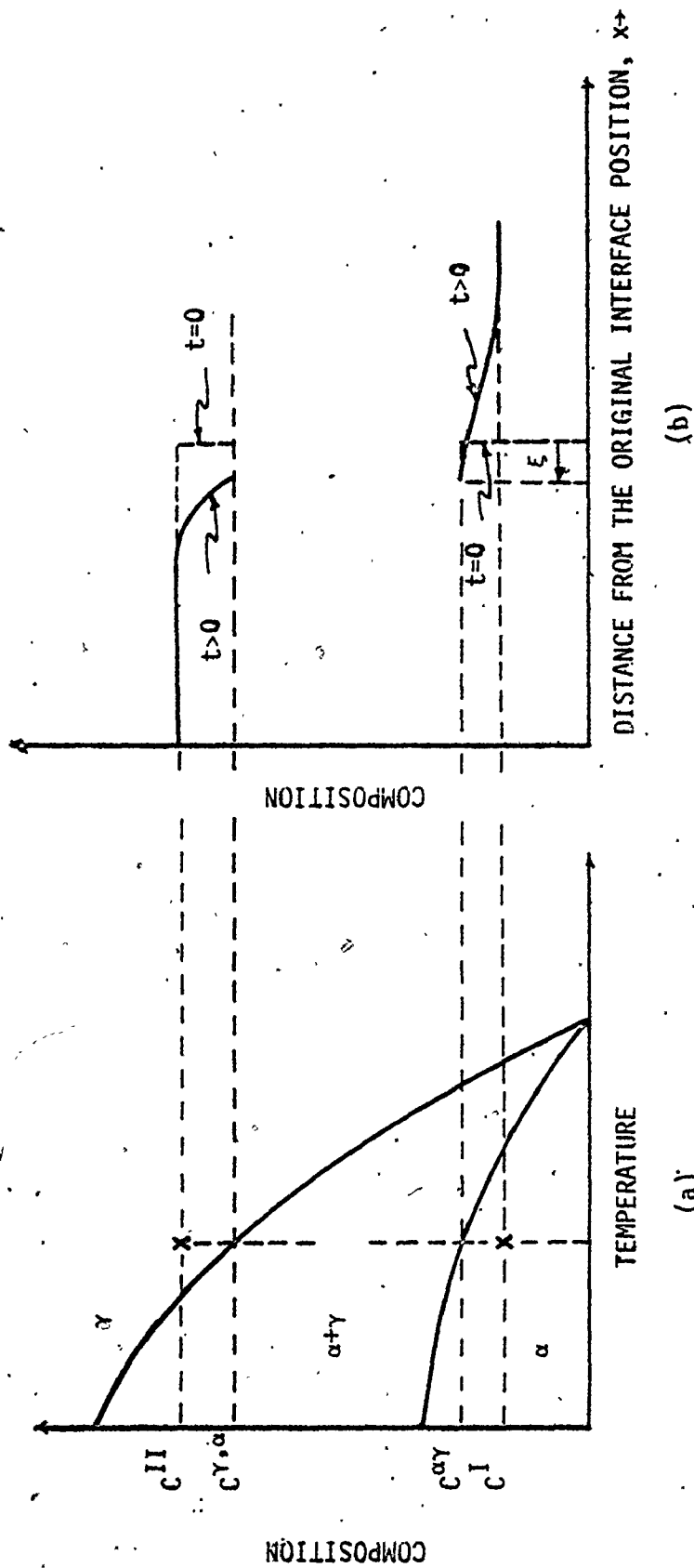


Figure (4) a. Schematic phase diagram showing α/γ equilibrium and the composition limits of the diffusion couple (x), b. Schematic composition profiles in the γ and α phases.

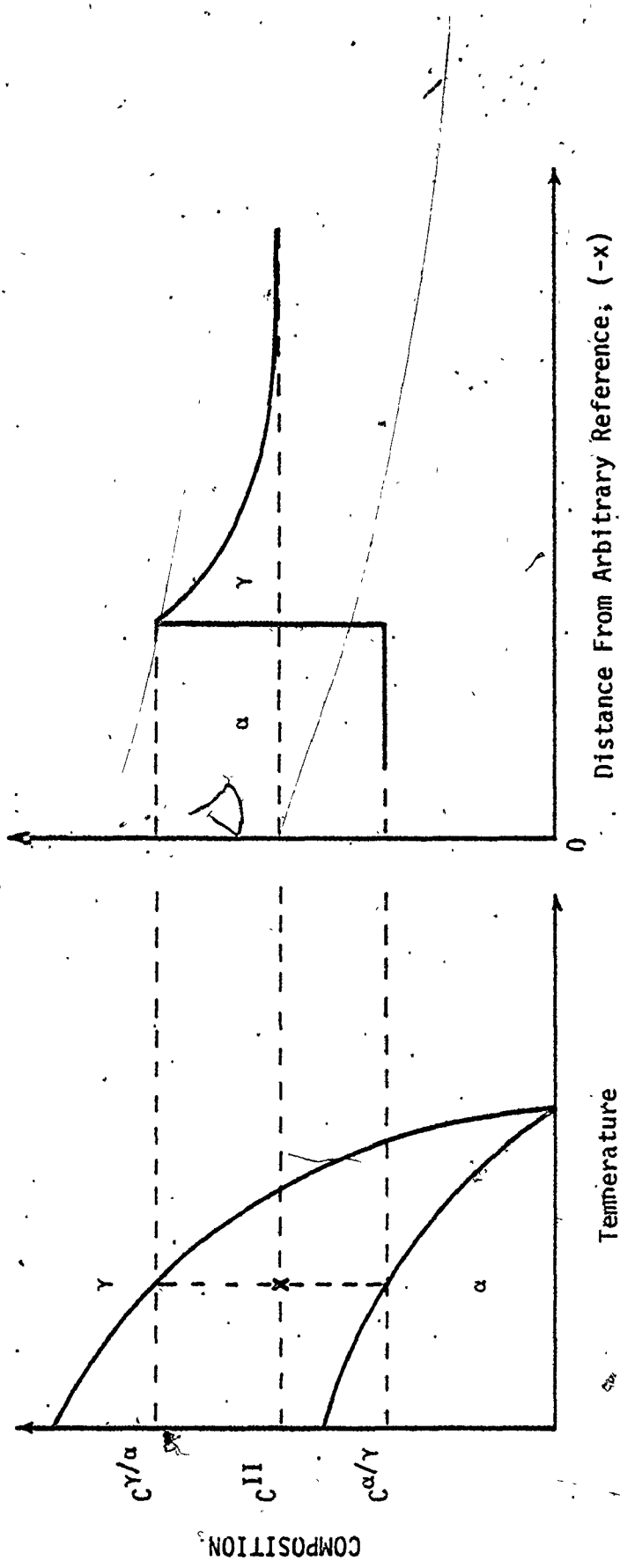


Figure (5) a. Schematic phase diagram showing α/γ equilibrium and the original composition of the alloy (x), b. the composition profile in α and γ phases, following the precipitation of α .

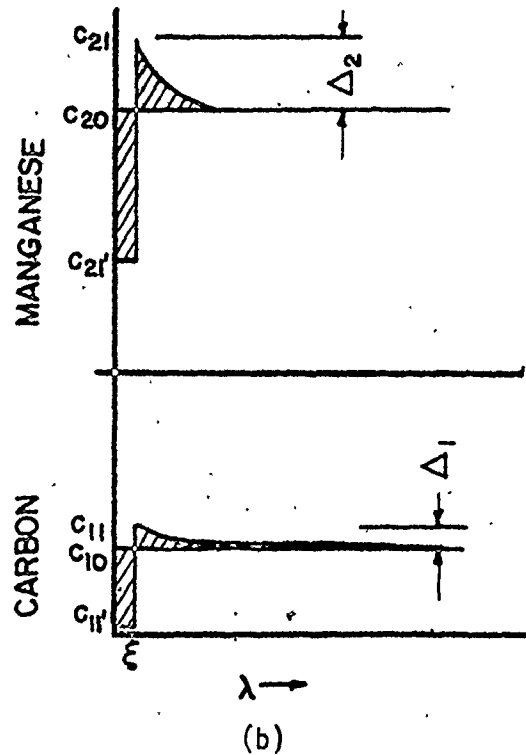
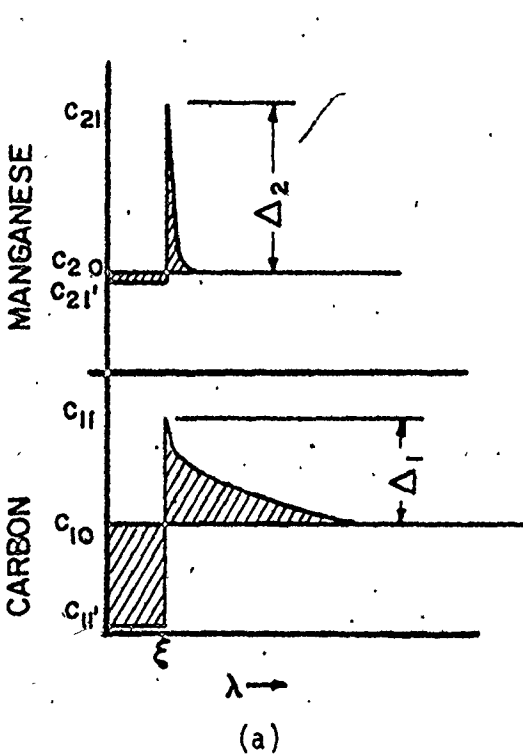
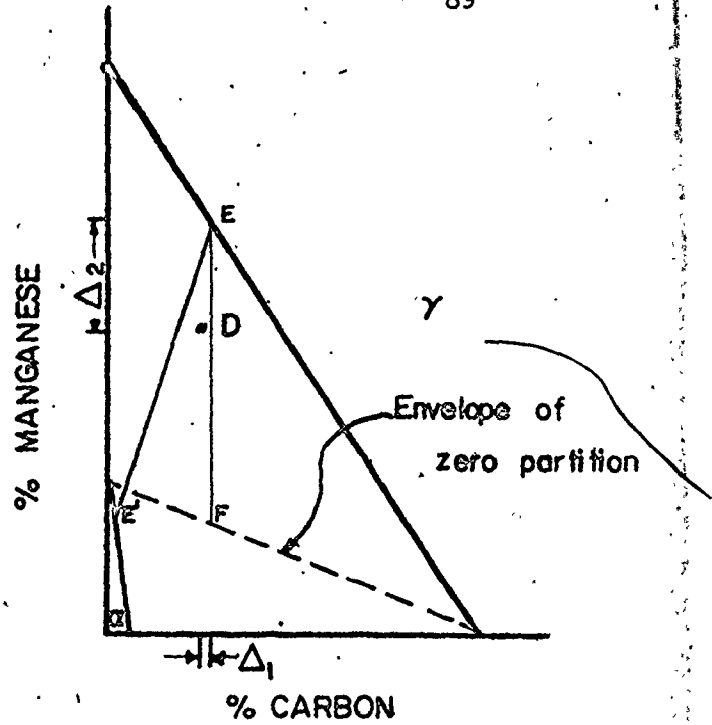
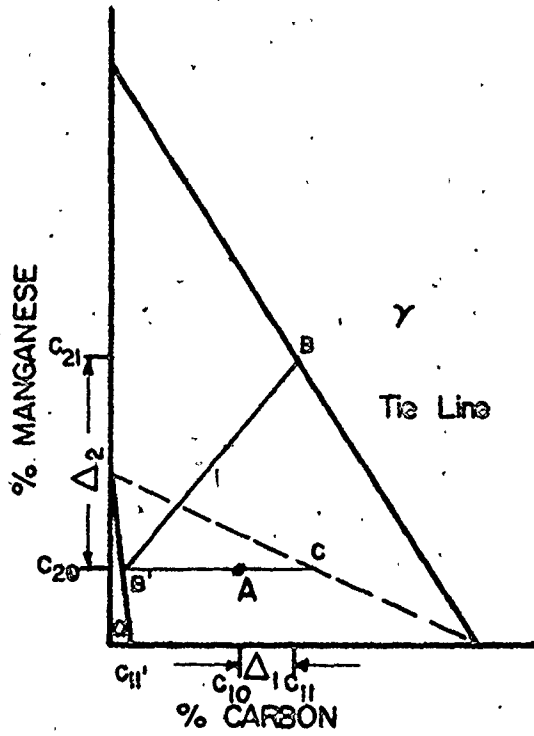


Figure (6) a, b Schematic penetration curves in $\lambda (=x/\sqrt{t})$ space for ferrite growth in Fe-C-Mn austenites. The mass balances are represented by equal shaded areas on either side of the interface ($\lambda=\xi$) (after Purdy, Weichert and Kirkaldy (25)).

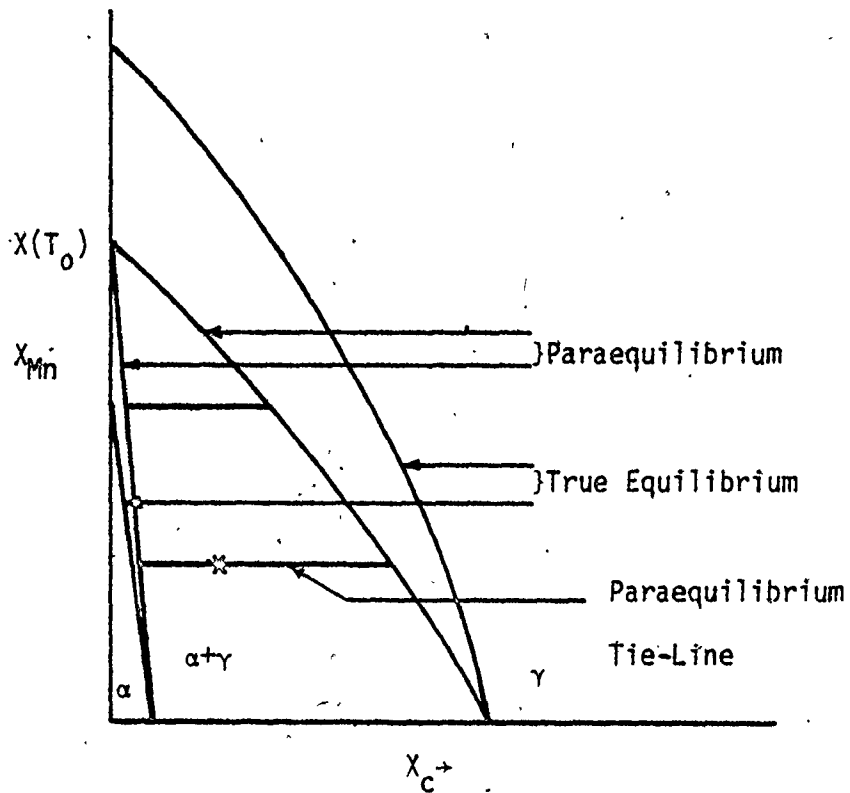


Figure (7) Schematic phase diagram showing true equilibrium and para-equilibrium phase boundaries with paraequilibrium tie-lines parallel to C axis.

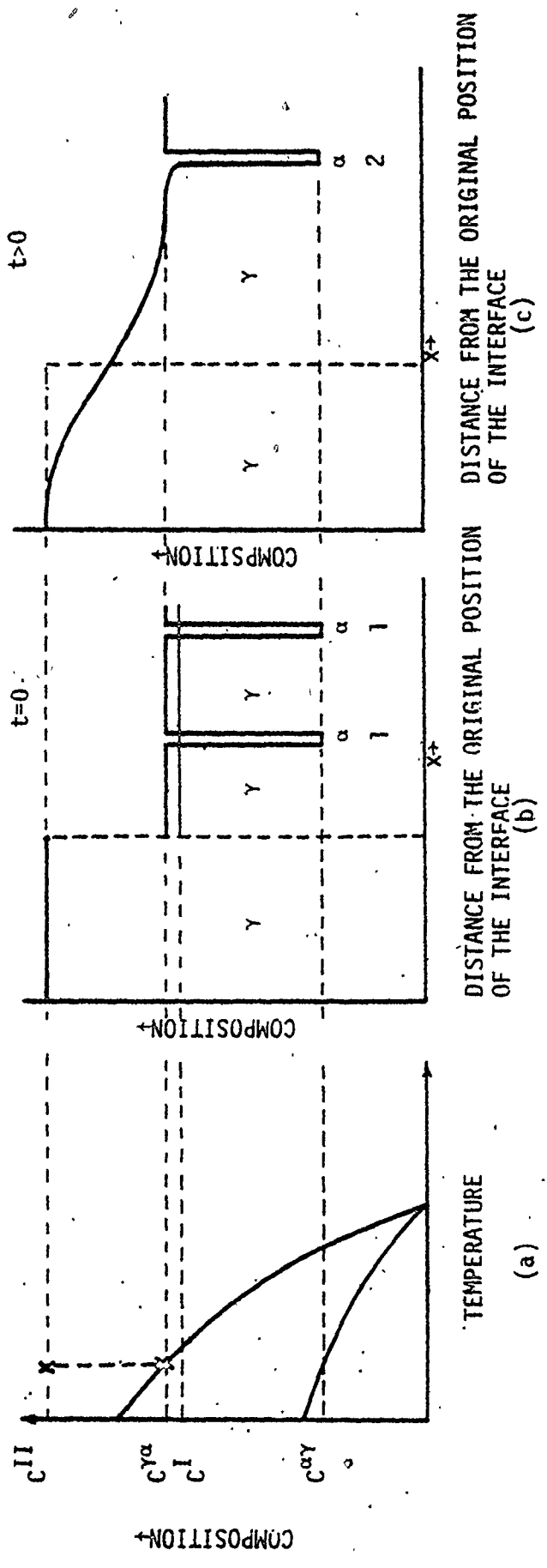


Figure (8) a. Schematic phase diagram showing α/γ equilibrium and the location of the composition limits of the diffusion couple, b. Schematic composition profile for the diffusion couple having a negligibly small fraction of α at $t=0$, and c, at $t>0$.

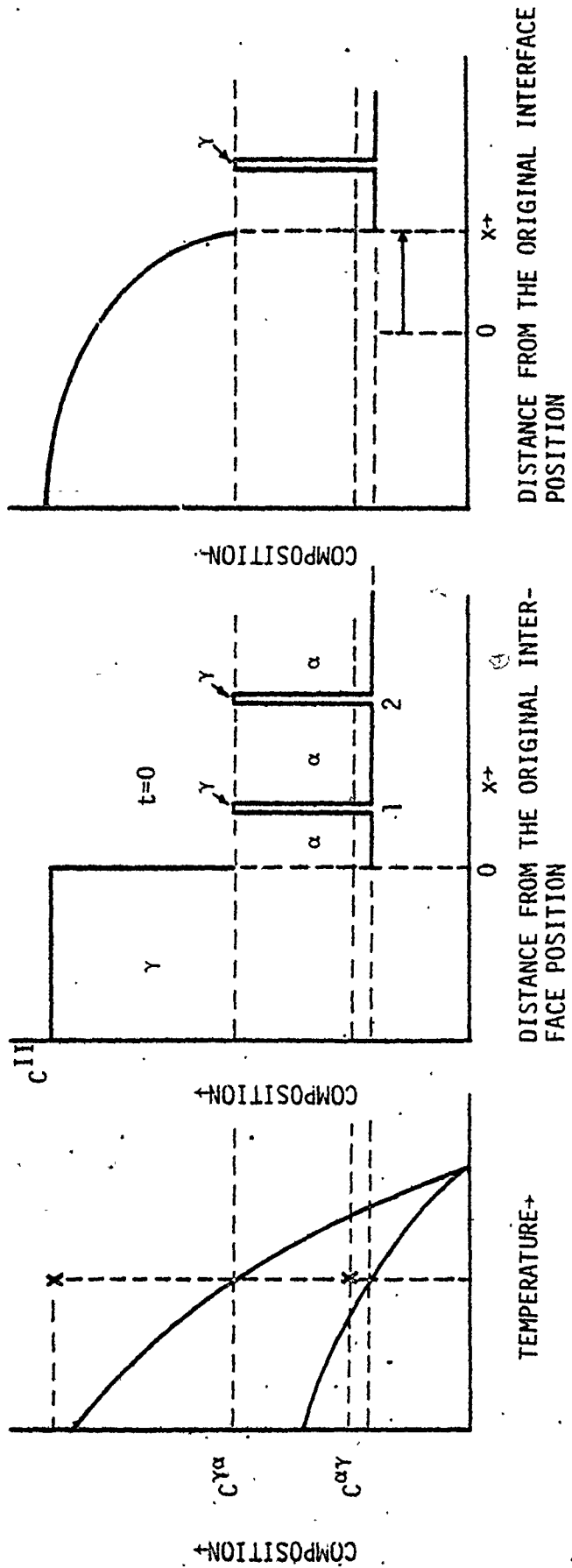


Figure (9) a. Schematic phase diagram showing α/γ equilibrium and the composition limits of the diffusion couple (x), b. composition profile at $t=0$ and c. at >0 .

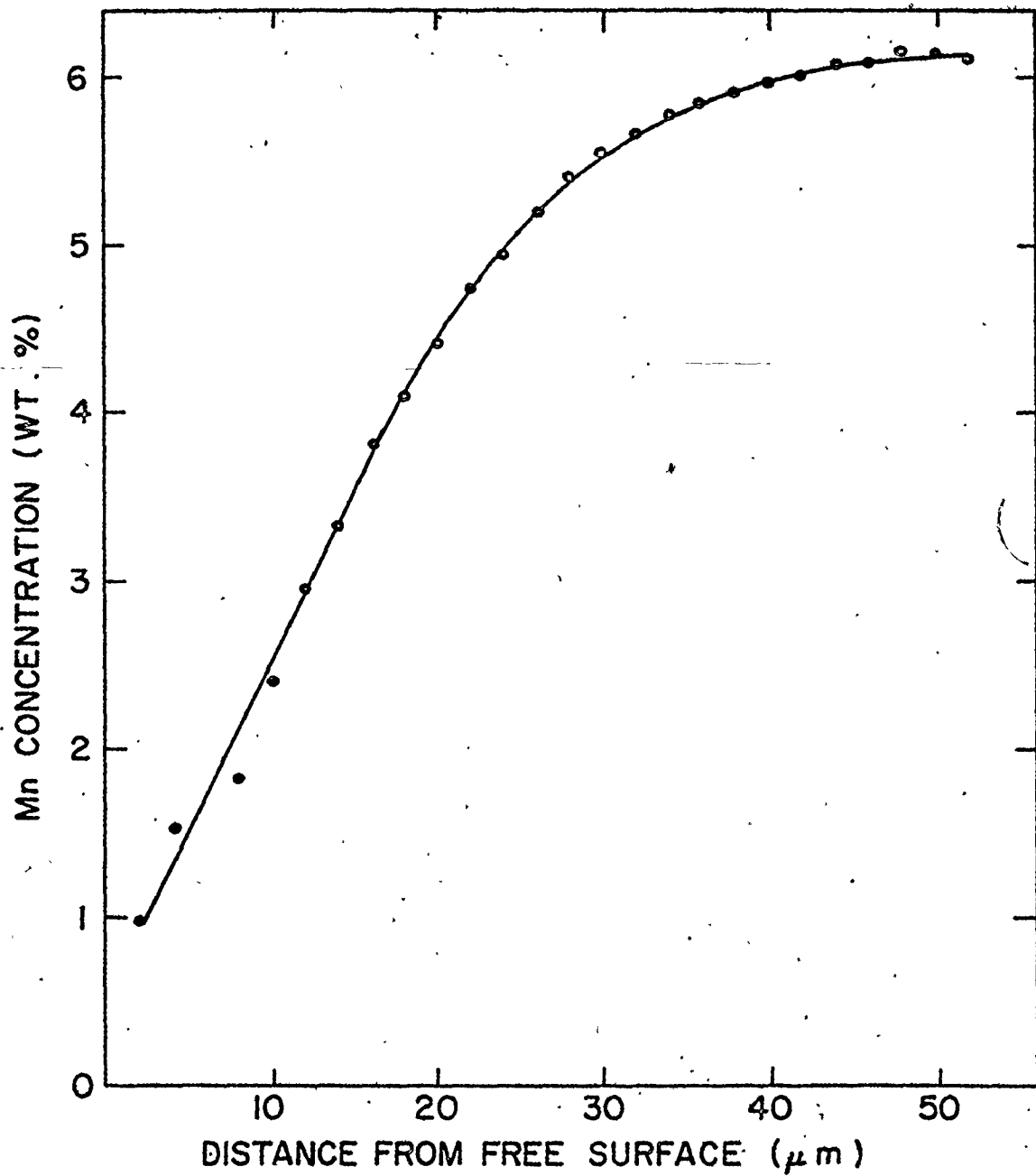


Figure (10) Diffusion profile generated in Fe-6.2% Mn alloy on heating in vacuum sealed cansule at 1100°C for 24 hours.

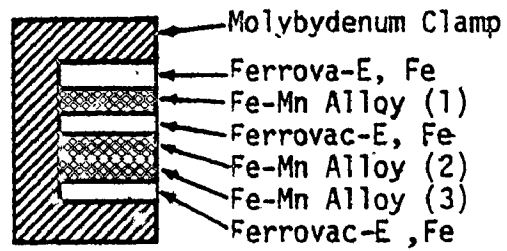


Figure (11) Schematic diagram showing arrangement of Ferrovac-E, Fe and Fe-Mn alloys, as held in a molybdenum clamp (approximately full size).

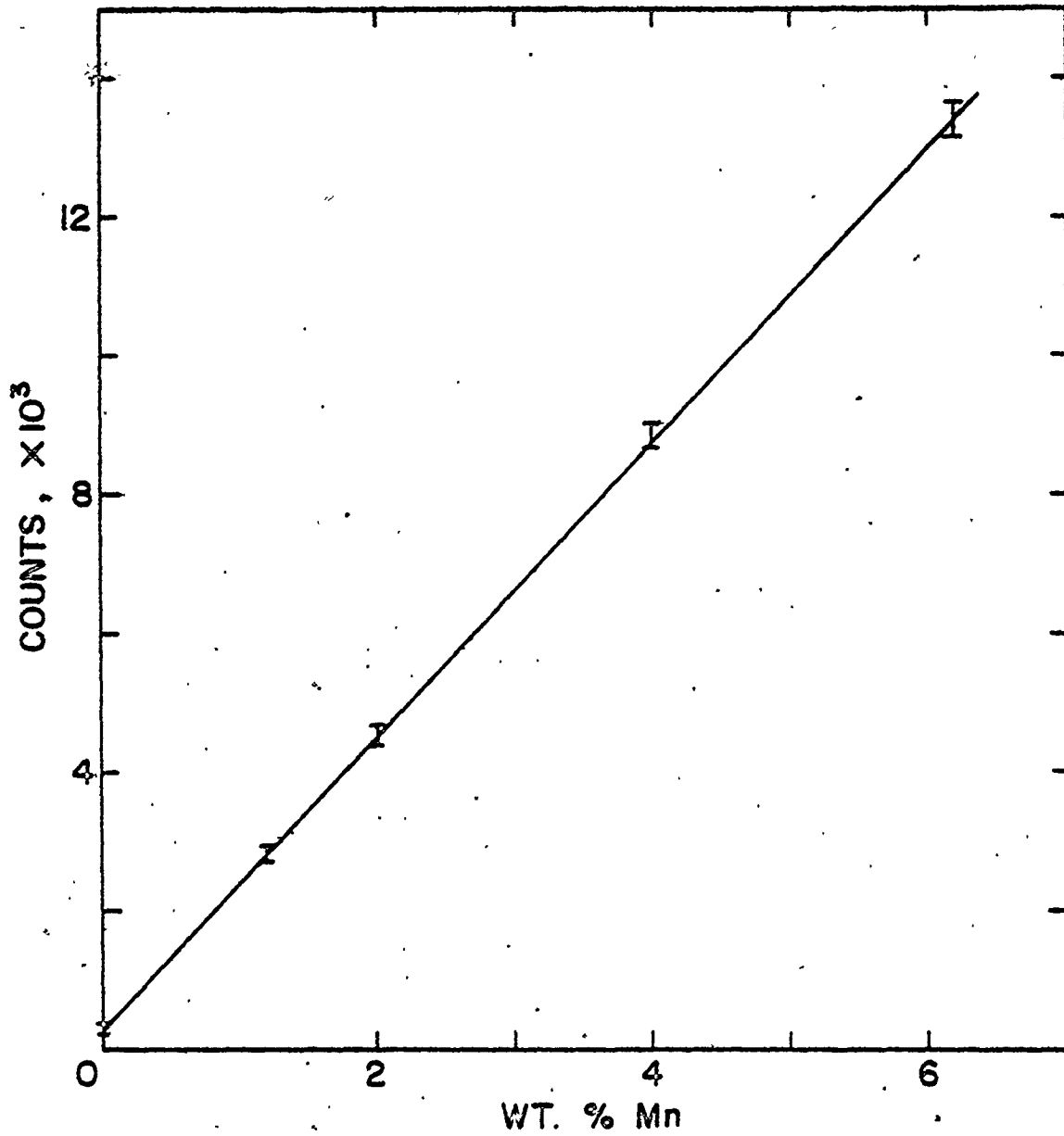
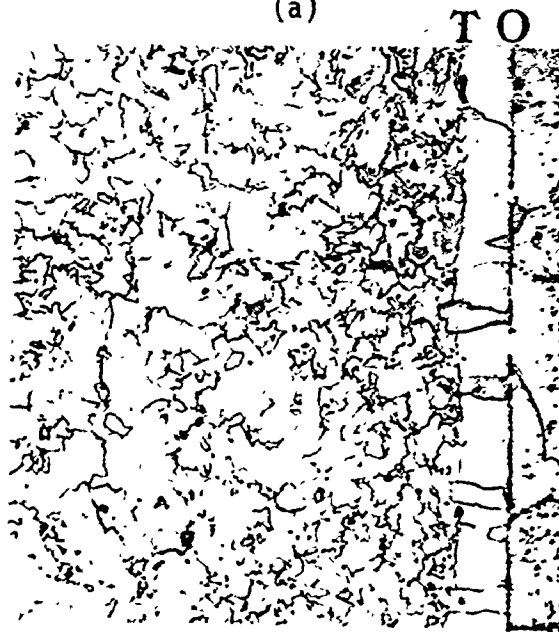


Figure (12) Typical calibration curve for electron microprobe analysis.



(a)



(b)

Figure (13) (a) Optical micrographs of Fe-6.2%Mn/Fe diffusion couple equilibrated at 762°C for 6 weeks (x125) and (b) Fe-3.1%Mn/Fe diffusion couple equilibrated at 822°C for 6 weeks (x125). 00 and TT are the positions of γ/α interface at $t=0$ and $t=t$, respectively.

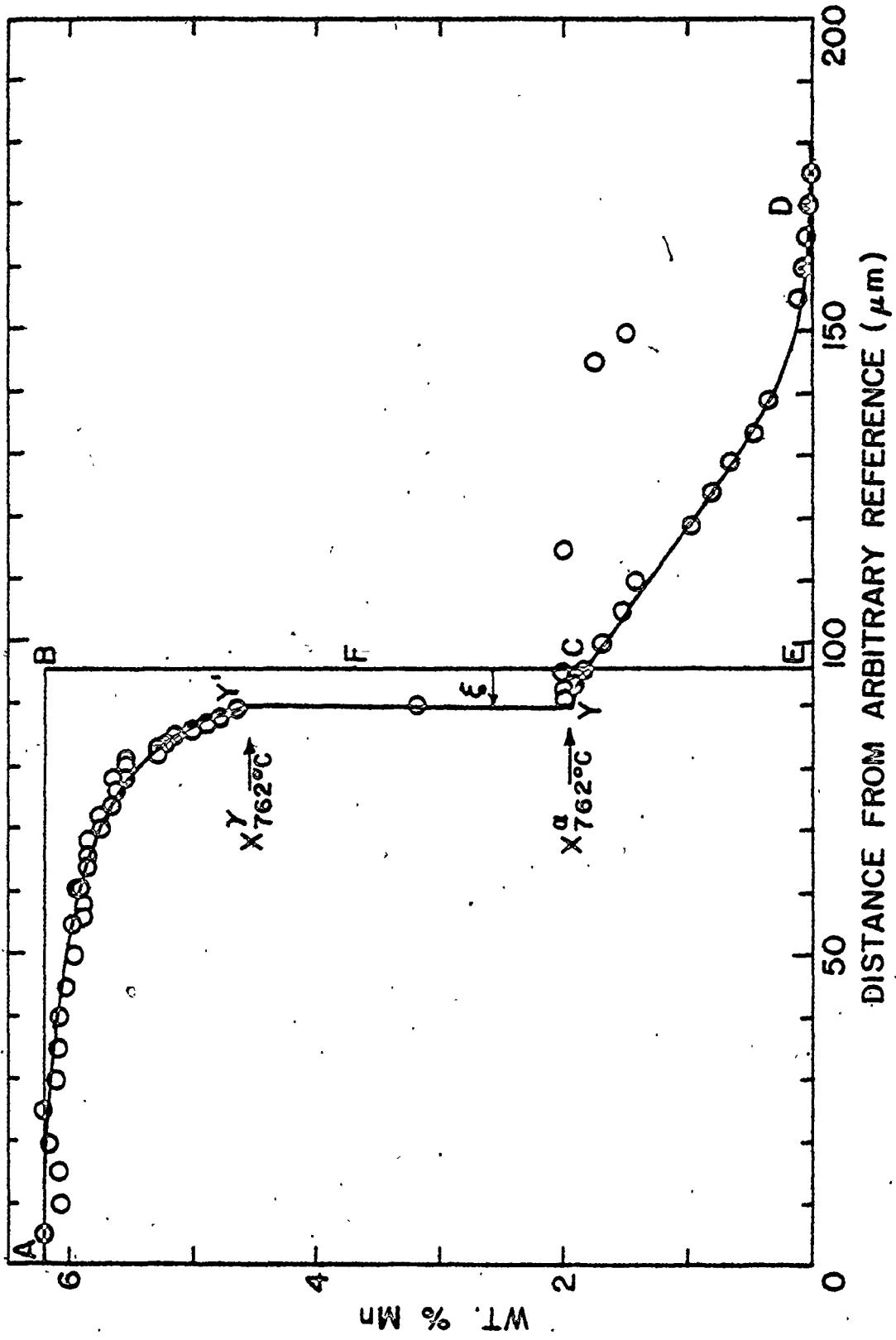


Figure (14a) Complete composition profile in Fe-6.2%Mn/Fe couple equilibrated at 762°C for 6 weeks, taken across the γ/α interface. There are a few MnO precipitates on the right.

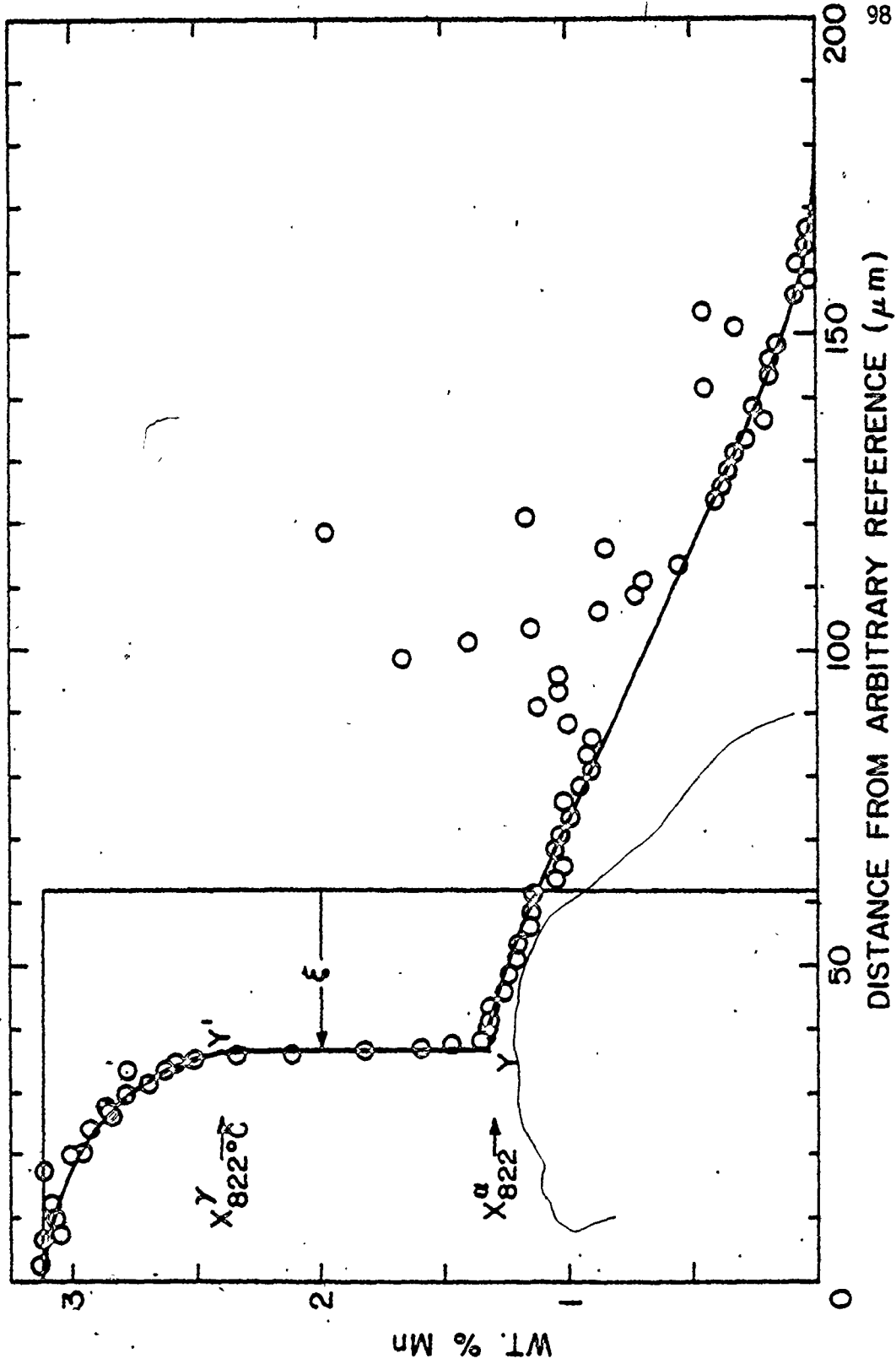


Figure (14b) Complete composition profile across γ/α interface in the Fe-3.1%Mn/Fe diffusion couple equilibrated at 822°C for 6 weeks. Note the precipitates of MnO which have been detected with Ferrovac side.

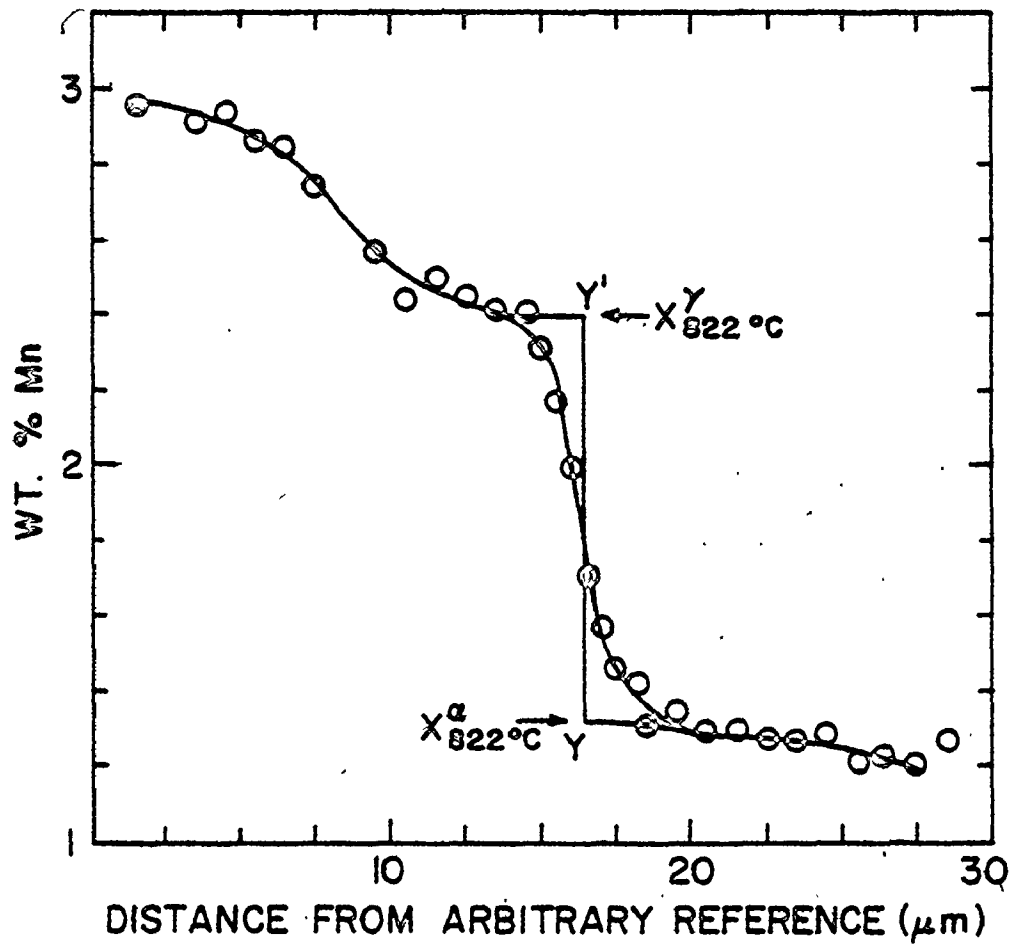
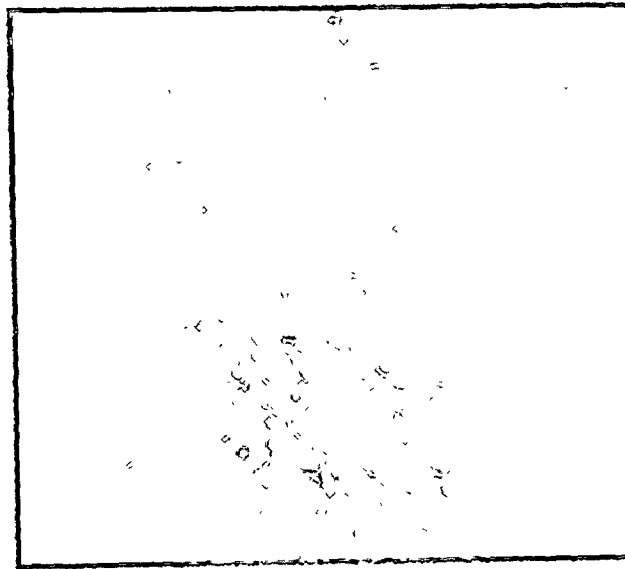
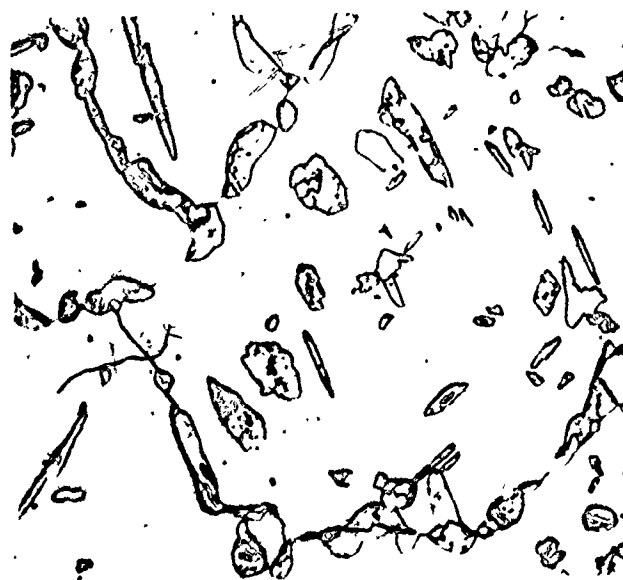


Figure (14c) Expanded partial composition profile in the Fe-3.1%Mn/Fe diffusion couple equilibrated at 822°C for 6 weeks. Note the loss of resolution at the interface due to the approximately 2 μm diameter x-ray source.



(a)



(b)

Figure (15) (a) Optical micrograph of Fe/Fe-2.4%Mn diffusion couple equilibrated at 762°C for 6 weeks, x125, and (b) that at higher magnification of the far right region of the same sample as in (a), x250.

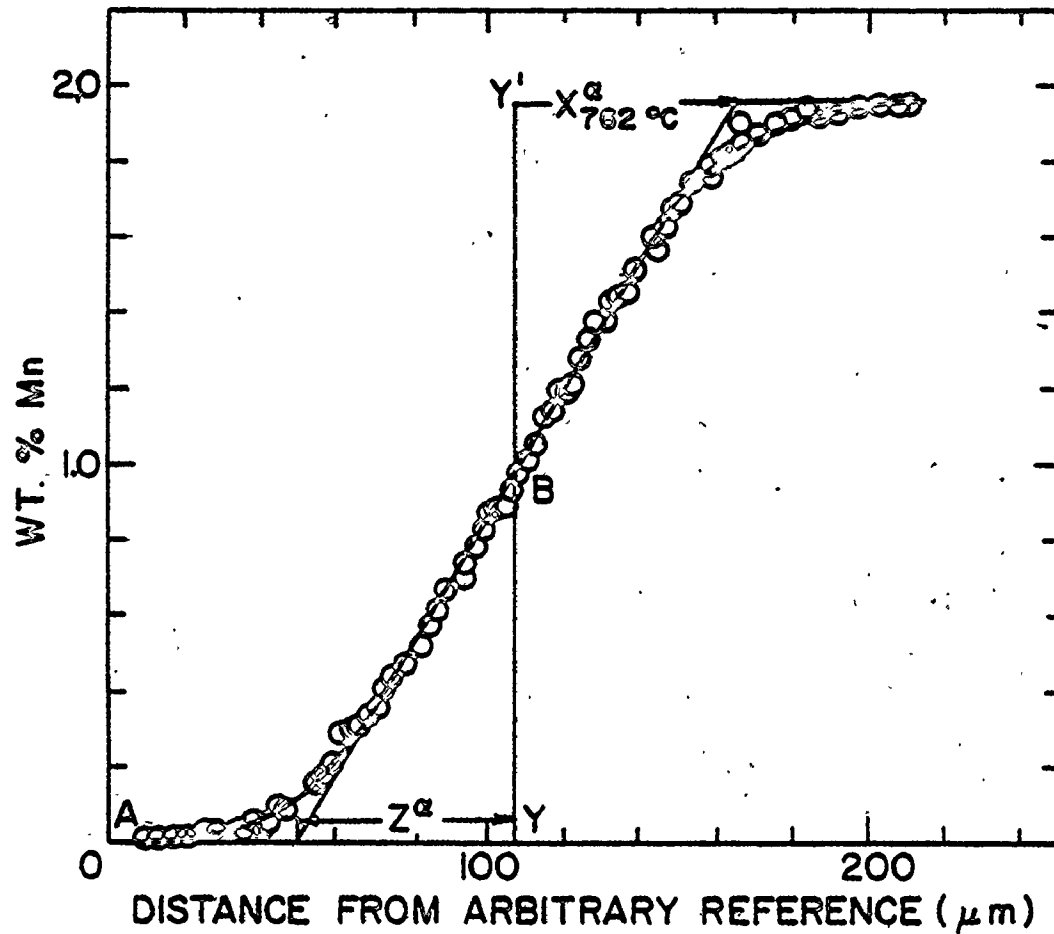


Figure. (16a) Composition profile in the single phase ferrite region of Fe/Fe-2.4%Mn couple equilibrated at 762°C for 6 weeks.

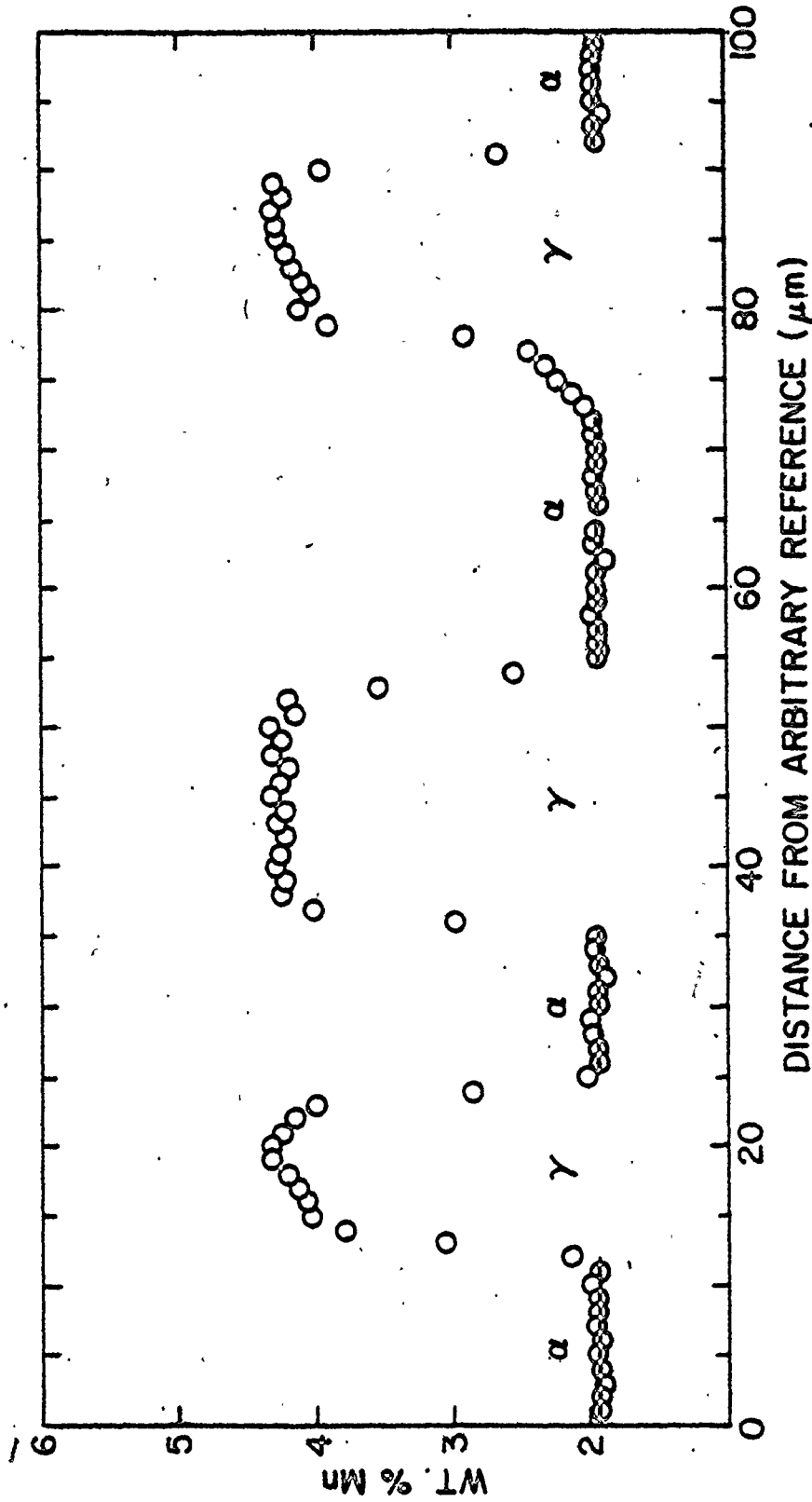


Figure (16b) Typical composition profiles across α/γ interfaces in Fe/Fe-2.4%Mn couple equilibrated at 762°C for 6 weeks.



(a)



(b)

Figure (17) (a) Optical micrograph of Fe/Fe-4%Mn, x250 and (b) that of Fe-6.2%Mn/Fe-4%Mn diffusion couples equilibrated at 762°C for 6 weeks, x250.

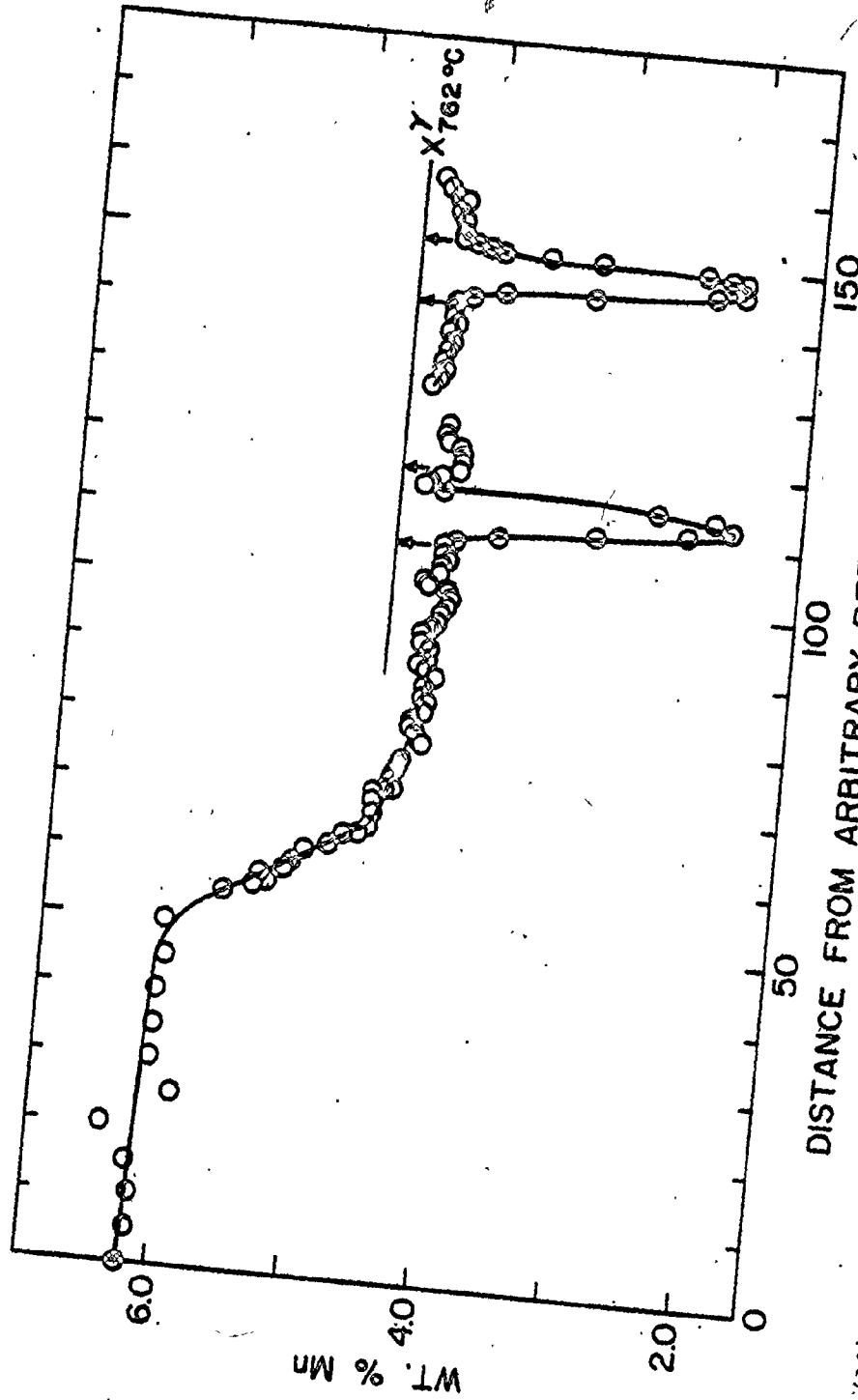
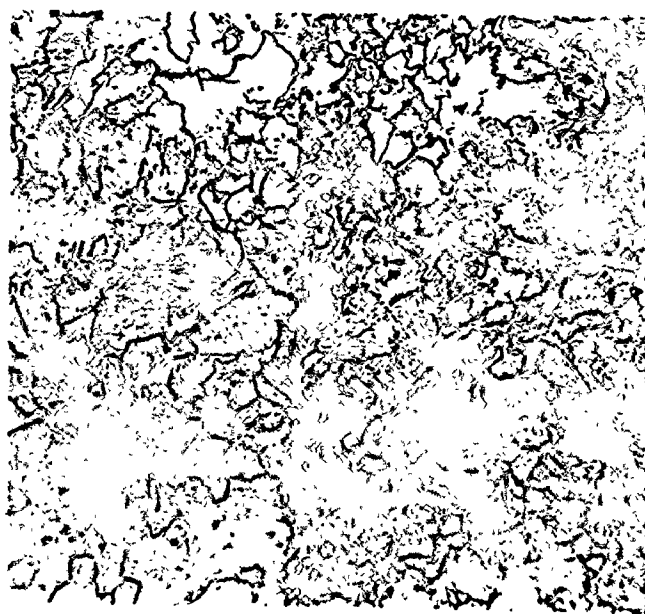


Figure (18) Typical composition profile in Fe-6.2%Mn/Fe-4%Mn couple equilibrated at 762°C for 6 weeks.



(a)



(b)

Figure (19) (a) Optical micrograph of Fe/Fe-2%Mn x 125, and (b) that of Fe-2.47%Mn/Fe-3.1%Mn diffusion couples equilibrated at 822°C, x125.

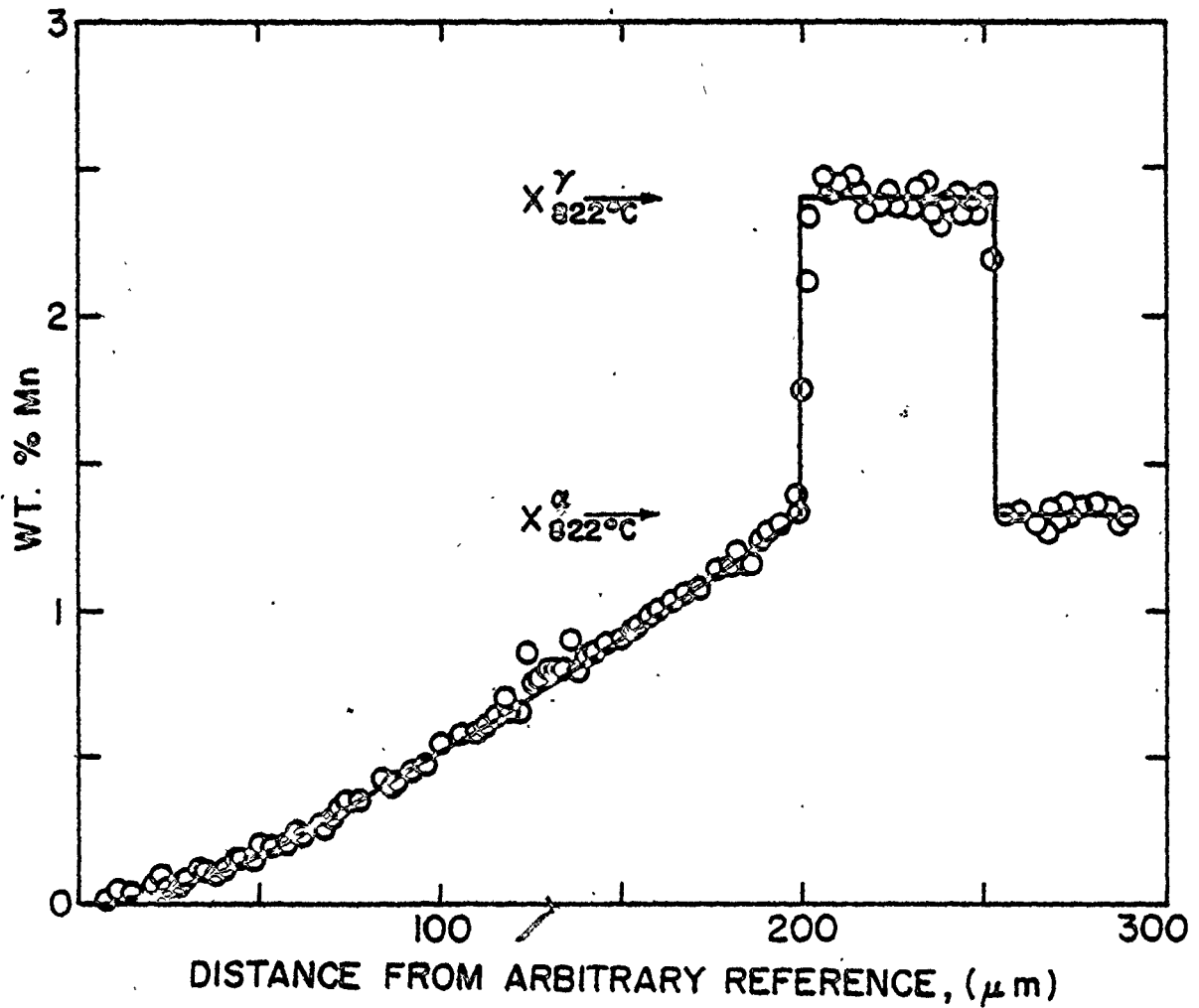


Figure (20a) Typical composition profile in Fe/Fe-2%Mn diffusion couple equilibrated at 822°C for 6 weeks.

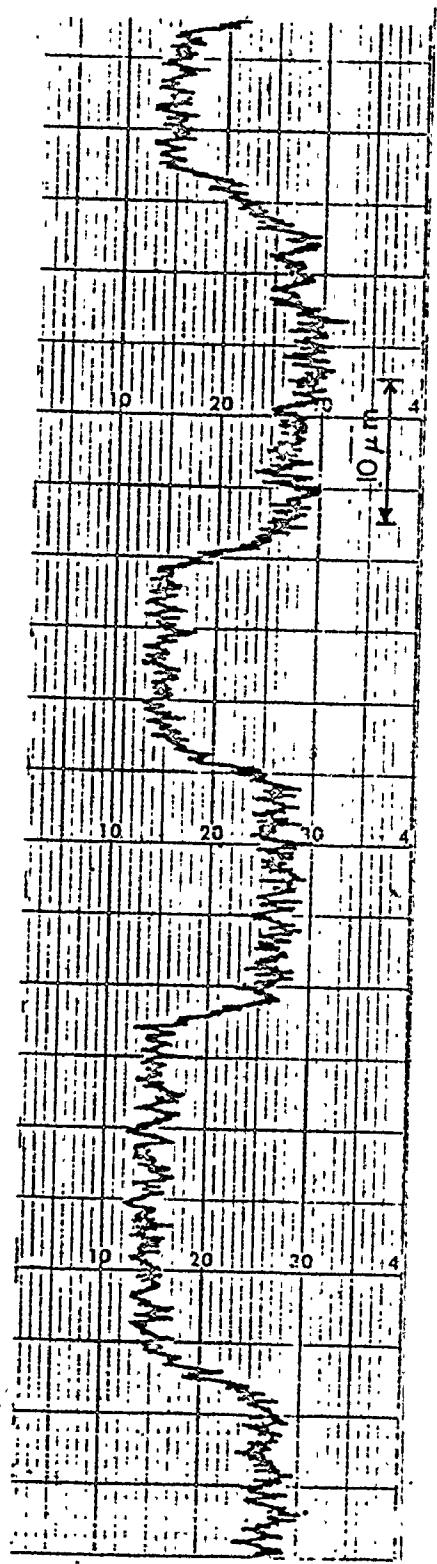


Figure (20b) Typical microprobe trace across $\alpha/\gamma/\alpha$ regions of Fe/Fe-2%Mn diffusion couple equilibrated at 822°C for 6 weeks.

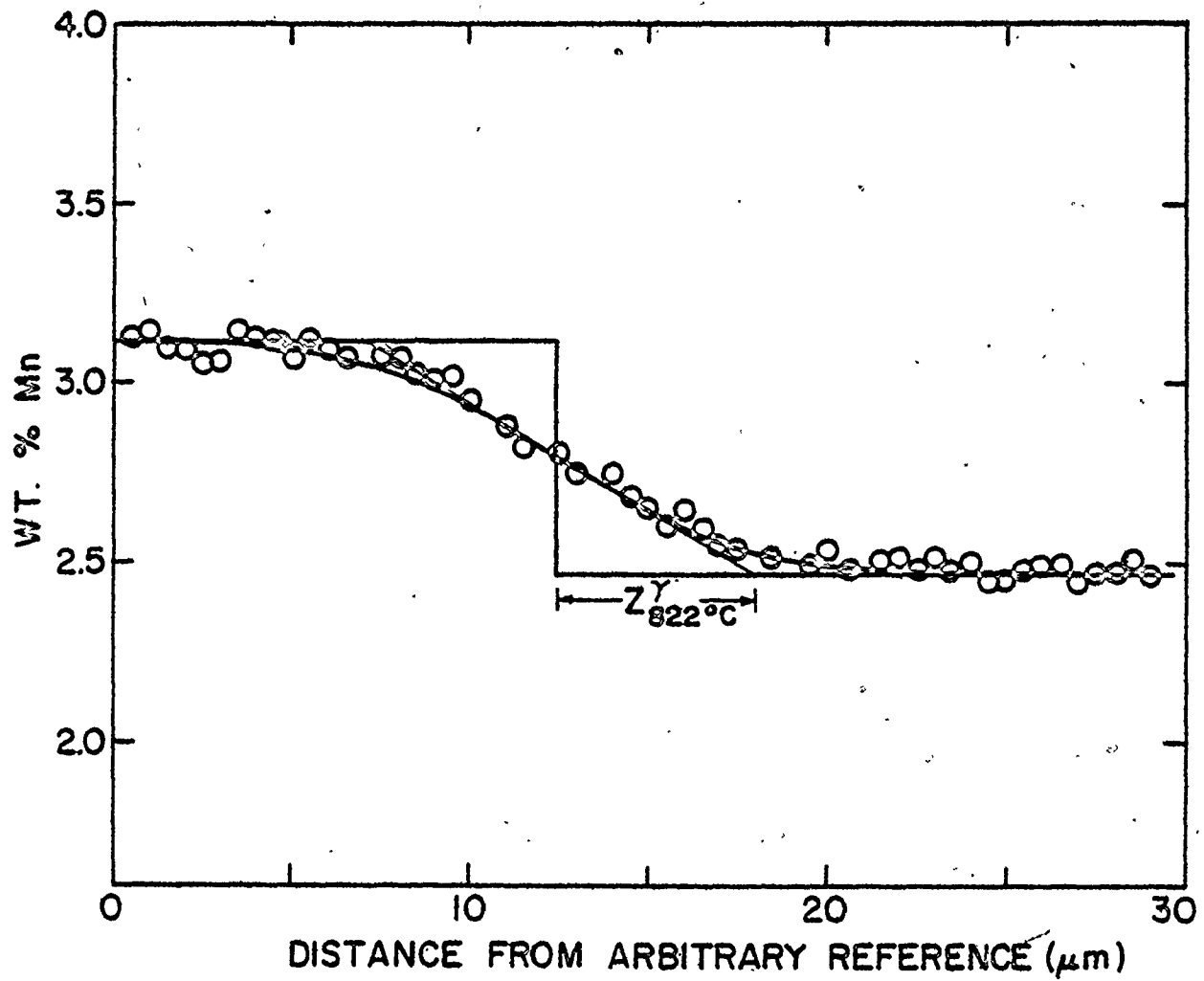
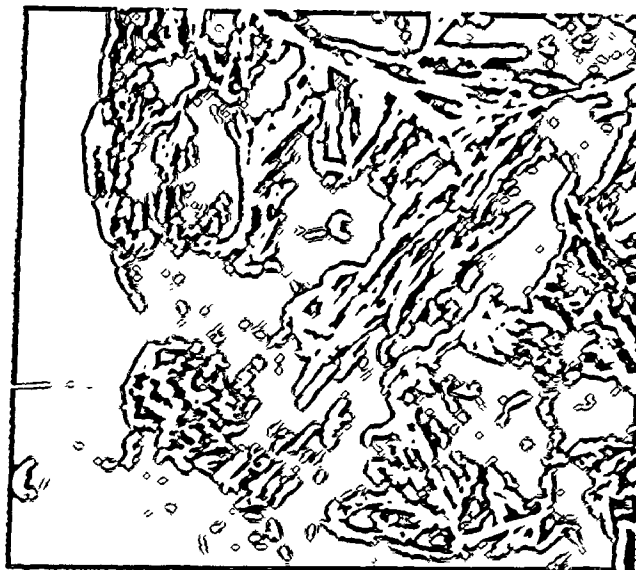
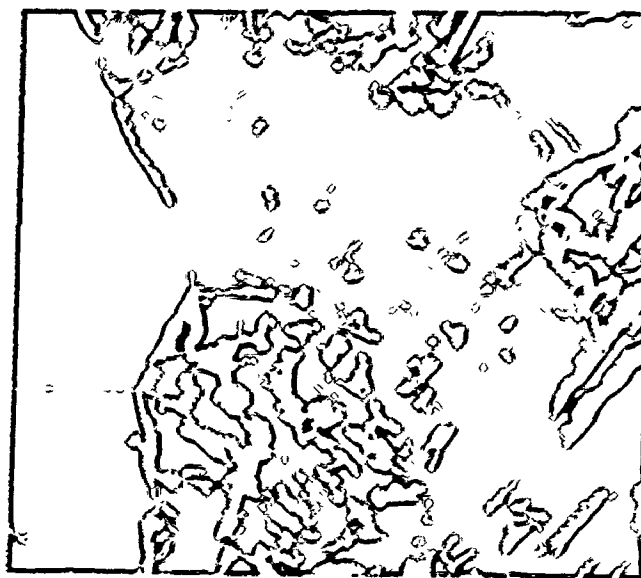


Figure (21) Composition profile in single phase austenite; Fe-3.1 %Mn/
Fe-2.47%Mn equilibrated at 822°C for 6 weeks.



(a)



(b)

Figure (22) (a) Scanning electron micrographs of Fe-6.2% Mn sample austenitized at 1100°C for 120 hr and followed by annealing at 762°C for 6 weeks, x1800, and (b) at higher magnification, x4500.

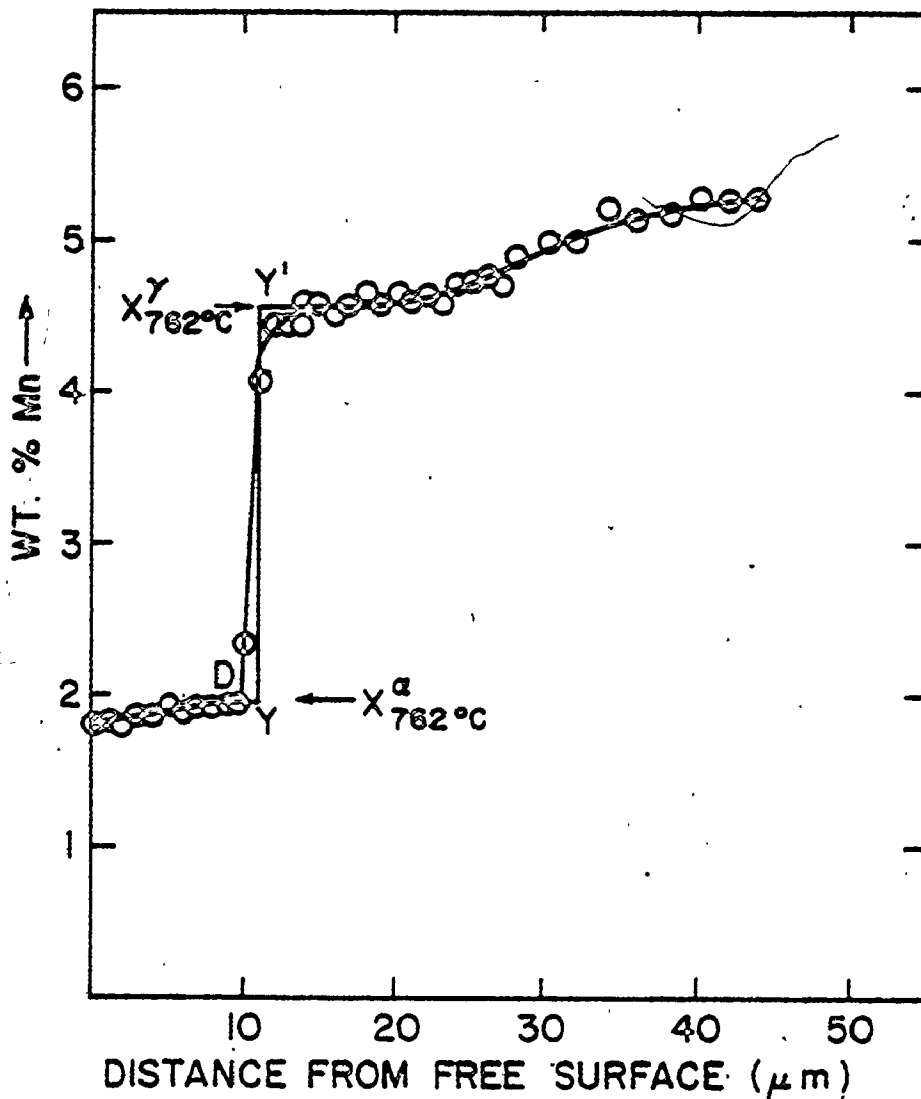


Figure (23) Typical composition profile of the Fe-6.2%Mn alloy austenitized at 1100°C for 120 hrs. and followed by annealing at 762°C for 6 weeks.

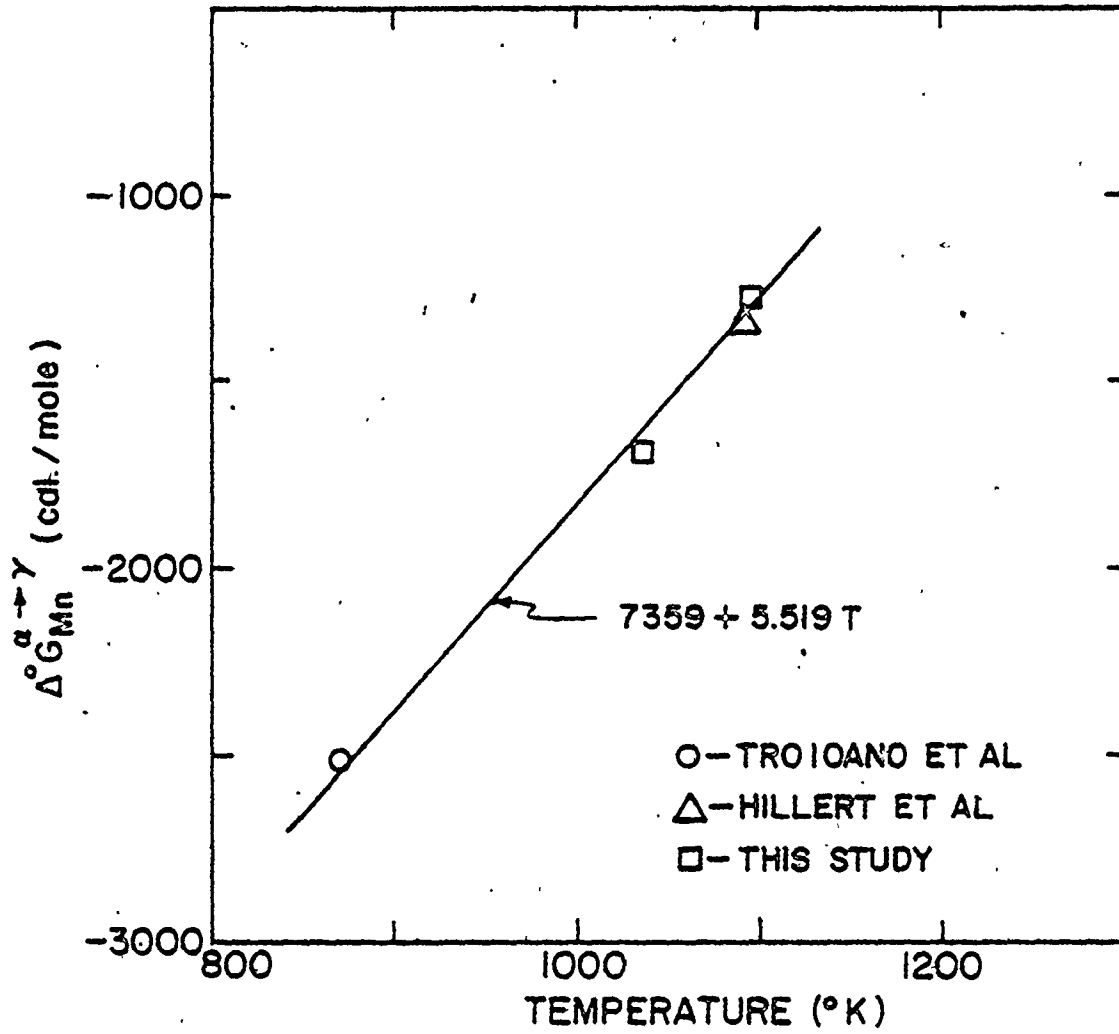


Figure (24) $\Delta^0 G_{Mn}^{\alpha \rightarrow \gamma}$ as a function of temperature.

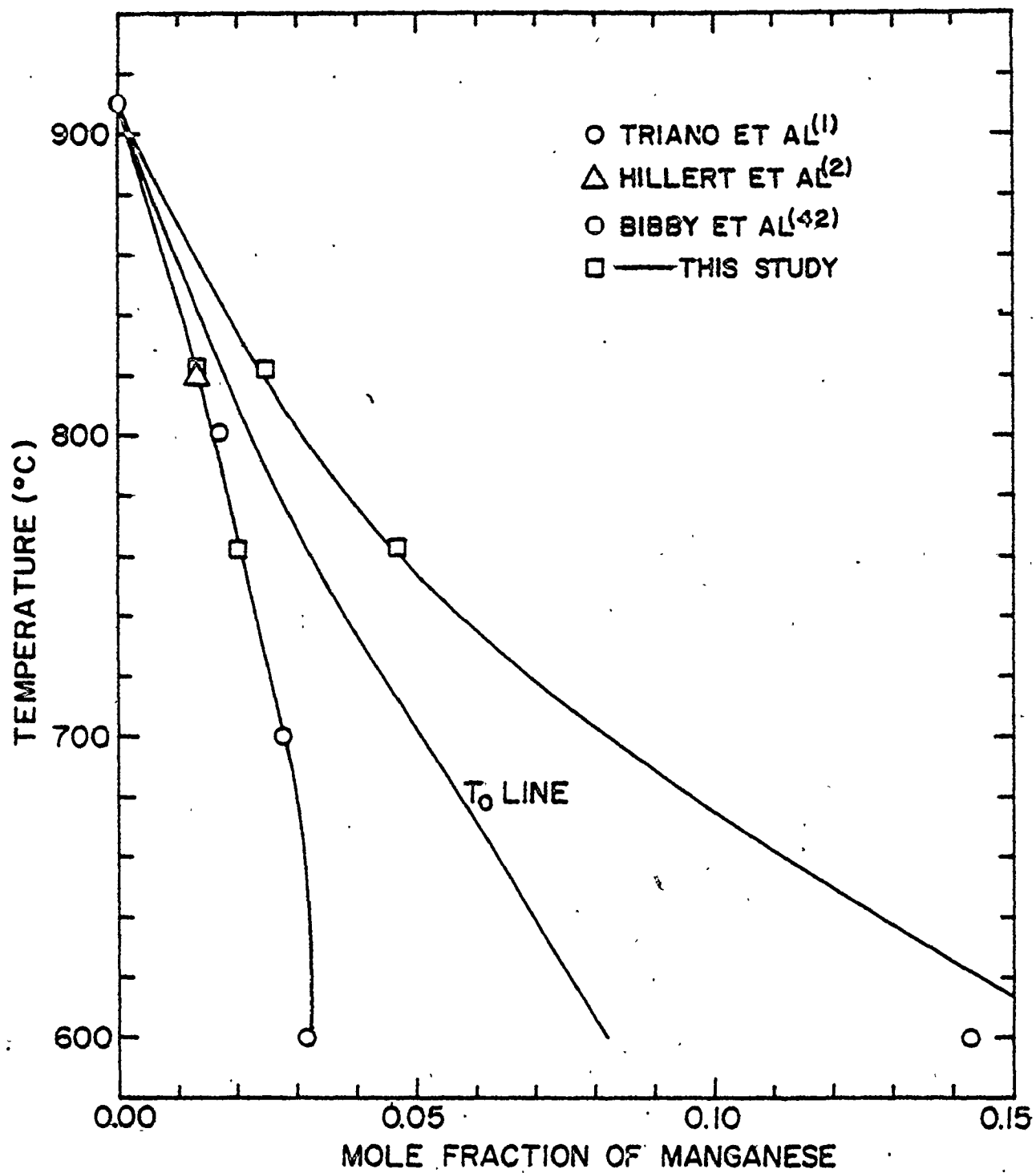


Figure (25) Phase diagram of the iron-rich Fe-Mn system.

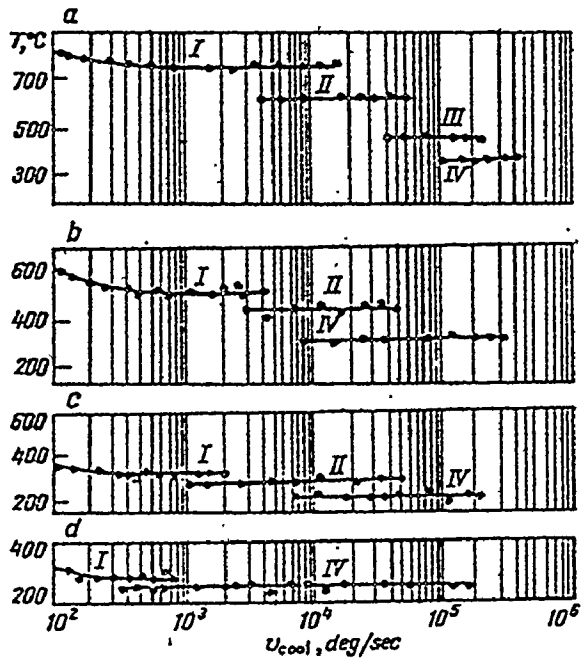
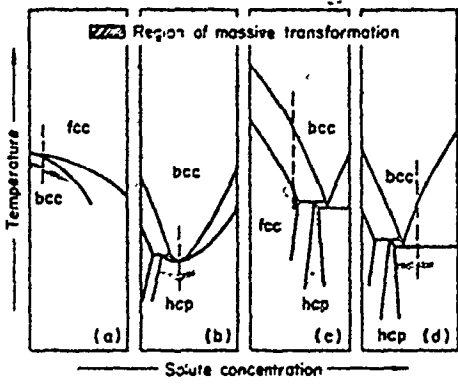
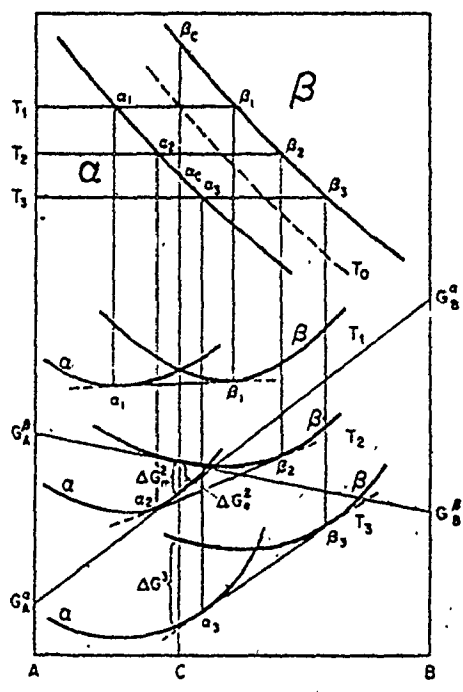


Figure (26) Influence of cooling rate on the temperatures at which the $\gamma \rightarrow \alpha$ transformation begins in Fe-Mn alloys: a-1.2; b-4.1; c-7.5; d-9.8%Mn: I-IV stages of transformation (after Shtyenberg et. al.(47)).



(I)



(II)

Figure (27) (I) Schematic phase diagrams for various types of alloys that may undergo massive transformations, (critical compositions are indicated by dashed vertical lines), (II) Schematic free energy diagrams for β and α phases (after Massalski⁽⁵⁴⁾).

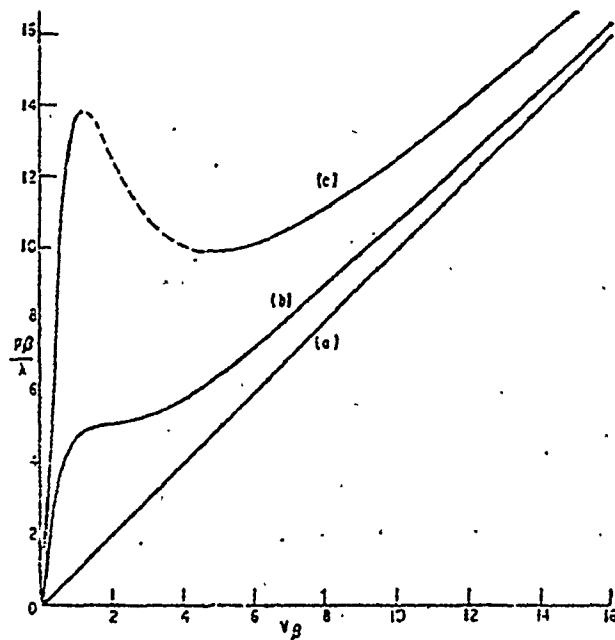


Figure (28) The driving force versus velocity curve for various compositions. (a) pure material, (b) and (c) correspond to the increasing concentration of impurity. The unstable part of the curve (c) is broken. The two stable branches (c.f. curve (c)) conform to the low and high velocity approximations (after Cahn(64)).

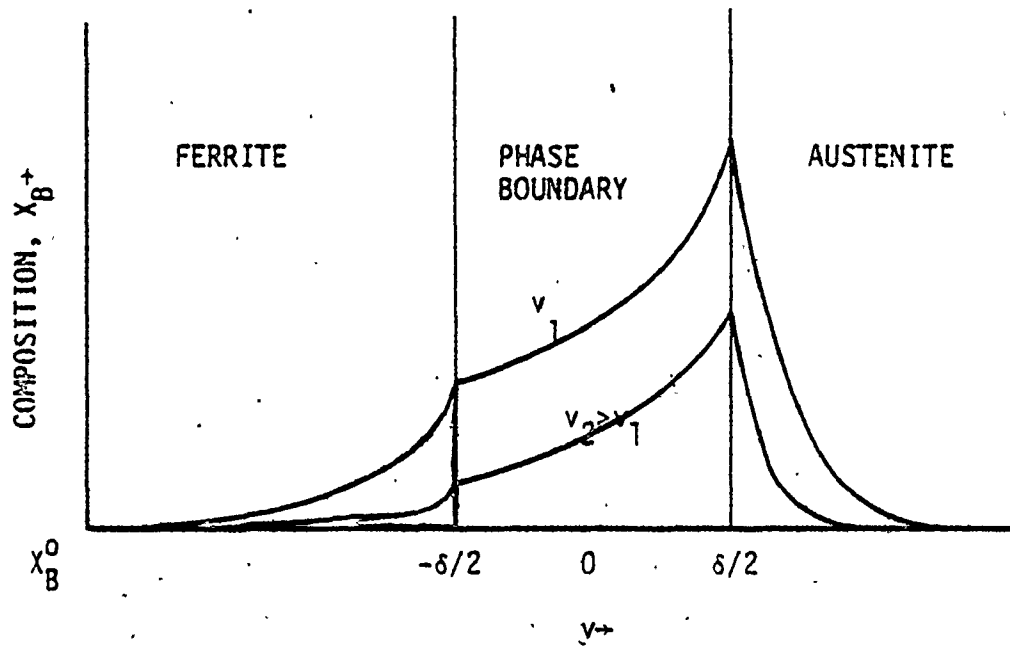


Figure (29) Schematic steady state composition profiles in ferrite, phase boundary, and austenite for boundary velocities, v_1 and v_2 .

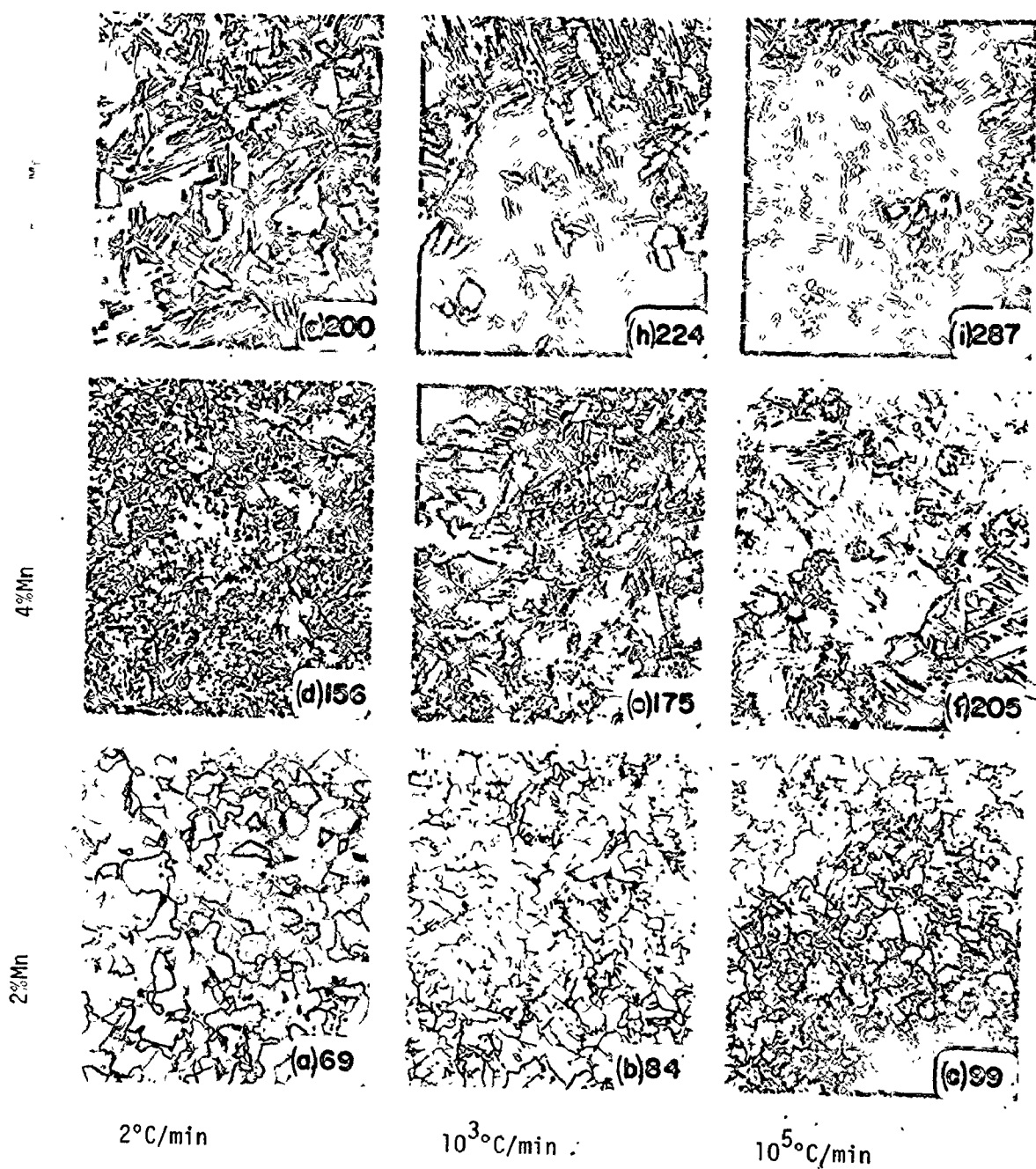


Figure (30) a-i Various ferrite morphologies in Fe-Mn alloys as a function of composition and cooling rate, $\times 120$, number on each micrograph gives microhardness, DPH, for 500 gm load.

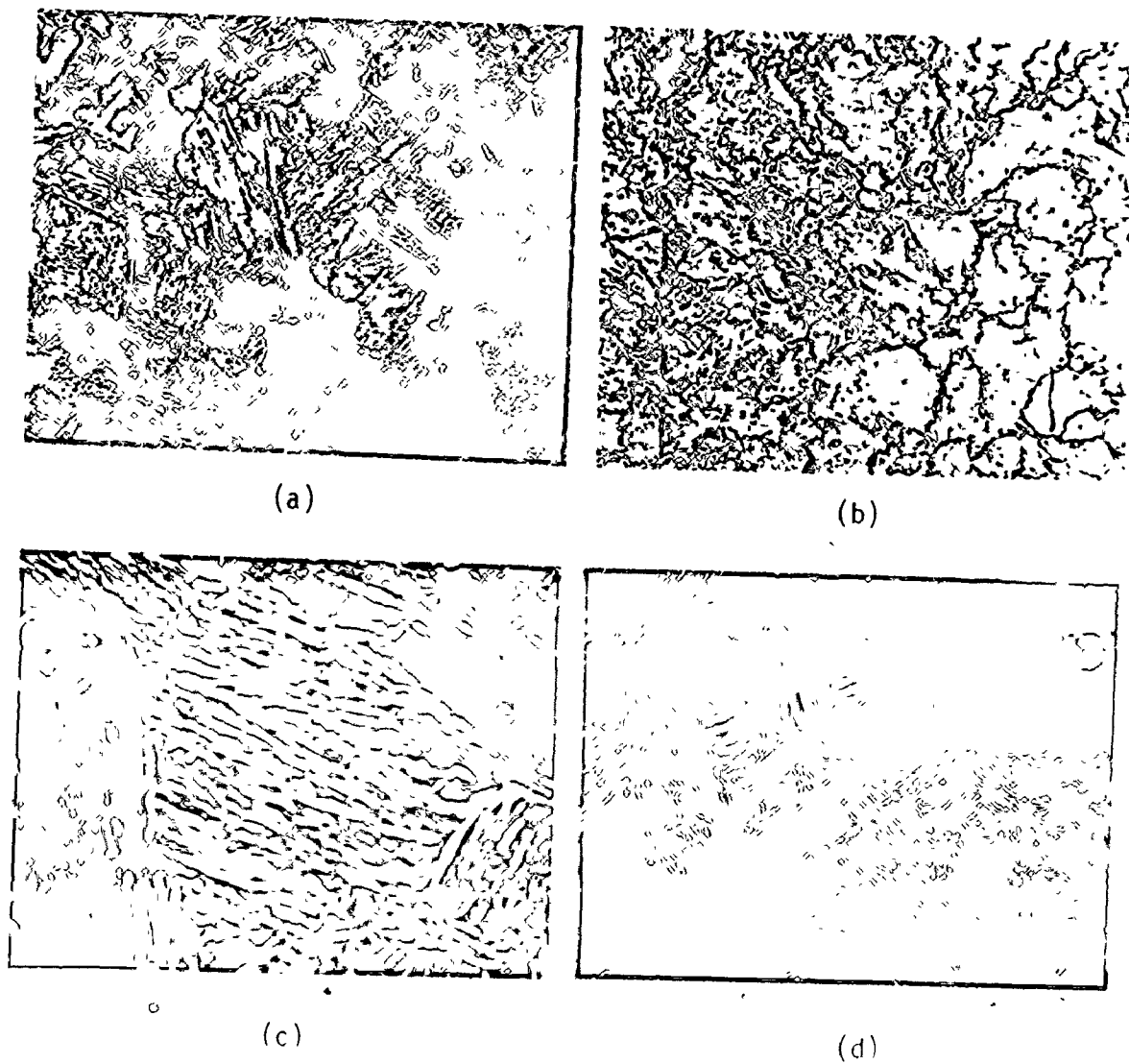
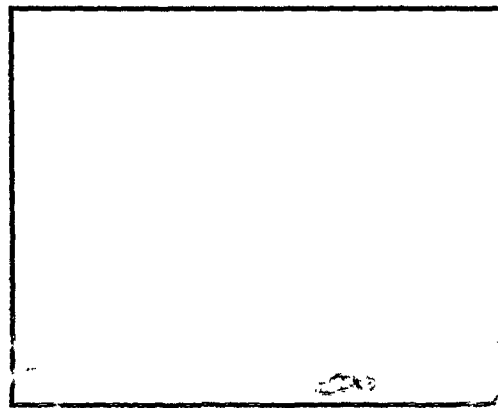
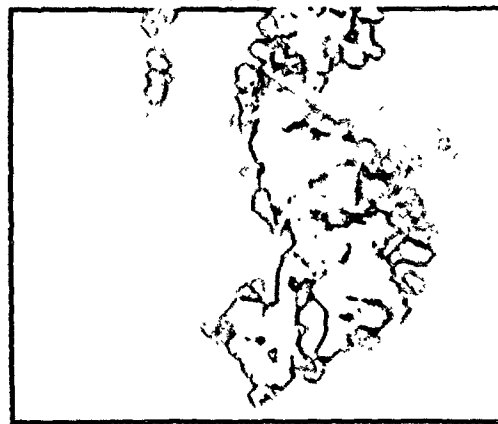


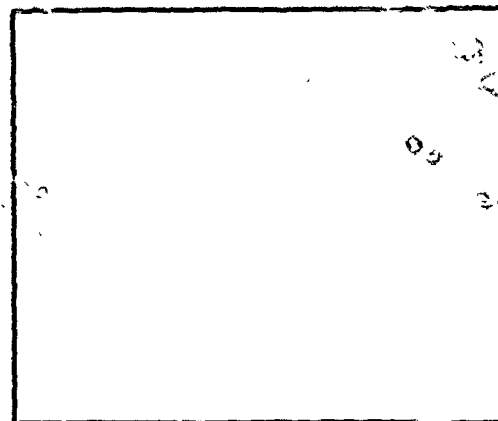
Figure (31) a. Optical micrograph of air cooled Fe-4% Mn alloy, x250, and b. that of prepolished sample of Fe-6.2%Mn alloy austenitized at 900°C for 10 min. and then unbroken capsule thrown in water, x125. Note the surface rumpling following the transformation, c. Scanning electron micrograph of water quenched Fe-4%Mn alloy, x1000, and d. that of Fe-1.5%Mn-0.25%Mn alloy, x500.



(a)



(b)



(c)

Figure (32) Transmission electron micrographs of (a) furnace cooled Fe-2%Mn alloy, x14000, (b) water quenched Fe-4%Mn alloy, x12000 and (c) water quenched Fe-1.5%Mn-0.25%Mo, x64000.

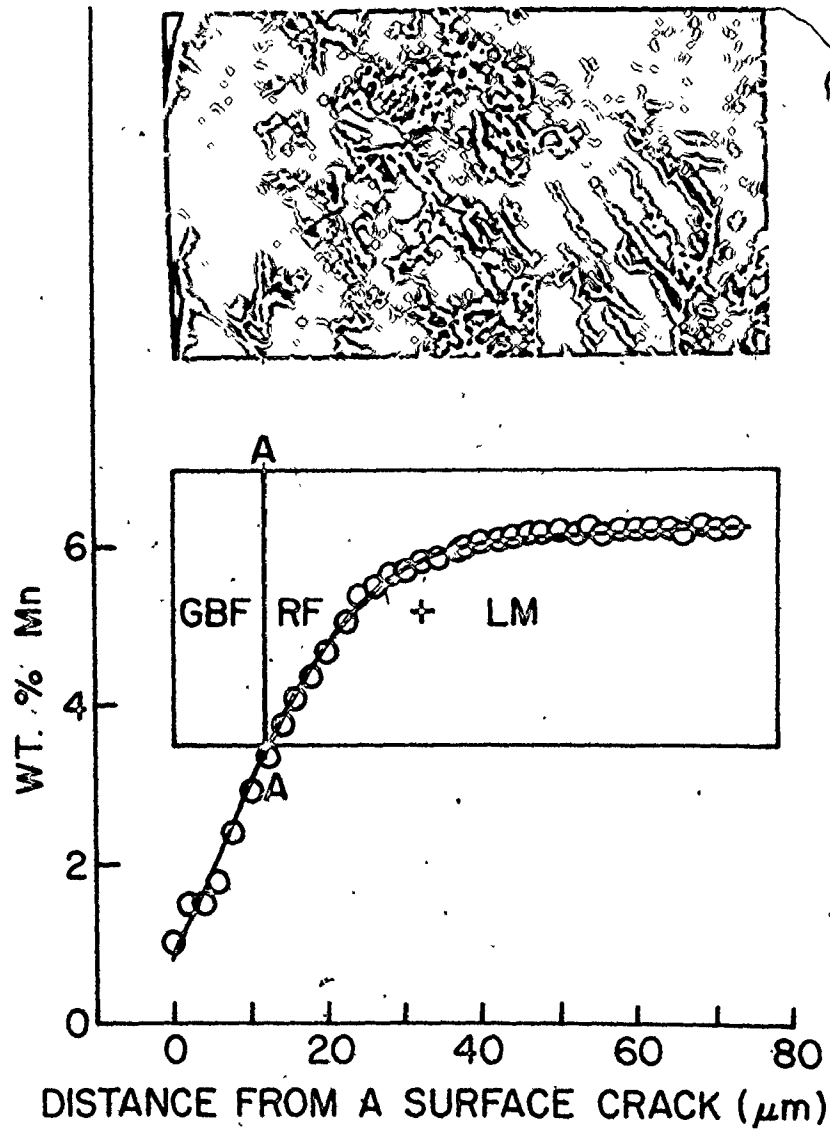


Figure (33a) Variation of ferrite morphology with composition in Fe-6.2%Mn alloy austenitized at 1100°C in vacuum sealed quartz capsule for 24 hours followed by furnace cooling. GBF: Grain boundary ferrite, RF: Ragged Ferrite, LM; Lath morphology.

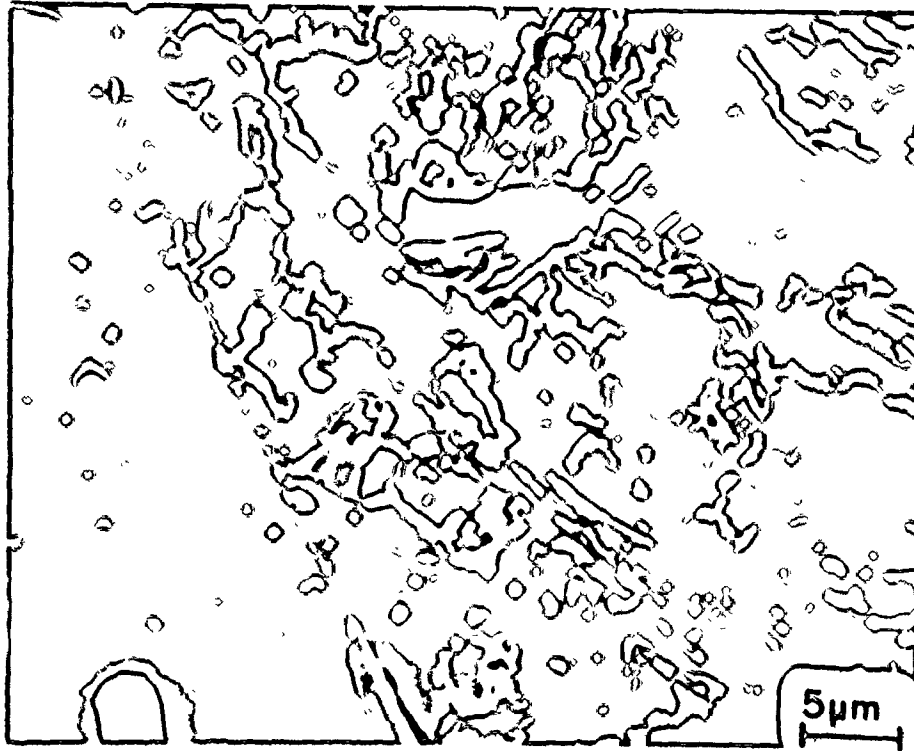
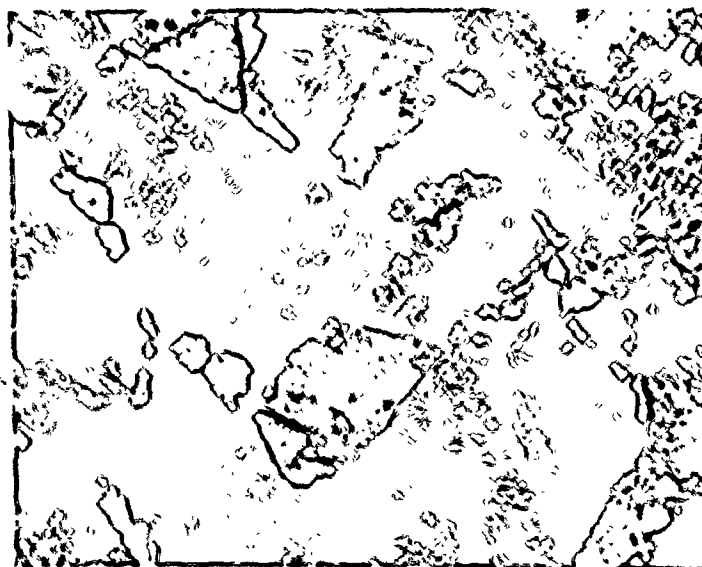


Figure (33b) Scanning electron micrograph of the same region as shown in Figure (33a) at higher magnification.

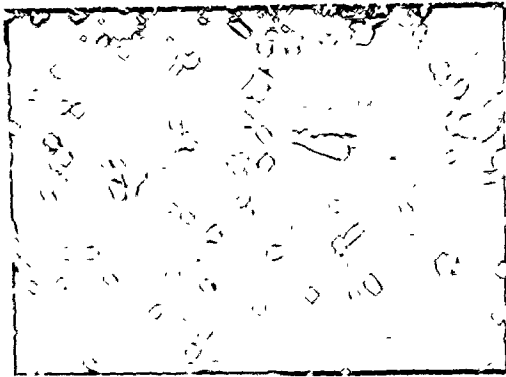


(a)

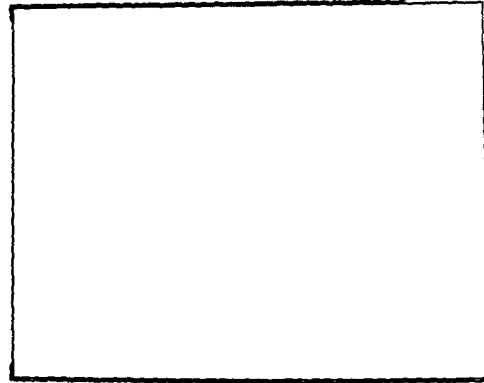


(b)

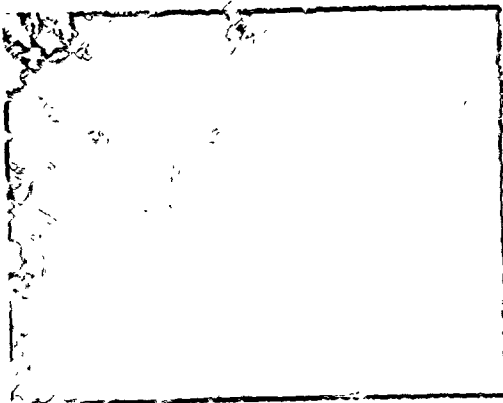
Figure (34): Optical micrographs at higher magnification (x240) for the estimation of fraction of grain boundary ferrite formed in (a) Fe-2.8%Mn alloy at 675°C for 10 min. and (b) Fe-3.1%Mn at 620°C for 27 min.



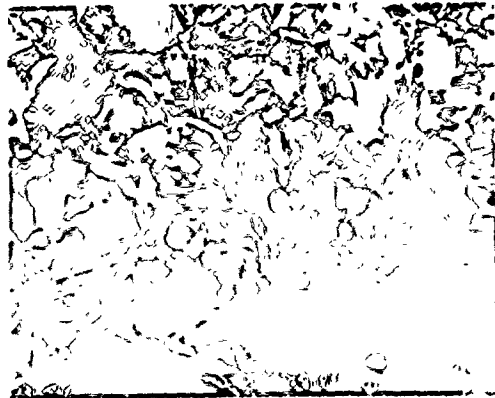
a. 600°C/60 min.



b. 620°C/27 min.

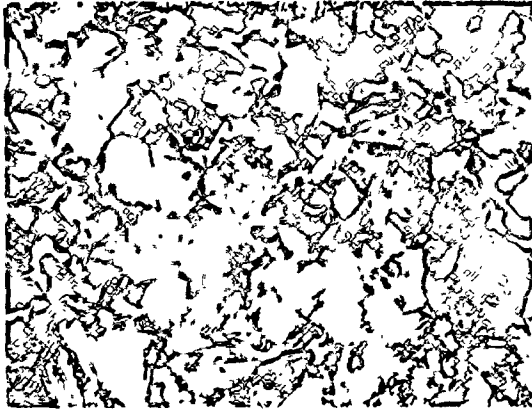


c. 630°C/18 min.

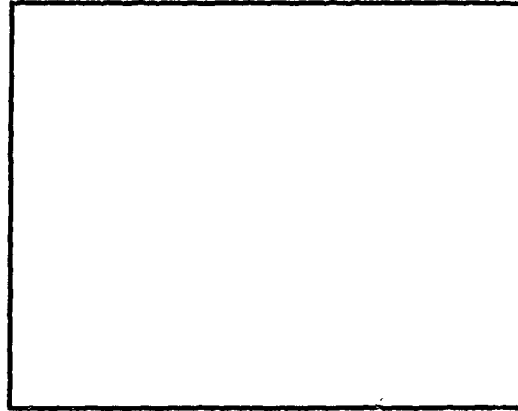


d. 630°C/21 min.

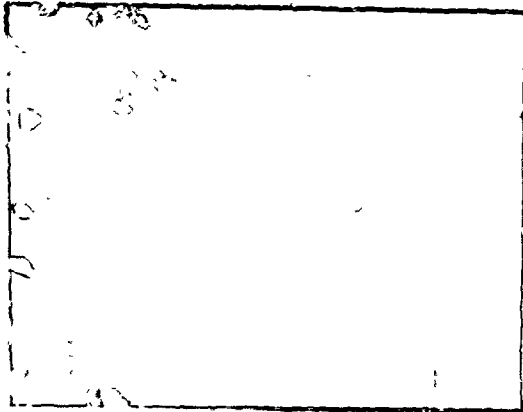
Figure (35) Microstructures of Fe-3.1%Mn samples austenitized at 1040°C for 30 min. and followed by different heat treatments, x60.



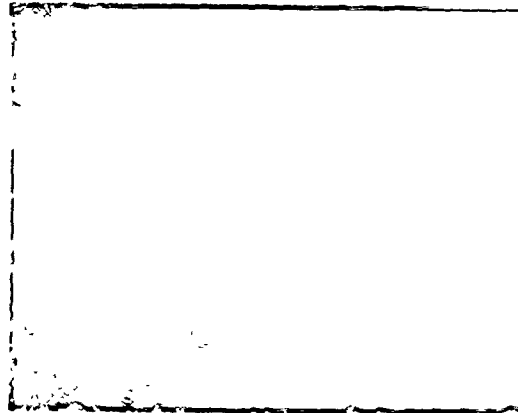
e. 640°C/15 min.



f. 640°C/30 min.



g. 650°C/20 min.



h. 660°C/43 min.

Figure (35) cont'd. Microstructures of Fe-3.1%Mn samples austenitized at 1040°C for 30 min. and followed by different heat treatments, x60.

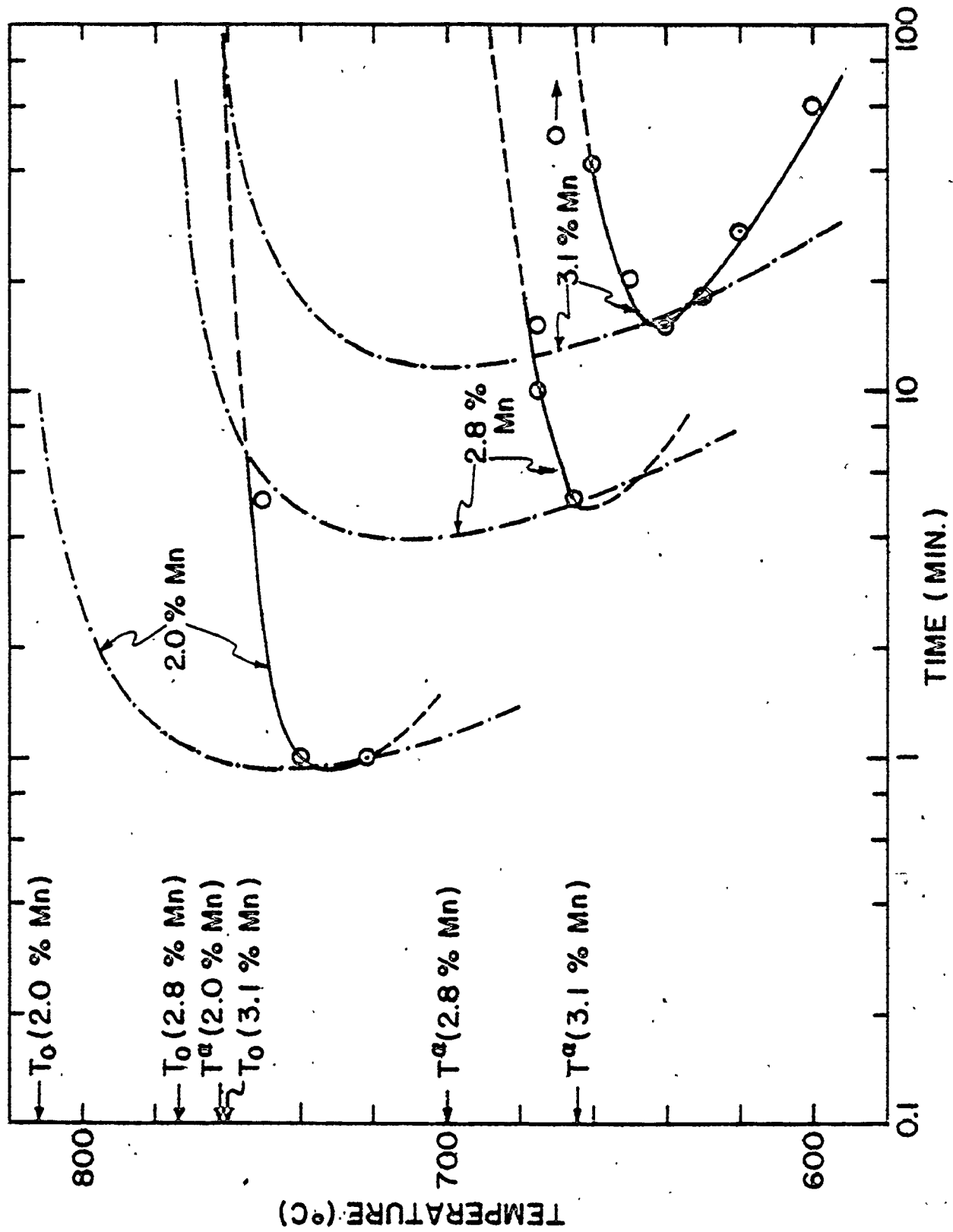


Figure (36) TTT start (5%) curves for grain boundary ferrite formation in Fe-Mn alloys. (—) theoretical TTT start curves for pure massive control.

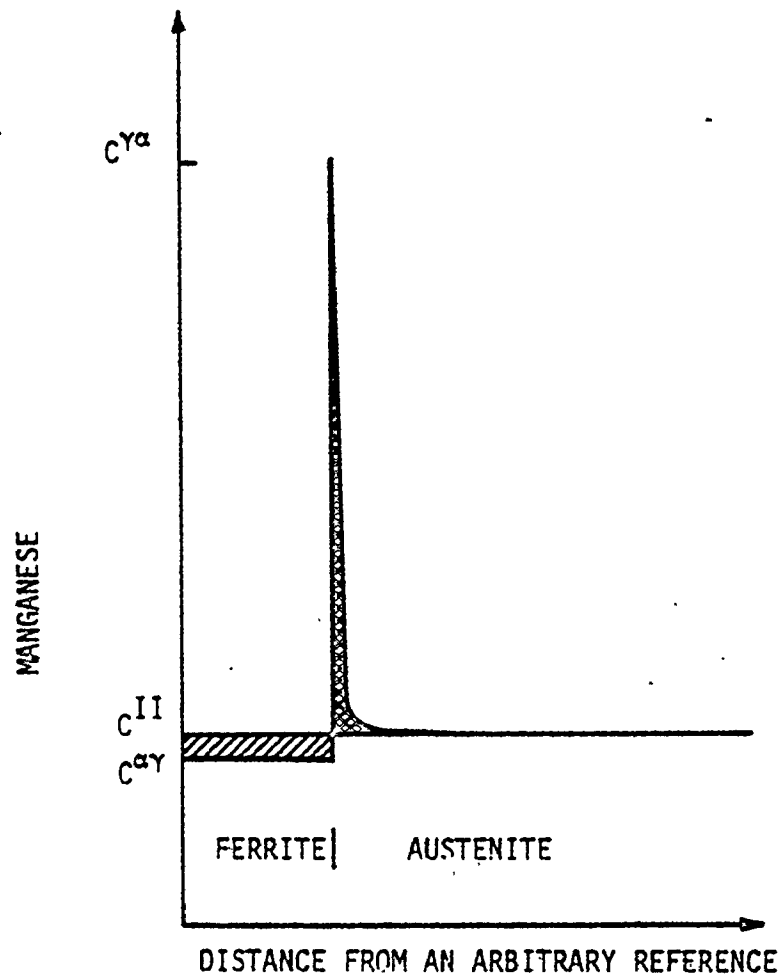
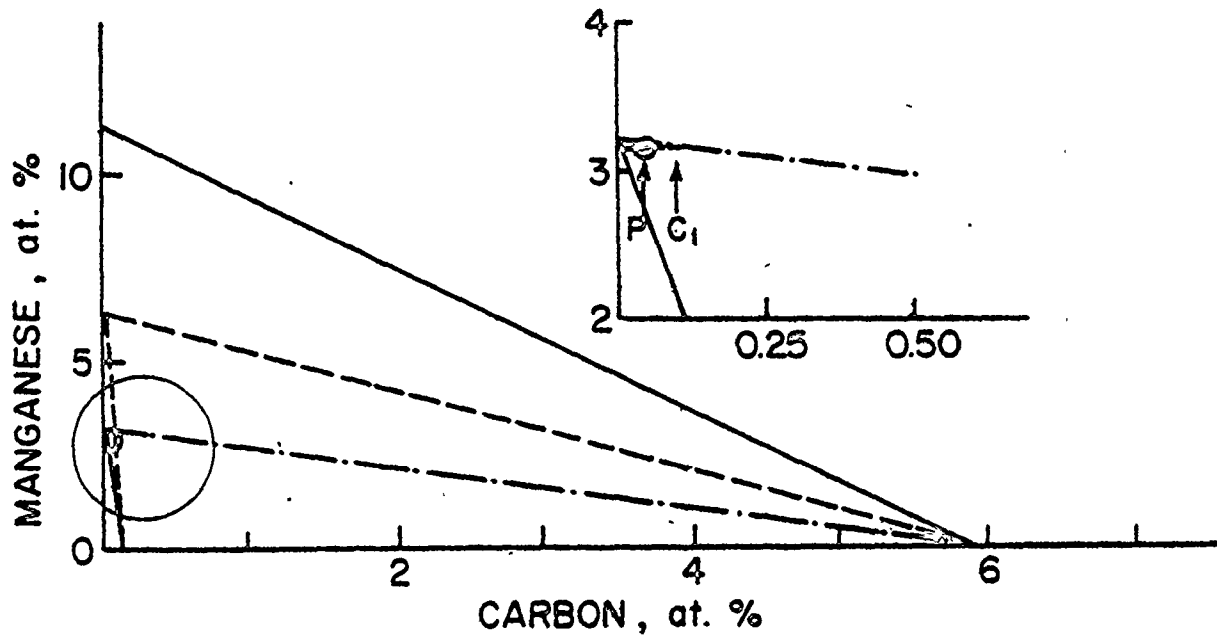
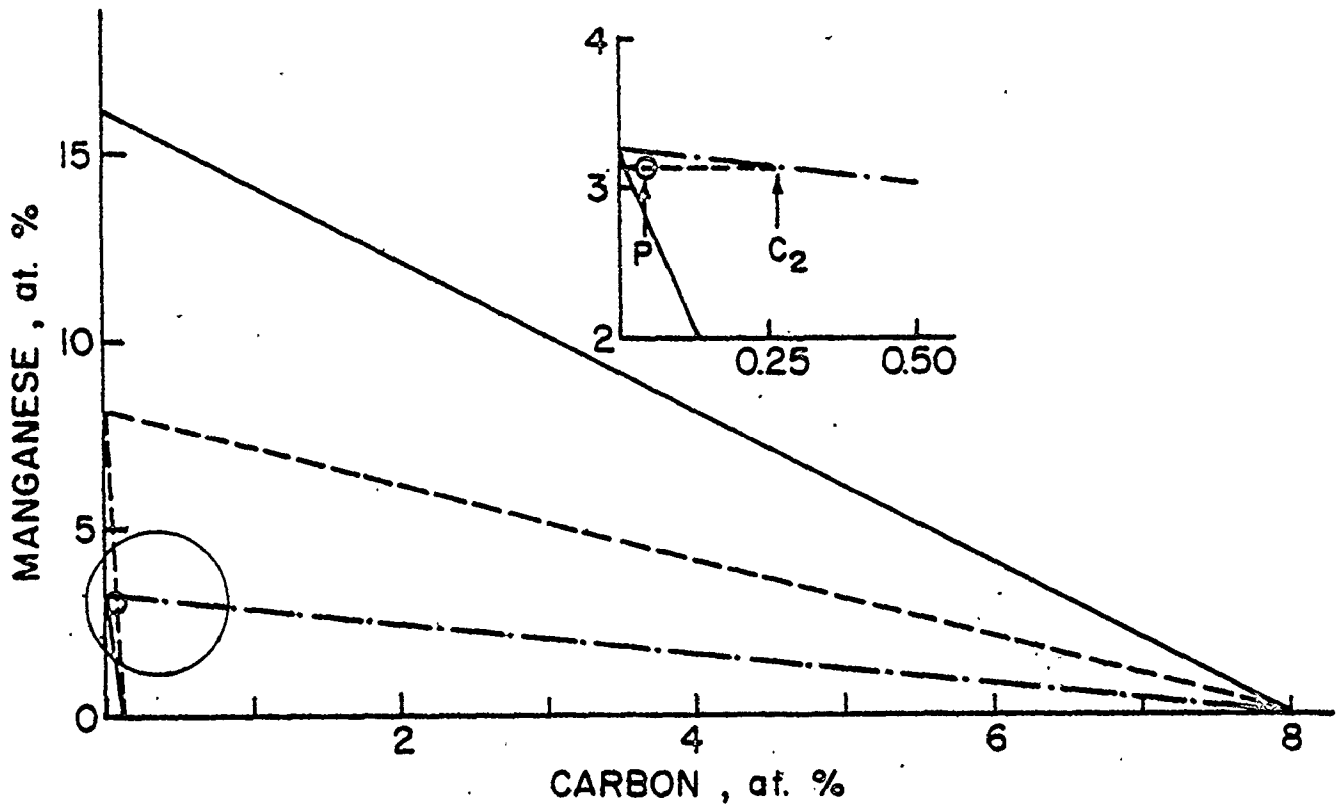


Figure (37) Schematic manganese spike in austenite, ahead of the advancing interface.



(a)



(b)

Figure (38) a. An approximate Fe-Mn-C isotherm: (—) true equilibrium, (---) envelope of zero partition, (- - -) para equilibrium, (·) composition of alloy, at 660°C and b. at 600°C. The areas in circle are shown on expanded scales.

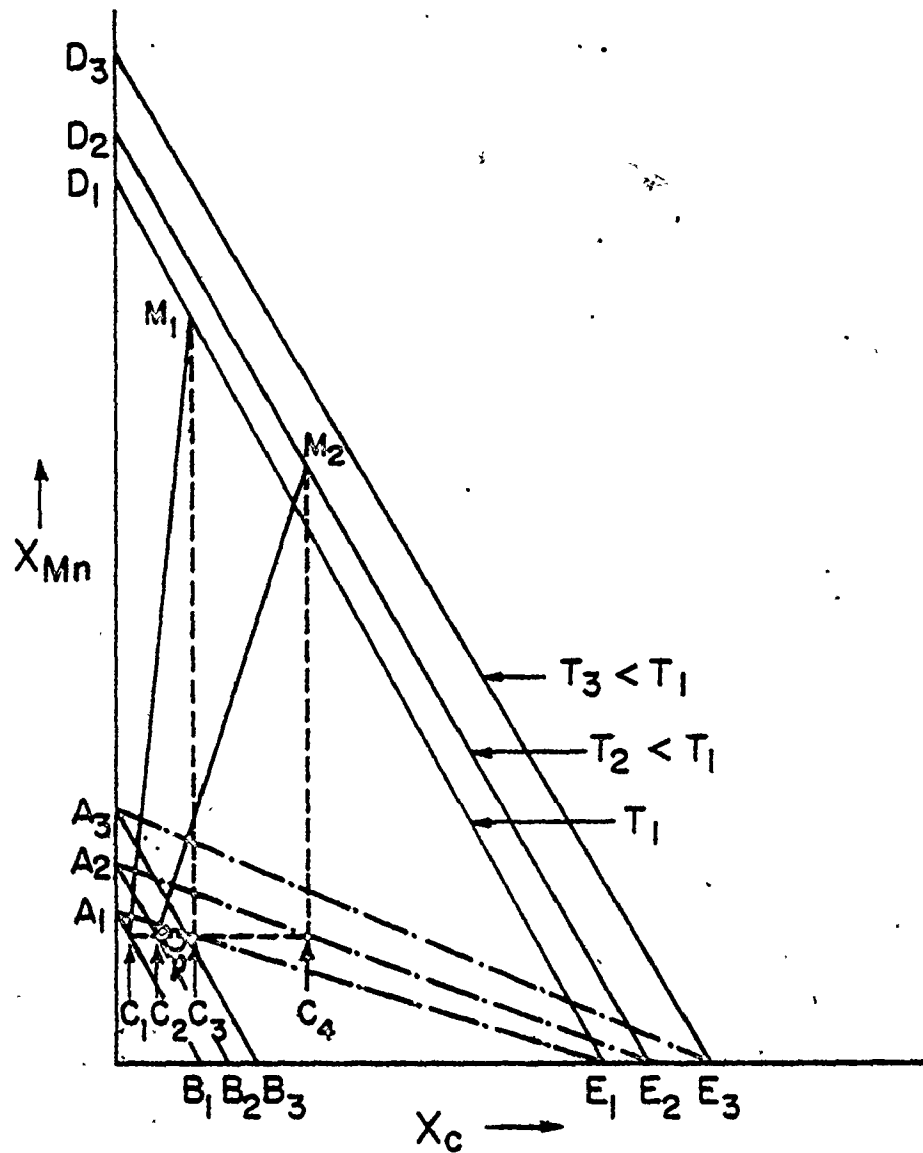


Figure (39) Schematic representation of the variation of driving force for carbon diffusion ahead of austenite (controlling the rate of transformation) with variation in temperature estimated in terms of location of the bulk composition of alloy relative to the ferrite/austenite boundaries; A_1B_1/D_1E_1 , A_2B_2/D_2E_2 , and A_3B_3/D_3E_3 are the ferrite/austenite solvus, respectively, for temperature $T_1 > T_2 > T_3$; (— — —) envelop of zero partition.